

INFORMATION TO USERS

The most advanced technology has been used to photograph and reproduce this manuscript from the microfilm master. UMI films the text directly from the original or copy submitted. Thus, some thesis and dissertation copies are in typewriter face, while others may be from any type of computer printer.

The quality of this reproduction is dependent upon the quality of the copy submitted. Broken or indistinct print, colored or poor quality illustrations and photographs, print bleedthrough, substandard margins, and improper alignment can adversely affect reproduction.

In the unlikely event that the author did not send UMI a complete manuscript and there are missing pages, these will be noted. Also, if unauthorized copyright material had to be removed, a note will indicate the deletion.

Oversize materials (e.g., maps, drawings, charts) are reproduced by sectioning the original, beginning at the upper left-hand corner and continuing from left to right in equal sections with small overlaps. Each original is also photographed in one exposure and is included in reduced form at the back of the book.

Photographs included in the original manuscript have been reproduced xerographically in this copy. Higher quality 6" x 9" black and white photographic prints are available for any photographs or illustrations appearing in this copy for an additional charge. Contact UMI directly to order.

U·M·I

University Microfilms International
A Bell & Howell Information Company
300 North Zeeb Road, Ann Arbor, MI 48106-1346 USA
313/761-4700 800/521-0600

Order Number 9111974

Radiative transfer model for a spherical atmosphere

Thome, Kurtis John, Ph.D.

The University of Arizona, 1990

U·M·I
300 N. Zeeb Rd.
Ann Arbor, MI 48106



RADIATIVE TRANSFER MODEL FOR A SPHERICAL ATMOSPHERE

by

Kurtis John Thome

A Dissertation Submitted to the Faculty of the
DEPARTMENT OF ATMOSPHERIC SCIENCES
In Partial Fulfillment of the Requirements
For the Degree of
DOCTOR OF PHILOSOPHY
In the Graduate College
THE UNIVERSITY OF ARIZONA

1 9 9 0

STATEMENT BY AUTHOR

This dissertation has been submitted in partial fulfillment of requirements for an advance degree at the University of Arizona and is deposited in the University Library to be made available to borrowers under rules of the Library.

Brief quotations from this dissertation are allowable without special permission, provided that accurate acknowledgement of source is made. Requests for permission for extended quotation from or reproduction of this manuscript in whole or in part may be granted by the head of the major department or the Dean of the Graduate College when in his or her judgement the proposed use of the material is in the interests of scholarship. In all other instances, however, permission must be obtained from the author.

SIGNED:

A handwritten signature in cursive script, reading "Kurtis John Brown", written over a horizontal line.

ACKNOWLEDGEMENTS

The author would like to thank the members of his committee for taking the time to read and critique this dissertation. Special thanks go out to my advisor Dr. Benjamin M. Herman for his help in developing this model. His expertise in the field and hallway discussions greatly aided my understanding of the problem. I also would like to acknowledge those who made early attempts at spherical modelling at the University of Arizona, especially Dr. Aivishai Ben-David whose help in writing and debugging the actual code was immense help.

I would like to thank my family, both near and far, for their undying support and encouragement during this endeavour. A special note of thanks goes to my wife, Leatha, whose help in preparing this manuscript was immeasurable and whose smiling face was a source of inspiration.

TABLE OF CONTENTS

	Page
LIST OF ILLUSTRATIONS	7
ABSTRACT	10
I.INTRODUCTION	11
II.THEORY	17
1. The General Radiative Transfer Equation	17
2. The Radiative Transfer Equation in a Flat Atmosphere	20
3. The Radiative Transfer Equation in a Spherical Atmosphere	21
III.METHOD	24
1. Differences between the Flat and Spherical Cases	24
2. Coordinate System and Conical Boundary	27
3. Application of the Radiative Transfer Equation	30
4. Single Scatter Calculation	31
5. Zenith Multiple Scatter	35
a. The Source Term Integral	36
b. The Incident Multiple Scatter	39
6. Cone Multiple Scatter	40
a. The Source Term Integral	42
b. The Incident Multiple Scatter	43
7. The Gauss-Sidel Iteration	44

TABLE OF CONTENTS - - Continued

	Page
IV. RESULTS AND CHECKS	48
1. Choice of Parameters	48
2. Flat Atmosphere Comparison	52
3. Energy Conservation	55
4. Cone to Zenith Comparison	58
5. Comparison with Other Methods	60
V. APPLICATION TO LIMB SCAN	78
VI. CONCLUSIONS AND FURTHER WORK	95
APPENDIX A CALCULATION OF ATMOSPHERIC PARAMETERS	98
REFERENCES	102

LIST OF ILLUSTRATIONS

Figure		Page
1.1	Diagram to illustrate the path differences between (a) the flat atmosphere and (b) the spherical atmosphere.	12
3.1	Illustration demonstrating the change in solar zenith angle at the top of the atmosphere.	26
3.2	Coordinates used in the current method.	29
3.3	Diagram illustrating the incident intensities and layers used to compute the multiple scatter contribution and also the numerical method approximation of the source integral. . .	32
3.4	Illustration showing the optical depths along the solar path and the line of sight. Also shows the layers used in calculating the single scatter.	34
3.5	Shows the boundary for the three line of sight cases on the zenith as well as the points used for interpolation of the incident multiple scatter and the intensities used in the calculation of the source term integral.	37
3.6	Shows the boundary for the three line sight cases on the cone.	41
4.1	Transmitted intensities at the surface for the case of a high sun and small optical depth. Comparison with flat atmosphere results for $\phi=0$ and 180 degrees.	53
4.2	Transmitted intensities at the surface for the case of a high sun and small optical depth. Comparison with flat atmosphere results for $\phi=60$ and 120 degrees.	54
4.3	Reflected intensities at the top of the atmosphere for the case of a high sun and small optical depth. Comparison with flat atmosphere results for $\phi=0$ and 180 degrees.	56
4.4	Reflected intensities at the top of the atmosphere for the case of a high sun and small optical depth. Comparison with flat atmosphere results for $\phi=60$ and 120 degrees.	57
4.5	Transmitted intensities at the surface for $\eta = \phi = 0$ and 180 degrees. Shows the cone to zenith comparison.	61

LIST OF ILLUSTRATIONS - - Continued

Figure		Page
4.6	Transmitted intensities at the surface for $\eta = \phi = 60$ and 150 degrees. Shows the cone to zenith comparison.	62
4.7	Reflected intensities at the top of the atmosphere for $\eta = \phi = 0$ and 180 degrees. Shows the cone to zenith comparison. . .	63
4.8	Reflected intensities at the top of the atmosphere for $\eta = \phi = 60$ and 150 degrees. Shows the cone to zenith comparison. .	64
4.9	Transmitted intensities at the surface for $\phi=0$ and 180 degrees. Results are from Asous(1982) and the current method. . .	66
4.10	Reflected intensities at the top of the atmosphere for $\phi=0$ and 180 degrees. Results are from Asous(1982) and the current method.	67
4.11	Transmitted intensities at the surface for $\phi=60$ and 120 degrees. Results are from Asous(1982) and the current method. . .	68
4.12	Reflected intensities at the top of the atmosphere for $\phi=60$ and 120 degrees. Results are from Asous(1982) and the current method.	69
4.13	Transmitted intensities at the surface for $\phi=0$ and 180 degrees and albedo of 0.0. Results are from Marchuk <i>et al.</i> (1980) and the current method.	70
4.14	Transmitted intensities at the surface for $\phi=0$ and 180 degrees and albedo of 0.25. Results are from Marchuk <i>et al.</i> (1980) and the current method.	71
4.15	Reflected intensities at the top of the atmosphere for $\phi=0$ and 180 degrees and albedo of 0.0. Results are from Marchuk <i>et al.</i> (1980) and the current method.	72
4.16	Reflected intensities at the top of the atmosphere for $\phi=0$ and 180 degrees and albedo of 0.25. Results are from Marchuk <i>et al.</i> (1980) and the current method.	73
4.17	Reflected intensities at the top of the atmosphere for $\phi=0$ and 180 degrees for a homogeneous Rayleigh atmosphere of optical depth 0.25. Results are from Adams and Kattawar(1978) and the current method.	75

LIST OF ILLUSTRATIONS - - Continued

Figure		Page
4.18	Reflected intensities at the top of the atmosphere for $\phi=0$ and 180 degrees for a homogeneous Rayleigh atmosphere of optical depth 1.00. Results are from Adams and Kattawar(1978) and the current method.	76
5.1	Height distribution of air molecules for Model I, and distribution of ozone molecules($\times 10^6$) for Model II in terms of mass density.	79
5.2	Height distribution of aerosols for Models III, IV, and V.	80
5.3	Satellite geometry and definition of terms used in the atmospheric limb scan.	82
5.4	Flat atmosphere comparison for Model III with 0.04 ozone optical depths for $\phi =90$ and 180 degrees.	84
5.5	Flat atmosphere comparison for Model IV with 0.04 ozone optical depths for $\phi =90$ and 180 degrees.	85
5.6	Flat atmosphere comparison for Model V with 0.04 ozone optical depths for $\phi =90$ and 180 degrees.	86
5.7	Comparison between Models III, IV, and V with 0.0 ozone optical depths for $\phi =90$ degrees to show effect of volcanic layers.	88
5.8	Comparison between Models III, IV, and V with 0.04 ozone optical depths for $\phi =90$ degrees to show effect of volcanic layers.	89
5.9	Satellite limb scan simulation for Model II with ozone optical depths of 0.00, 0.02, 0.04, and 0.08 and $\phi =90$ degrees.	91
5.10	Satellite limb scan simulation for Model II with ozone optical depths of 0.00, 0.02, 0.04, and 0.08 and $\phi =90$ degrees and solar zenith angle of 85 degrees.	92
5.11	Satellite limb scan simulation for Model III with ozone optical depths of 0.00, 0.02, 0.04, and $\phi =90$ degrees.	93

ABSTRACT

A new model for computing radiative transfer in a spherically symmetric atmosphere has been developed which uses a Gauss-Sidel iteration similar to Herman(1963). To account for inhomogeneities in the horizontal intensity field, the current work introduces a conical boundary on which solutions are found. This boundary is used in an interpolation scheme to obtain the intensity at the center of the cone. The model includes absorption and aerosols but neglects polarization and refraction.

Checks of the model were performed. Results for a high sun and small optical depth compared to flat atmosphere results were consistent with geometric arguments. The results where the radius of the planet was increased by a factor of 100 agree with flat atmosphere results to better than 1%. Flux is conserved to better than 3%, and boundary solutions are accurate to better than 3% for nontangent paths, and 12% for tangent paths. A 10% biased boundary solution caused less than a 1% change in the final solution. The model also agreed favorably with models developed by Asous (1982), Marchuk *et al.* (1980) and Adams and Kattawar (1978). From the results of tests the model is concluded to be accurate to 3%, and in most earth-atmosphere situations accurate to 1%. This accuracy is on the order of, or better than, previous techniques and more computationally efficient than Monte Carlo simulations. The current model is more versatile and accurate than techniques that strive for computational efficiency.

The model was used to examine the atmospheric limb problem and results from this work indicate that ozone and stratospheric dust layers may be detected from limb measurements.

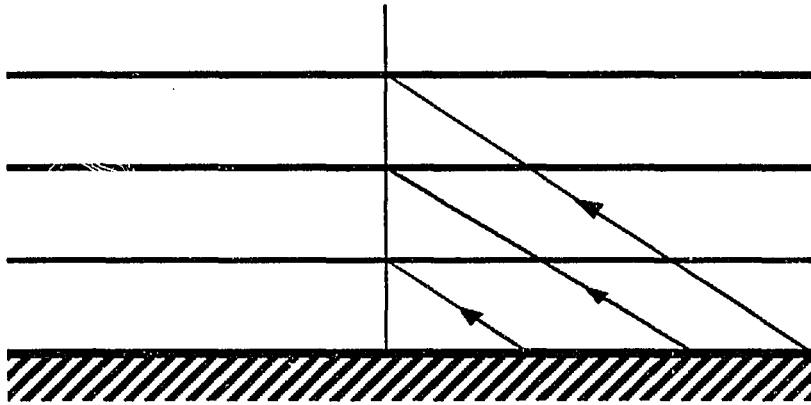
CHAPTER I

INTRODUCTION

Radiative transfer in the earth's atmosphere has long been of interest for a wide variety of problems. Since solar radiation is the primary source of energy for the earth's atmosphere, its behavior in the atmosphere is especially of interest. In the past, radiative transfer models have emphasized the plane-parallel model. This model assumes that the atmosphere consists of plane-parallel homogeneous layers. This assumption simplifies the radiative transfer equation and reduces the computer time required to solve a given problem. Van de Hulst(1980) reviews the different techniques used to solve the flat atmosphere problem. One of these is the Gauss-Sidel iteration method(Herman(1963) and Herman and Browning(1965)). This method is both accurate and efficient. In the current work, a spherical radiative transfer model is developed that applies Gauss-Sidel iteration to a spherically symmetric atmosphere.

Typically the plane parallel assumption is quite accurate, but there are situations where assuming the atmosphere to be plane-parallel results in loss of accuracy. These cases occur when the zenith angle, solar and/or viewing, approaches ninety degrees. Limb scans of the earth's atmosphere from satellites is one case which falls into this category. The flat atmosphere approach breaks down completely when the solar zenith angle exceeds ninety degrees. Path length differences cause most of the differences between the flat and the spherical approaches. Fig. 1 shows one example of how the two situations differ with exaggerated path length differences. It is clear that the spherical geometry

(a)



(b)

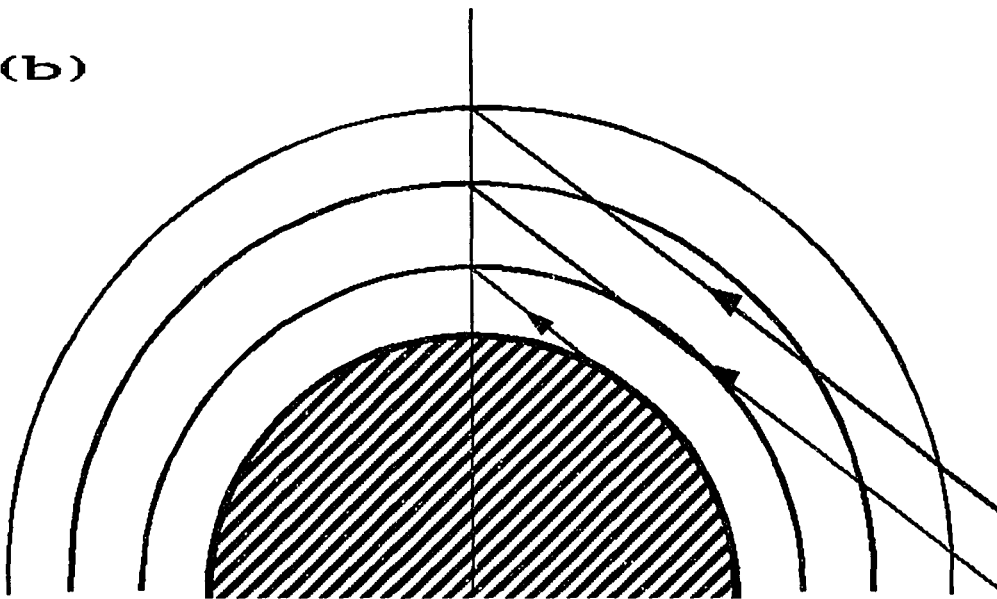


Fig. 1.1 Diagram to illustrate the path differences between the flat atmosphere, part (a) and the spherical atmosphere in part (b).

is more appropriate when modelling twilight sky, horizon, and satellite limb measurements.

Early radiative transfer calculations with spherical geometry were carried out for non-atmospheric problems. Collins and Wells(1965) used a Monte Carlo scheme to describe the diffusion of neutrons in nuclear reactors. Bellman *et al.*(1968) developed a spherical model to determine the brightness of planetary nebula. Kattawar *et al.*(1971) used a Monte Carlo method to compute emergent intensities from Venus.

To date, most spherical studies of the earth's atmosphere have concentrated on twilight phenomenon. Hulbert(1953) used single scattering to explain the colors of the twilight sky. He proposed that the deep blue color of the zenith sky at twilight results from ozone absorption in the Chappuis band at around $0.6 \mu\text{m}$. Rozenberg(1966) gave a qualitative discussion of multiple scattering at twilight. Dave and Mateer(1968) computed single scattering for several atmospheric models. They concluded that an atmosphere with only Rayleigh scattering should appear yellow at twilight. Ozone absorption creates the blue colors, while aerosols tend to enhance the blue and give rise to purple. Adams *et al.*(1974) attributed the reds and oranges to the effects of aerosols. Blattner *et al.*(1974) and Blattner(1977) used a spherical model and color ratios to show that surface measurements can detect stratospheric dust layers. The location and the width of the peak of the color ratio versus solar angle provide the height and thickness of the layers.

The increase in satellite limb measurements in recent years has created a new need for radiative transfer models in spherical atmospheres. Rozenberg(1965) attempted to quantify multiple scatter effects in limb measurements. Whitney

et al.(1974) and Marchuk(1980) both applied spherical models to satellite measurements, as did Newell and Gray(1972).

Lenoble and Sekera(1961) first gave the radiative transfer equation in spherical coordinates. Since no general analytic solution has been found, a number of approximate solutions have been developed(Lenoble(1985)) These methods include Monte Carlo methods, invariant imbedding, moments of intensity and stream methods, and approximations to an exact solution. Bailey(1964) derived the equations for an invariant imbedding approach. Bellman(1966) solved these for diffuse reflection from an absorbing sphere. Leong and Sen(1972 and 1975) compared results from an invariant imbedding scheme to a more probabilistic approach.

Marchuk(1980) reviews the Monte Carlo techniques that have been applied to the spherical geometry problem. Early attempts were made by Marchuk and Mikhailov(1967a), Smokty(1969), and Collins and Wells(1970). Collins *et al.*(1972) used their FLASH program to study the importance of multiple scattering and polarization. Blattner(1974) added refraction to this model as well as ozone absorption.

Using the moments of intensity simplifies the problem by removing the dependency on the polar angle. Hummer and Rybicki(1971) and Unno and Kondo(1976) applied the Eddington factor to obtain solutions. Sobolev(1975) and Wilson(1980a and b) solved higher order scattering by moments methods. Simonneau(1976) assumed the source term to be a function of the zero order moment of the intensity. An approach that also uses the moments of intensity is the stream or DART method. Using this technique Newell and Gray(1972) and Whitney(1972) solved for the radiation as seen by a satellite. Gray(1973)

solved the single scatter exactly and applied the stream method to the higher order scattering. Whitney(1974) attempted to improve efficiency by treating the scattering in thin layers as matrix operators, then combining the operators of several layers.

Several techniques make approximations to the exact problem to allow solutions to be found. Chapman(1966) used this approach to solve a gray spherically symmetric atmosphere. Minin and Sobolev(1963) assumed isotropic scattering and solved the flat atmosphere case with a varying solar angle to simulate spherical effects on the solar beam. Smokty used this technique on a plane cylindrical atmosphere. Sobolev(1975) applied the varying solar angle technique to non-isotropic scattering.

Another approach is to solve the single, or primary, scattering exactly in spherical geometry and then approximate the higher order scattering. Divari and Plotnikova(1966) solved the multiple scattering in terms of the single scattering. Sobolev(1975) and Wilson and Sen(1980a and b) solved the multiple scattering by retaining only the first two terms of the Legendre polynomial expansion of the phase function. Asous(1982) assumed each local region to be flat and used a Gauss-Sidel iteration, with all path lengths and angles computed from spherical geometry.

The current work utilizes a Gauss-Sidel iteration with all angles and path lengths computed using sphericity. The solution to the general radiative transfer equation is obtained with the needed incident intensity field supplied by a conical boundary. A more detailed description of the technique and the grid is given in Chapter 3. The general radiative transfer equation, in both integral and differential forms, is presented in Chapter 2. This chapter also gives the

differential forms of the radiative transfer equation in plane-parallel and spherical geometries without polarization. Polarization can be included by incorporating the required matrix formulation into the transfer equation and thus into the computer model as well, but has been neglected here because of computing time and storage constraints.

The application of the general radiative transfer equation to the current problem is described in Chapter 3 where the coordinate system and grid used to solve the problem are discussed. The results from the model are presented in Chapter 4 together with several checks of the model. The boundary solution for a given solar zenith angle is compared to the zenith solution for a properly adjusted solar zenith angle. The model is also run for a high sun case and compared to flat atmosphere results. Flat atmosphere results are also compared to model results with the radius of the planet is increased by two orders of magnitude. Comparisons to other models and a check of conservation of energy in a conservative atmosphere are given as well. Also given is a discussion of the optimum discretization of the variables.

In Chapter 5, the model is used to simulate satellite data. Five model atmospheres are used. The first is a pure Rayleigh atmosphere and the second is a pure Rayleigh atmosphere plus ozone. The last three include aerosols. The first of these consists of a standard vertical distribution, while the last two have distributions attempting to simulate stratospheric volcanic dust layers. The results from the spherical model are compared to flat atmosphere results and a brief discussion on the possibilities of inverting these results is given. Concluding remarks and future work are discussed in Chapter 6.

CHAPTER II

THEORY

Although the radiative transfer equation is simple in form it is difficult to obtain an analytic solution to a general problem in the earth's atmosphere. Only with the relatively recent advent of high speed computers has it become possible to routinely solve the radiative transfer equation for a variety of situations. In this chapter, the radiative transfer equation in differential and integral form is presented. In Section 2.1, the forms of these equations are give in terms of an arbitrary distance variable. Section 2.2 gives the differential form of the radiative transfer equation applied to a plane-parallel homogeneous atmosphere. The spherical atmosphere case is presented in Section 2.3.

2.1 The General Radiative Transfer Equation

The radiative transfer equation is essentially a statement of the conservation of energy. In words, the change in intensity along a given path is due to scattering into and out of the path, assuming there are no sources due to emission along the path. Here, and throughout the remaining, the term "intensity" is defined as the radiant energy per unit solid angle passing thru unit area normal to its direction of propagation per unit time and wavelength. This is alternatively referred to as the radiance. Omitting the derivation of the radiative transfer equation here for brevity and following the form of Chandrasekhar(1960), the differential form of the general radiative transfer equation may be stated as

$$-\frac{1}{K_{T\lambda}(s)} \frac{dI_{\lambda}(s, \omega)}{ds} = I_{\lambda}(s, \omega) - J_{\lambda}(s, \omega) \quad (2.1)$$

where

$$K_{T\lambda}(s) = \rho \kappa_{T\lambda}(s) \quad (2.2)$$

For a rigorous derivation of (2.1) the reader is directed to Chandrasekhar(1960), Sobolev(1963), or any of a number of similar texts. Here $I_{\lambda}(s, \omega)$ is the specific monochromatic intensity at the point s in the direction ω , $K_{T\lambda}(s)$ is the total volume extinction coefficient. $K_{T\lambda}(s)$ has also been given as the product of the density, ρ , and the total mass extinction coefficient, $\kappa_{T\lambda}(s)$. The units of $K_{T\lambda}(s)$ are inverse distance. The last term on the right hand side is the source term which describes how energy travelling in all directions is scattered into the direction ω , assuming there is no emission. The source term may be written

$$J_{\lambda}(s, \omega) = p(\omega, \omega_0)F_{\lambda}(s, \omega_0) + \frac{1}{4\pi} \int_0^{4\pi} p(\omega, \omega')I_{\lambda}(s, \omega')d\omega' \quad (2.3)$$

where

$$\frac{1}{4\pi} \int_0^{4\pi} p(\omega, \omega')d\omega' = \varpi_0 \leq 1 \quad (2.4)$$

ω_0 is the direction in which the solar beam is travelling, $F_{\lambda}(s, \omega_0)$ is the monochromatic solar flux density at the point s travelling in the direction ω_0 , $p(\omega, \omega')$ is the phase function, ϖ_0 is the single scattering albedo, and there are no sources due to emission. The definition of flux density as used in the current work, implicitly assumes that the energy is plane-parallel and thus travelling in only one direction. The solar beam will be assumed plane-parallel throughout this work and thus is uni-directional. Although the solar beam is not truly plane-parallel, this approximation will not result in large errors. The phase function

describes how much energy from the direction ω' is scattered into the direction ω . As stated previously, (2.3) ignores internal emissions.

The source term may be viewed as the sum of single and multiple scatter contributions. The single, or primary, scatter is the first term on the right hand side of (2.3). This term refers to scattering of the plane parallel solar beam. The second term in (2.3) is the multiply scattered light. This term refers to scattering of the diffuse radiation field. In this dissertation, the term **multiple** scatter is reserved for this portion of the intensity. The sum of the single and the multiple terms will constitute the **total** intensity.

Since the current work will only consider monochromatic light, the λ subscript will be dropped. The solution to the general radiative transfer equation can be shown to be(Chandrasekhar(1960)

$$I(s, \omega) = I(0, \omega)e^{-\int_0^s K_T(s')ds'} + \int_0^s J(s', \omega)e^{-\int_{s'}^s K_T(s'')ds''} K_T ds' \quad (2.5)$$

where $I(0, \omega)$ is the specific intensity at the point $s=0$ in the direction ω . If the optical depth, $\tau'(s, s')$, is defined as

$$\tau'(s, s') = \int_{s'}^s K_T(s')ds' \quad (2.6)$$

then (2.5) may be rewritten as

$$I(s, \omega) = I(0, \omega)e^{-\tau(s, 0)} + \int_0^s J(s', \omega)e^{-\tau'(s, s')}d\tau' \quad (2.7)$$

Equation (2.7) states that the total intensity at the point s , in the direction ω , arises from two causes. The first, related to the first term on the right hand side of (2.7), is the directly transmitted radiation. This is radiation incident at

the boundary of the medium that has passed entirely through the medium. The transmitted radiation is also known as the Beer's Law term. The second term in (2.7) refers to that part of the radiation that is scattered into the direction ω between the points 0 and s, and is transmitted to s.

In the case of conservative scattering, that is no absorption, the single scattering albedo is unity. Then if the flux density through a unit area whose normal is \vec{n} , is given by

$$\pi F = \int_0^{4\pi} \vec{I}(s, \omega') \cdot \vec{n} d\omega' \quad (2.8)$$

it can be shown that

$$\frac{dF_x}{dx} + \frac{dF_y}{dy} + \frac{dF_z}{dz} = 0 \quad (2.9)$$

where x, y, and, z define a set of three mutually perpendicular directions. Equation (2.9) is similar to Gauss' Law in electromagnetic theory. Simply stated, the amount of energy entering a volume must equal the amount leaving if there are no sources or sinks in the volume. This will be used as a check of the model developed in the current work.

2.2 The Radiative Transfer Equation in a Flat Atmosphere

To this point, equations (2.1) and (2.5) are independent of geometry. In many applications, the earth's atmosphere may be assumed to be plane-parallel and homogeneous. That is, the atmosphere is considered to be flat without horizontal inhomogeneities. The reader is directed to the previously mentioned sources for a rigorous derivation of (2.1) as applied to this problem. If the flat atmosphere assumption is made, (2.1) may be restated as

$$\frac{\cos\theta}{K_T(z)} \frac{dI(z, \theta, \phi)}{dz} = I(z, \theta, \phi) - J(z, \theta, \phi) \quad (2.10)$$

where z is the vertical coordinate, θ is the polar zenith angle measured from the vertical axis, and ϕ is the azimuth angle. The dependency on x and y vanishes because of the horizontal homogeneity assumption. In terms of a vertical optical depth, $\tau(z)$, defined as

$$\tau(z) = \int_z^{\infty} K_T(z') dz' \quad (2.11)$$

(2.10) may be written as

$$-\mu \frac{dI(\tau, \theta, \phi)}{d\tau} = I(\tau, \mu, \phi) - J(\tau, \mu, \phi) \quad (2.12)$$

where $\mu = \cos\theta$. The advantage of assuming a flat atmosphere, is that once the intensity field has been obtained at a given point, this field is valid anywhere in the atmosphere at the same height. To solve (2.12) a Gauss-Sidel iteration technique was developed by Herman(1963) and Herman and Browning(1965). This technique utilizes the fact that intensity fields are identical at the same level to find the intensities along the path over which (2.12) will be solved. In the current work, the Gauss-Sidel approach is applied to (2.5) for spherical geometry. The problem with spherical geometry is that the horizontal homogeneity is no longer valid, thus complicating the path integration.

2.3 The Radiative Transfer Equation in a Spherical Atmosphere

As mentioned, the flat atmosphere solution is sufficiently accurate in most earth atmosphere situations. It does fail to simulate accurately radiative transfer in the atmosphere as the cosines of the viewing and solar zenith angles become small. The problem cannot be solved for cases where $\mu_0 \leq 0$ and solutions for flat and spherical atmospheres differ largely for situations where $\mu \leq 0$ and the

paths do not strike the ground. These tangent line of sights were illustrated in Fig. 1.1.

In these cases it becomes necessary to include the effects of sphericity. Using the center of the planet as the origin and the z -axis parallel to the solar beam, Lenoble and Sekera(1961) showed that

$$\begin{aligned} & \left\{ \left[\mu\mu_0 + (1 - \mu^2)^{\frac{1}{2}}(1 - \mu_0^2)^{\frac{1}{2}} \cos(\phi_0 - \phi) \right] \frac{\partial}{\partial r} \right. \\ & - \frac{1}{r} \left[\mu(1 - \mu_0^2)^{\frac{1}{2}} - (1 - \mu^2)^{\frac{1}{2}} \mu_0 \cos(\phi_0 - \phi) \right] \frac{\partial}{\partial \mu_0} \\ & \left. - \frac{1}{r} \left[\frac{(1 - \mu^2)^{\frac{1}{2}}}{(1 - \mu_0^2)^{\frac{1}{2}}} \sin(\phi_0 - \phi) \right] \frac{\partial}{\partial \phi_0} \right\} I(r, \mu_0, \phi_0, \mu, \phi) = \\ & -K_T(r, \mu_0, \phi_0) [I(r, \mu_0, \phi_0, \mu, \phi) - J(r, \mu_0, \phi_0, \mu, \phi)] \end{aligned} \quad (2.13)$$

where r describes the radial distance from the origin. Often it is more convenient to treat the local zenith as the z -axis. In this case (2.13) becomes(Lenoble and Sekera(1961))

$$\begin{aligned} & \left\{ \frac{(1 - \mu^2)^{\frac{1}{2}}(1 - \mu_0^2)^{\frac{1}{2}}}{r} \cos(\phi_0 - \phi) \frac{\partial}{\partial \mu_0} \right. \\ & + \frac{(1 - \mu^2)^{\frac{1}{2}}(1 - \mu_0^2)^{\frac{1}{2}}}{r} \left[\frac{\mu_0}{(1 - \mu^2)} \sin(\phi - \phi_0) \frac{\partial}{\partial(\phi - \phi_0)} \right] \\ & \left. + \mu \frac{\partial}{\partial r} + \frac{1 - \mu^2}{r} \frac{\partial}{\partial \mu} \right\} I(r, \mu_0, \phi_0, \mu, \phi) = \\ & -K_T(r, \mu_0, \phi_0) [I(r, \mu_0, \phi_0, \mu, \phi) - J(r, \mu_0, \phi_0, \mu, \phi)] \end{aligned} \quad (2.14)$$

Even with $J(r, \mu_0, \phi_0, \mu, \phi)=0$, there is no analytic solution. One of the difficulties in solving (2.14) is that μ and μ_0 are functions of distance even though the

radiation is travelling in straight lines. Because of the difficulties encountered in solving this form of the radiative transfer equation, the current work concentrates on (2.5). To solve for the spherical case, all angles and paths are computed according to spherical geometry. By using (2.5), the complicated nature of the geometry is handled such as to allow the physics of the problem to be more easily studied.

CHAPTER III

METHOD

In this chapter the actual method of solution is discussed. The method relies on a Gauss-Sidel iteration technique similar to that developed by Herman(1963) and Herman and Browning(1965) for the plane-parallel atmosphere. Because of sphericity, several differences arise between the flat atmosphere Gauss-Sidel and the spherical model developed here. These differences are discussed in the first section of this chapter. The coordinate system and conical boundary are presented in Section 3.2. Section 3.3 applies the radiative transfer equation to the current work. Sections 3.4 to 3.6 are devoted to the method of solution. The single scatter, which is the first iteration of the Gauss-Sidel process, is covered in Section 3.4. The multiple scatter on the z-axis is discussed in Section 3.5, while the same quantity on the conical boundary is covered in Section 3.6. Finally, in Section 3.7, a brief description of the Gauss-Sidel process is given.

3.1 Differences Between the Flat and Spherical Cases

As illustrated in Fig. 1.1, there are many differences between the flat and spherical atmospheres which may be traced to differences in the geometrical and optical path lengths. When examining the paths for upward travelling radiation, it is apparent that some of these paths will be tangent to a given spherical shell within the atmosphere. These tangencies cause the geometrical path lengths for the spherical case to greatly exceed those of the flat atmosphere if the level of tangency is in the lower part of the atmosphere. For those paths that are

tangent in the upper part of the atmosphere, the geometric path length in the plane-parallel atmosphere can greatly exceed that of the spherical. In addition, the path in the spherical case may not reach the optically thicker portions of the atmosphere further reducing the optical path.

It is not only the differences in the path lengths of the scattered radiation that cause the flat and spherical solutions to differ, but also differences in solar path. In cases where the sun is above the horizon, the geometrical and optical paths of the solar beam are smaller in the spherical case than in the flat. For solar angles greater than ninety degrees, a comparison cannot be made since the plane-parallel model does not allow a sub-horizon sun. The angle of incidence of the solar beam also creates differences. As shown in Fig. 3.1(a), the incident solar angle in the flat atmosphere is constant throughout the atmosphere, while it is variable in the spherical case(Fig 3.1(b)).

The angular and path differences by themselves would not be a hindrance since the geometry effects, though complicated, can be determined. The problem is that the spherical geometry leads to inhomogeneities over a given shell along a constant height level. In the flat atmosphere, all points at a given level have identical intensity fields. Referring to Fig. 3.1(a), the intensity fields at the three points along X, Y, and Z are identical. The solution need only be known along one vertical axis to know the solution at all points in the atmosphere. This greatly simplifies the path integration of (2.7). In the spherical case(Fig 3.1(b)) the intensity fields are different at each of the three points shown. To accurately compute the path integration, the intensity field would have to be computed at each level along the path through the atmosphere. Even for today's high speed computers, this is a formidable problem that cannot be done on a routine basis.

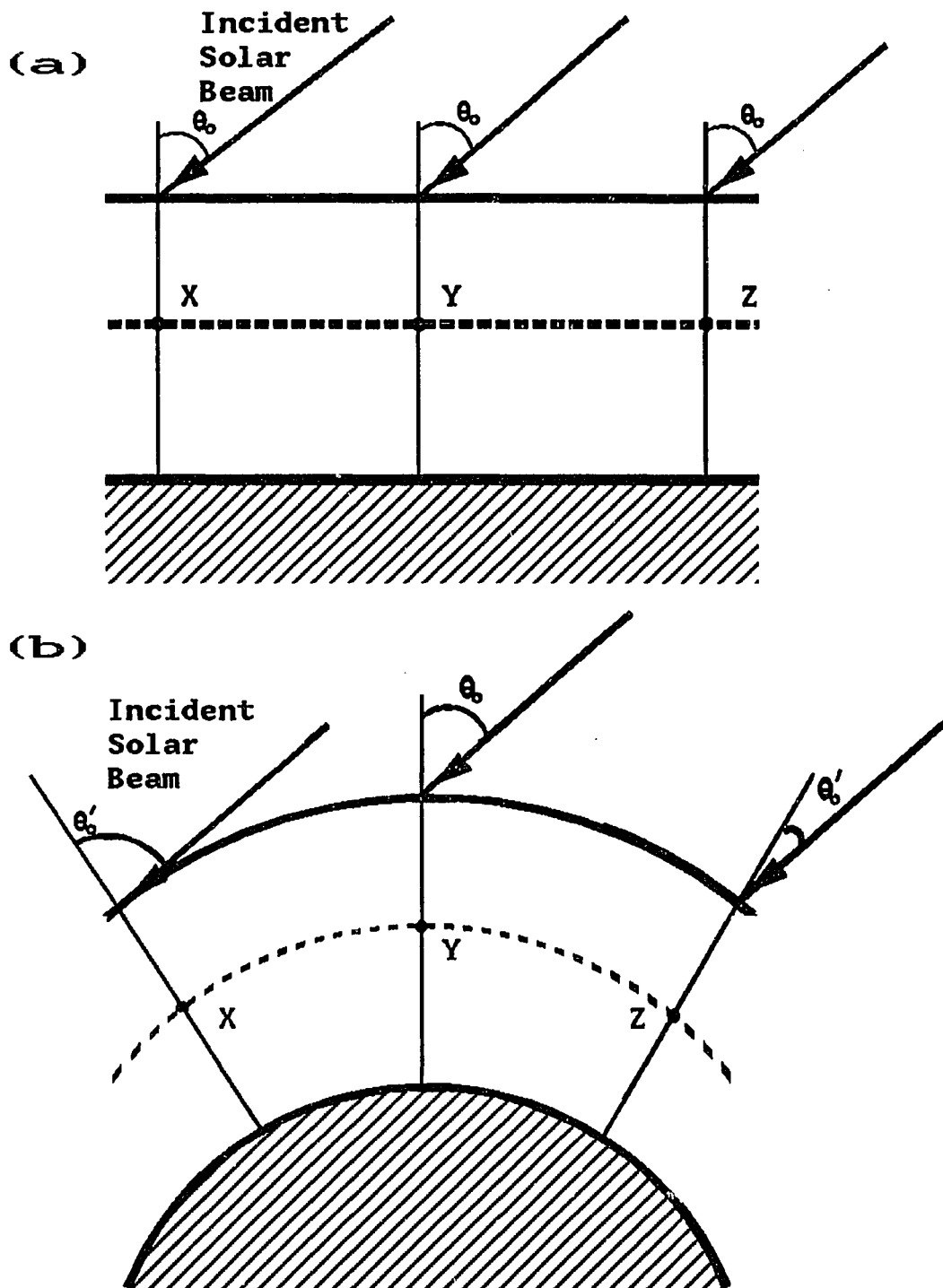


Figure 3.1 Illustration demonstrating the change in solar zenith angle at the top of the atmosphere.

To overcome this problem, a conical boundary is introduced which is discussed in future sections.

3.2 Coordinate System and Conical Boundary

To fully describe the intensity at a point in the atmosphere, seven independent variables are used. Three of these variables, z , ψ , and η , define the location of a point in the coordinate system; θ and ϕ define the direction of propagation of a diffuse beam of radiation; and θ_0 and ϕ_0 define the direction of propagation of the incident solar beam. The z -axis is defined by the line passing through the center of the planet and the desired solution point. The height, z , is measured along this axis with a value of zero corresponding to the surface of the planet. The total height of the atmosphere is designated as Z_0 and the radius of the planet is R_0 . Thus, z takes on values ranging from 0 at R_0 , to Z_0 at the top of the atmosphere. The atmosphere is divided into homogeneous spherical shells with the height of the l^{th} level defined as z_l . The method of dividing the atmosphere is discussed in Appendix A. Resulting heights from the model are given for each z_l along the z -axis, which is also referred to as the zenith.

The polar zenith angle of a beam of radiation, θ , is measured relative to the z -axis. A value of θ between zero and ninety degrees indicates that the radiation is travelling downward. For values between ninety and 180 degrees, the radiation is travelling upward. The model allows θ to take on discrete values designated as θ_i , and the model gives results at these angles only. The solar zenith angle, θ_0 , is the polar zenith angle made by the solar beam with the z -axis. It must be kept in mind that both θ and θ_0 are always measured relative to the z -axis and

not any other radial line. The direction of the solar beam is also described by the solar azimuth angle, ϕ_0 . For simplicity, the zero azimuth plane is defined by the plane containing the z-axis and the solar beam. Then, by definition, ϕ_0 is zero. The azimuthal angle of an arbitrary diffuse beam, ϕ , is measured relative to this plane and allowed to take on discrete values, ϕ_j . A value of zero degrees for ϕ indicates that the radiation is travelling in the same azimuthal direction as the solar beam, while a value of 180 degrees indicates that the propagation is opposite to the solar beam. From this point forward, the designations θ_0 and ϕ_0 are omitted when describing the intensity, but the dependency is still implied. Figure 3.2(a) illustrates the first five variables where the zero azimuth plane coincides with the paper.

The last two variables along with the height variable, z , describe the location of a point in the coordinate system. The angle between the z-axis and a radial line that forms a local zenith is designated by ψ . A conical boundary is formed by the rotation of the radial line that is ψ_0 degrees from the z-axis. To define a location on this cone, the cone azimuth, η , is used. As with the other variables, η takes on discrete values, η_k , and is measured relative to the zero-azimuth plane in the same direction as ϕ . Intensity distributions will be determined at each z_i and η over this conical boundary as well as along the zenith. Fig. 3.2 (b) illustrates η , ψ , and ψ_0 . It is important to emphasize the difference between ϕ and η . The location on the ψ_0 boundary is indicated by η , while the azimuthal direction of propagation of the radiation is indicated by ϕ , regardless of whether the point of interest is on the zenith or the cone. Also, it should be reiterated that θ and θ_0 are measured relative to the zenith, or z-axis, and not with respect to any other radial line that defines a local zenith.

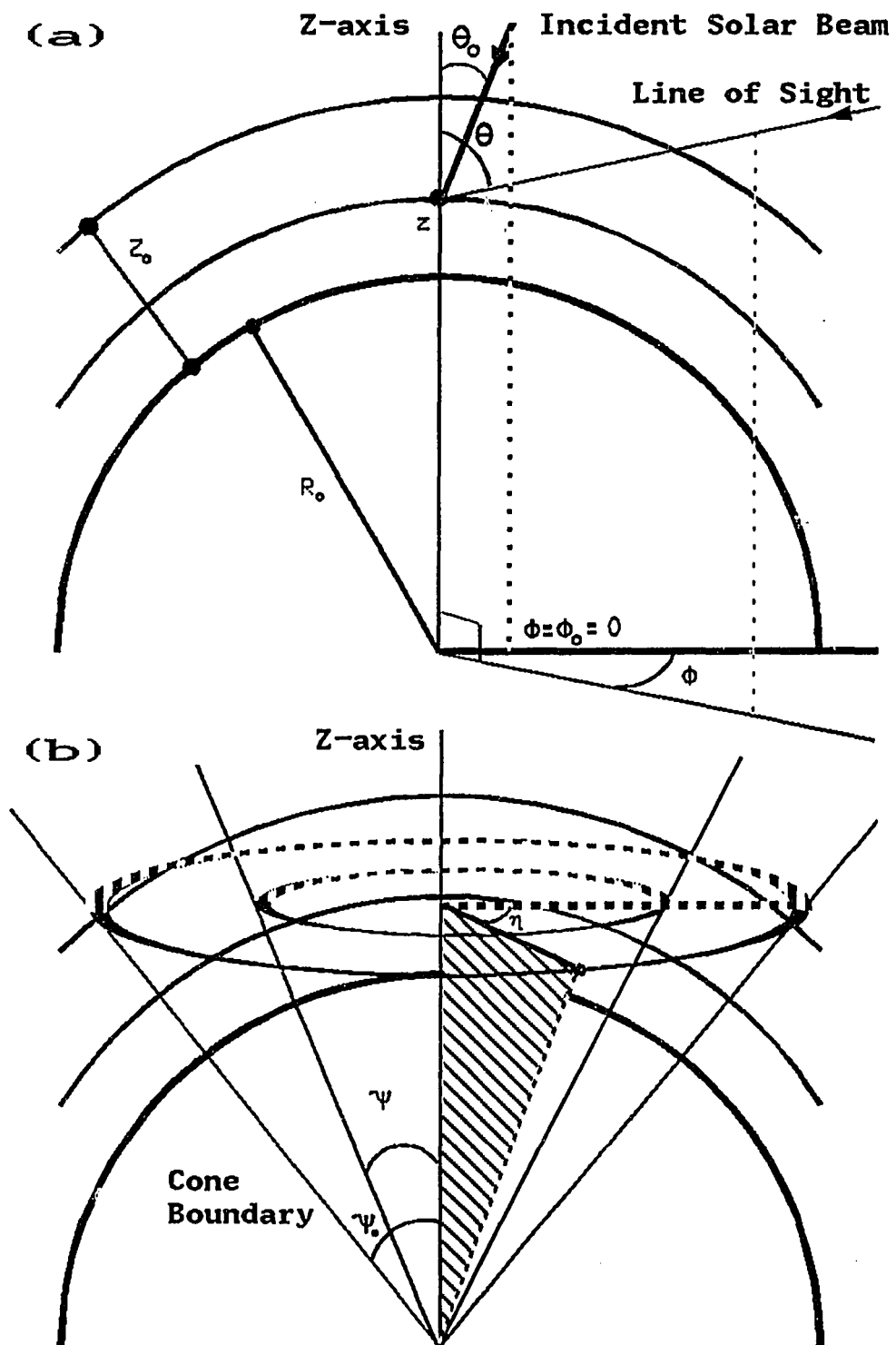


Figure 3.2 Coordinates used in the current method.

3.3 Application of the Radiative Transfer Equation

The solution to the general radiative transfer equation was given in Chapter 2. Restated here, it is

$$I(\tau_T(s, 0), \omega) = I(0, \omega)e^{-\tau_T(s, 0)} + \int_0^{\tau_T(s, 0)} J(\tau'(s', 0), \omega)e^{-(\tau_T(s, 0) - \tau'(s', 0))} d\tau' \quad (3.1)$$

where the optical depth along the path is assumed to vary from a value of zero at the point where the path exits the atmosphere or strikes the surface, to a value of τ_T at the point of solution. By assigning values to τ in this manner there is no need for upward and downward solutions. This equation is for arbitrary geometry and can be used for a spherical atmosphere as long as s and τ are computed properly. The definition of $J(\tau'(s', 0), \omega)$ was given in Chapter 2 in terms of the sum of single and multiple scattering. Eq. (3.1) may be rewritten utilizing the fact that both the source term due to scattering only and the incident term may be written as sums of single and multiple scatter contributions. Thus

$$I(\tau_T(s, 0), \omega) = I_{ss}(0, \omega)e^{-\tau_T(s, 0)} + I_{ms}(0, \omega)e^{-\tau_T(s, 0)} + \int_0^{\tau_T(s, 0)} [J_{ss}(\tau'(s', 0), \omega) + J_{ms}(\tau'(s', 0), \omega)]e^{-(\tau_T(s, 0) - \tau'(s', 0))} d\tau'. \quad (3.2)$$

Combining the single scatter terms yields

$$I(\tau_T(s, 0), \omega) = I_{ss}(\tau_T(s, 0), \omega) + I_{ms}(0, \omega)e^{-\tau_T(s, 0)} + \int_0^{\tau_T(s, 0)} J_{ms}(\tau'(s', 0), \omega)e^{-(\tau_T(s, 0) - \tau'(s', 0))} d\tau' \quad (3.3)$$

where

$$I_{ss}(\tau_T(s, 0), \omega) = I_{ss}(0, \omega)e^{-\tau_T(s, 0)} + \int_0^{\tau_T(s, 0)} J_{ss}(\tau'(s', 0), \omega)e^{-(\tau_T(s, 0) - \tau'(s', 0))} d\tau'. \quad (3.4)$$

The general form of (3.3) is that used in the current work. This equation is modified somewhat such that the path integration of the source term is only performed in the last layer, and not for the entire path through the atmosphere. Then the incident multiple scatter term is the intensity in the given direction at the point on the boundary, and not at the top or bottom of the atmosphere as in (3.3). Fig. 3.3 illustrates this. The intensity on the z-axis at the level D is due to scattering into the path along the entire path A'' to D and is found by computing the single scatter and the multiple scatter contribution separately. The multiple scatter contribution is found in two parts as is given in (3.3) except now, only the bottom layer is considered. The first part of the multiple scatter contribution is the incident multiple scatter intensity at C' while the second part is the integral of the source term between C' and D. The first term (i. e. the incident term) is obtained through a combination of interpolation and numerical techniques. These topics are elaborated in further detail in future sections.

3.4 Single Scatter Calculation

As just stated, the current technique first solves for the total single scatter intensities at each grid point by integrating along the entire path of each line of sight. This is the first iteration of the Gauss-Sidel and consists of solving for the single scatter intensity at all θ_i and ϕ_j for each z_l on the zenith, and for each η_k on the ψ_0 conical boundary. Introducing the dependency of the intensity and the optical depth on the previously described variables, the single scatter intensity

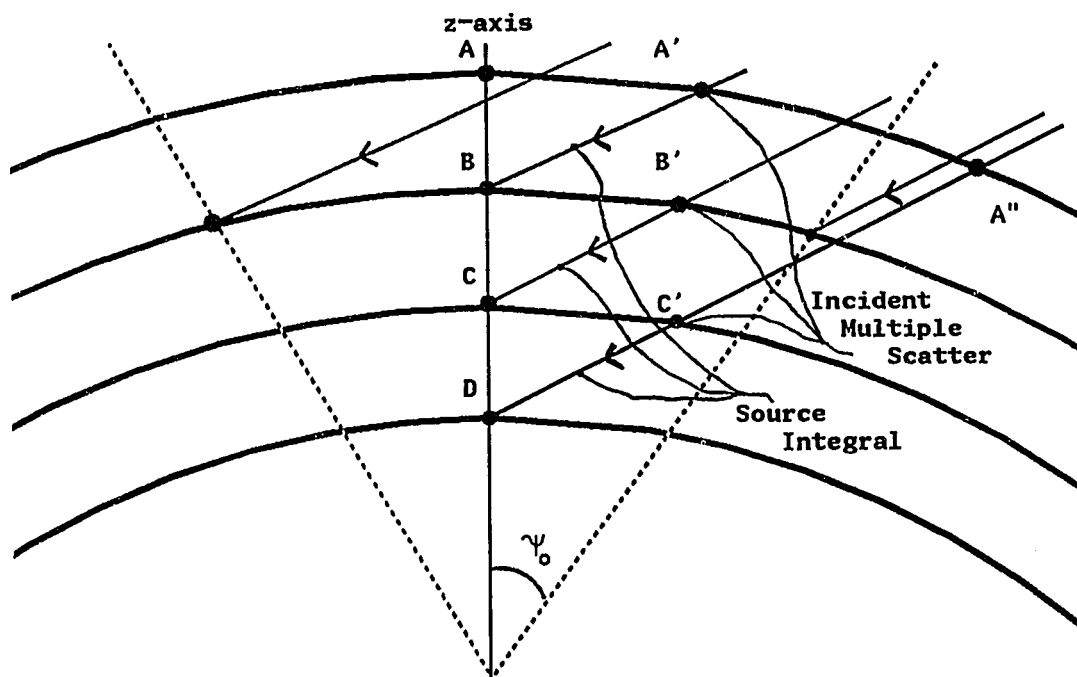


Figure 3.3 Diagram illustrating the incident intensities and layers used to compute the multiple scatter contribution and also the numerical method approximation of the source integral

may be written

$$I_{ss}(z, \theta, \phi, \psi, \eta) = \int_0^{\tau_T(z, \theta, \phi, \psi, \eta)} F(z', \theta_0, \phi_0) P(\theta, \phi, \theta_0, \phi_0, z') e^{-(\tau_T(z, \theta, \phi, \psi, \eta) - \tau'(z', \theta, \phi, \psi', \eta))} d\tau' \quad (3.5)$$

where the incident single scatter intensity at the top or bottom of the atmosphere has been assumed to be zero and $\tau_T(z, \theta, \phi, \psi, \eta)$ is the total optical depth along the entire path within the atmosphere from the observation point defined by z , ψ , and η , and in the direction θ and ϕ . Here the path has been defined using the coordinate variables described in Section 3.2 as opposed to the arbitrary distance s . $F(z', \theta_0, \phi_0)$ is the solar flux density at the point τ' along the path and is given by

$$F(z', \theta_0, \phi_0) = F_0 e^{-\tau_s(\tau')} \quad (3.6)$$

where F_0 is the exoatmspheric solar flux and $\tau_s(\tau')$ is the total optical depth along the solar beam from the top of the atmosphere to the point along the line of sight where the optical depth is τ' . This is illustrated in Fig 3.4.

Key points to mention are that θ_0 , θ , ϕ_0 , and ϕ are constant for the path integration while the primed quantities vary along the path, and the optical depths are computed using spherical geometry. If the path of the radiation strikes the ground, a surface reflection term is added to (3.5). In order to solve (3.5), the current work approximates the integral by a summation over the layers through which the radiation passes. In the case shown in Fig 3.4, the integral is calculated for each of the five layers, and these values are summed using the appropriate attenuation factor to yield the single scatter.

The single scattering on the cone is complicated slightly because the polar

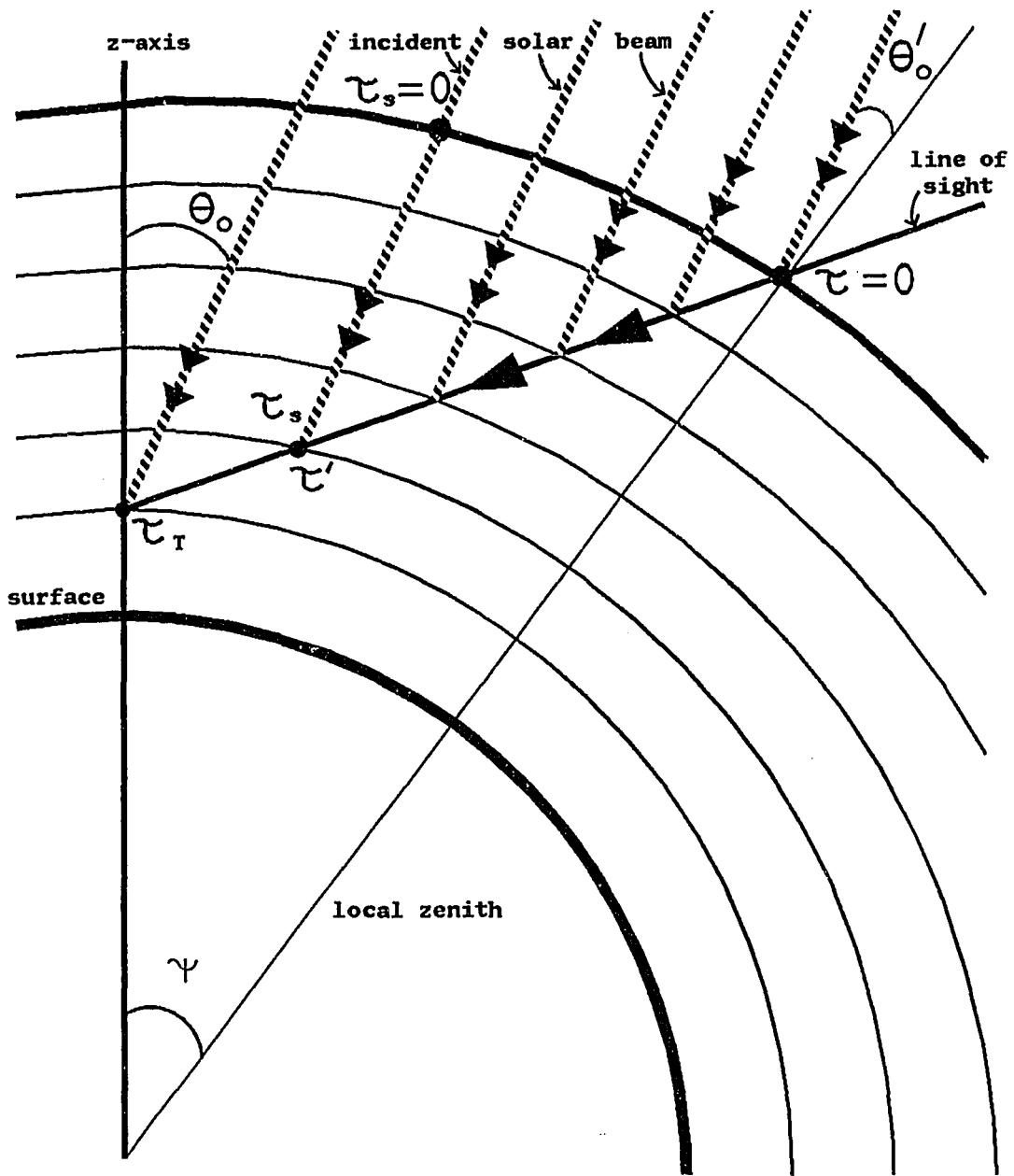


Figure 3.4 Illustration showing the optical depths along the solar path and the line of sight. Also shows the layers used in calculating the single scatter.

angles are measured relative to the z-axis. This is done to ensure that paths on the cone are parallel to those on the zenith. The reason for requiring parallel paths will become evident in future sections. With the computation of the single scatter at all levels and angles, for both the zenith and the cone, the first iteration is complete.

3.5 Zenith Multiple Scatter

Once the single scatter has been computed at each grid point, the more complicated multiple scatter can be calculated. Recalling that the desired solution is for the z-axis, the computation of the multiple scatter contribution along the zenith is discussed first. Then referring to (3.3) and substituting for J_{ms} using (2.3), the multiple scatter at the level z on the z-axis may be written

$$\begin{aligned}
 I_{ms}(z, \theta, \phi, \psi = 0) = & I_{ms}(z(\tau = 0), \theta, \phi, \psi) e^{-\tau_T(z, \theta, \phi, \psi = 0)} + \\
 & \int_0^{\tau_T(z, \theta, \phi, \psi = 0)} \int_0^{2\pi} \int_0^{\pi} I(z', \theta', \phi', \psi') P(\theta, \phi, \theta', \phi', z') \\
 & \times e^{-(\tau_T(z, \theta, \phi, \psi = 0) - \tau'(z', \theta, \phi, \psi'))} \sin \theta' d\theta' d\phi' d\tau'
 \end{aligned}
 \tag{3.7}$$

where the η dependence is omitted because it is undefined on the zenith and the s dependence has been substituted using the coordinate variables described earlier. This equation is for the entire path within the atmosphere, from the point on the zenith to the point where the optical depth is zero, either where the path exits the atmosphere or strikes the ground. As was mentioned at the end of Section 3.3, the current work modifies (3.7) such that the integral is only over the path within the last layer, which requires that the incident multiple scatter term (*i. e.* the first term on the right hand side) be the intensity in the given direction incident where the radiation enters the last layer. Referring to Fig 3.3,

these would be the points A' , B' , and C' , for the solution points on the z -axis for levels B, C, and D respectively. Fig 3.5 illustrates what is meant by the "last layer" and the "boundary." In this figure are shown three cases in which the boundary is indicated by the dotted line. The $+$ subscript is used to denote the point where the path strikes the boundary, no matter if this is above or below the current level. When at a given level z , the top and bottom boundaries are then defined by the current level, the level above as in Fig 3.5(a) or the level below as in Figs. 3.5(b) and (c), and the side boundaries are defined by the $\psi = \psi_0$ cone. The cone boundary is important in cases such as that shown in Fig 3.5(c). Using this notation, (3.7) may be rewritten in terms of the multiple scatter intensity incident on the boundary at the point τ_+ , and the source integral for the path within the boundary. Thus

$$\begin{aligned}
 I_{ms}(z, \theta, \phi, \psi = 0) &= I_{ms}(z_+, \theta, \phi, \psi) e^{-\tau_L(z, \theta, \phi, \psi)} + \\
 &\int_0^{\tau_L(z, \theta, \phi, \psi)} \int_0^{2\pi} \int_0^{\pi} I(z', \theta', \phi', \psi') P(\theta, \phi, \theta', \phi', z') \\
 &\times e^{-(\tau_L(z, \theta, \phi, \psi) - \tau'(z', \theta, \phi, \psi'))} \sin\theta' d\theta' d\phi' d\tau'
 \end{aligned} \tag{3.8}$$

where τ_L is the layer optical depth defined by $\tau_L = |\tau_T - \tau_+|$, and τ_+ is the optical depth along the path from the top of the atmosphere or surface, to the point where it enters the boundary. By defining τ_L in this fashion, (3.8) maintains the same form as (3.7) only here the incident term is the multiple scatter intensity incident on the boundary not the top or bottom of the atmosphere. The calculation of the various terms of (3.8) is now discussed.

3.5.a The Source Term Integral The integral of the source term in the layer, the second term on the right hand side of (3.8), is found by assuming P to be constant along the path within the layer for any given set of angles, and the

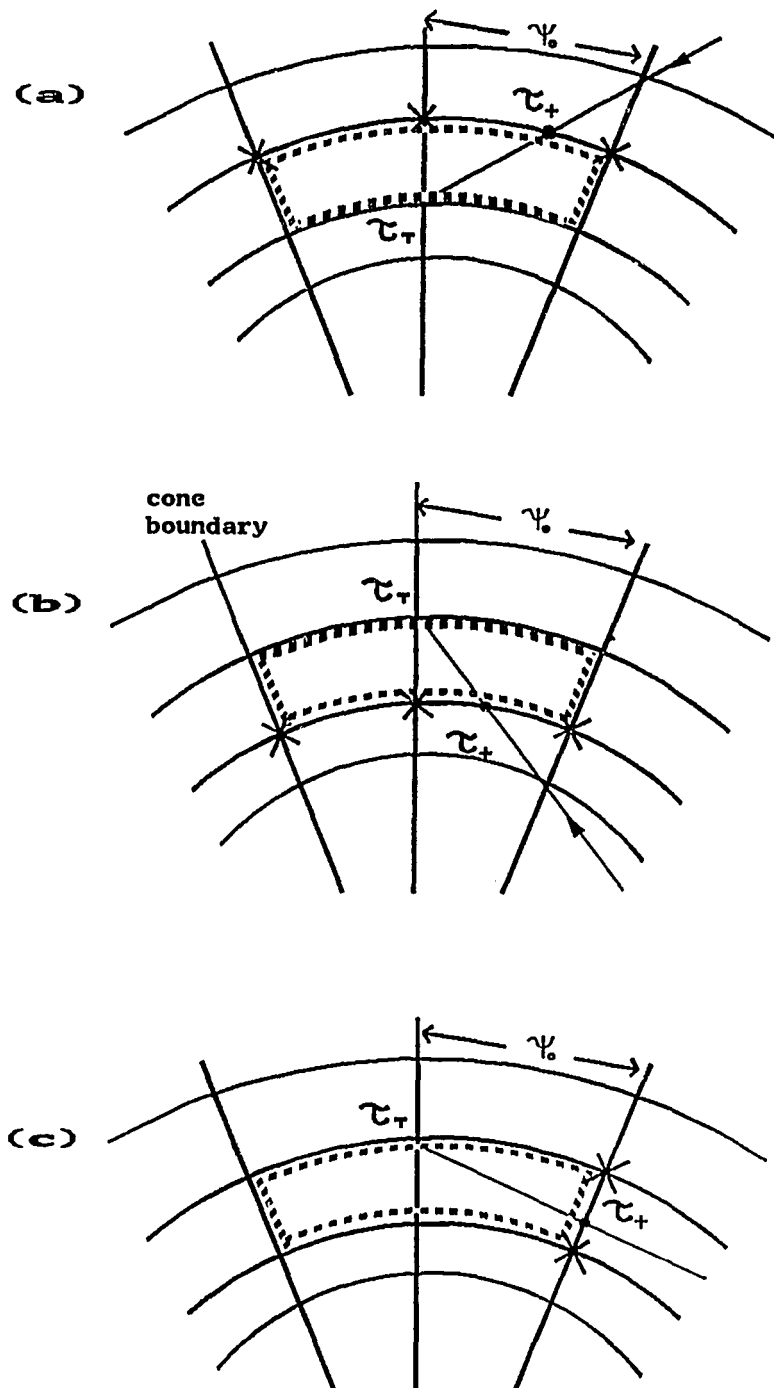


Figure 3.5 Shows the boundary for the three line of sight cases on the zenith as well as the points used for the interpolation of the incident multiple scatter and the intensities used in the calculation of the source term integral

intensity to vary linearly along this path. The path integration over optical depth is then performed analytically, and the solid angle integration is approximated by a summation. Then

$$\begin{aligned}
& \int_0^{\tau_L(z, \theta, \phi, \psi)} \int_0^{2\pi} \int_0^{\pi} I(z', \theta', \phi', \psi') P(\theta, \phi, \theta', \phi', z') \\
& \quad \times e^{-(\tau_L(z, \theta, \phi, \psi) - \tau'(z', \theta, \phi, \psi'))} \sin \theta' d\theta' d\phi' d\tau' \cong \\
& \quad \sum_{i'} \sum_{j'} P_{i'j'} \left\{ I_{i'j'}(z, \psi = 0) \left[\frac{-\tau_L e^{-\tau_L} + 1 - e^{-\tau_L}}{\tau_L} \right] \right. \\
& \quad \left. + I_{i'j'}(z_+, \psi) \frac{(\tau_L - 1 + e^{-\tau_L})}{\tau_L} \right\} \Delta \mu_{i'} \Delta \phi_{j'}
\end{aligned} \tag{3.9}$$

where again τ_L is the optical depth along the path within the boundary, $I_{i'j'}(z, \psi = 0)$ is the intensity at the solution point on the zenith in the direction $\theta_{i'}$ and $\phi_{j'}$, $I_{i'j'}(z_+, \psi)$ is the intensity in the same direction but on the boundary, and $P_{i'j'}$ corresponds to $P(\theta_{i'}, \phi_{j'}, \theta_{i'}, \phi_{j'})$ and is computed as described in Appendix A. The optical depth factors arise from the path integration, assuming a linear variation of the intensities within the layer.

In a plane-parallel model, $I_{i'j'}(z_+, \psi)$ is identical to $I_{i'j'}(z_+, \psi = 0)$ and, since $I_{i'j'}(z_+, \psi = 0)$ is known from previous calculations, no problem is encountered. In the spherical model $I_{i'j'}(z_+, \psi = 0)$ is still known from previous calculations, but it is no longer equal to the value on the boundary because of the lack of horizontal homogeneity. To obtain $I_{i'j'}(z_+, \psi)$ so that the source integral may be computed, the model utilizes the intensity from previous iterations at the zenith on the z_+ boundary, $I_{i'j'}(z_+, \psi = 0)$, and the values at z_+ on the cone $I_{i'j'}(z_+, \psi_0, \eta = \phi_{j'})$, and $I_{i'j'}(z_+, \psi_0, \eta = \phi_{j'} + 180)$ to interpolate a value for $I_{i'j'}(z_+, \psi)$. The method of determining the values on the cone is discussed in

the next section. These points are indicated by the \times 's in Fig 3.5(a) and (b) for the case where $\phi_j=0$ degrees. Then the values used for η are 0 and 180 degrees. As shown in Fig 3.5 (c), there are some cases where the path crosses the cone boundary before the z_+ boundary. In these situations a two point interpolation is utilized using the intensities at the indicated points. The interpolation is performed for each θ_i and ϕ_j in the above summation.

3.5.b The Incident Multiple Scatter Interpolation is also applied to determine the first term on the right hand side of (3.8), $I_{ms}(z_+, \theta, \phi, \psi)$, but with several modifications. Instead of using the total intensities for the interpolation, the multiple to single scatter ratios at the z_+ level along the zenith and on the $\psi = \psi_0$ boundary are used. One reason for using this technique is that the ratio is smoother than the actual intensity, thus allowing a more accurate interpolation. This also allows the known single scatter on the boundary for the given direction to be used. The incident multiple scatter is obtained by multiplying the interpolated ratio by this known single scatter. $I_{ss}(z_+, \theta, \phi, \psi)$ was obtained from the layer by layer summation process described in Section 3.3, for all levels, z_l along the line of sight. By using this known single scatter intensity at the boundary point, a much better estimate of the incident multiple scatter intensity is obtained.

It would also be desirable to use the interpolation of the multiple to single scatter ratio to compute the intensity distribution needed for the source term integral. This is not feasible because the single scatter intensities in all directions at all boundary intersections due to each path would have to be computed explicitly. This is computationally prohibitive. Thus the reason for not employing the ratio interpolation for the source term integral, is that the

single scatter is not known for all the directions on the z_+ boundary. It is known only for the one direction for the given line of sight from the zenith through the point on z_+ . This single scatter intensity has been found without performing any additional computations. In certain cases, the ratios are not used in determining the incident multiple scatter intensity. These are cases where the path exits the boundary through the side (*i. e.* through the $\psi = \psi_0$ cone) as in Fig. 3.5(c), or when the z_+ boundary is the surface. In both of these cases, the single scatter is not known at the boundary point and no advantage is gained by using the ratios. When this occurs, the actual multiple scatter intensities are used in the interpolation.

Once a value of $I_{ms}(z_+, \theta, \phi, \psi)$ is found, it is multiplied by the attenuation factor and added to the source integral to yield $I_{ms}(z, \theta, \phi, \psi = 0)$. This value is added to the previously computed single scatter to give the total intensity, $I(z, \theta, \phi, \psi = 0)$. These values are stored and used for future calculations. At this point it should be evident why parallel lines of sight are maintained on the cone. By doing this, interpolations to determine the incident multiple scatter terms and the intensities used in the source integrals can be performed.

3.6 Cone Multiple Scatter

In solving the zenith multiple scatter, multiple scatter intensities on the cone were used for interpolation. This section describes how the intensities on the cone are computed. As in the zenith case, the problem consists of finding the source integral for the path within the boundary, and adding an attenuated incident boundary term. On the cone, the boundary is defined by the level that the path exits. The three different situations are illustrated in Fig 3.6. Fig 3.6(c)

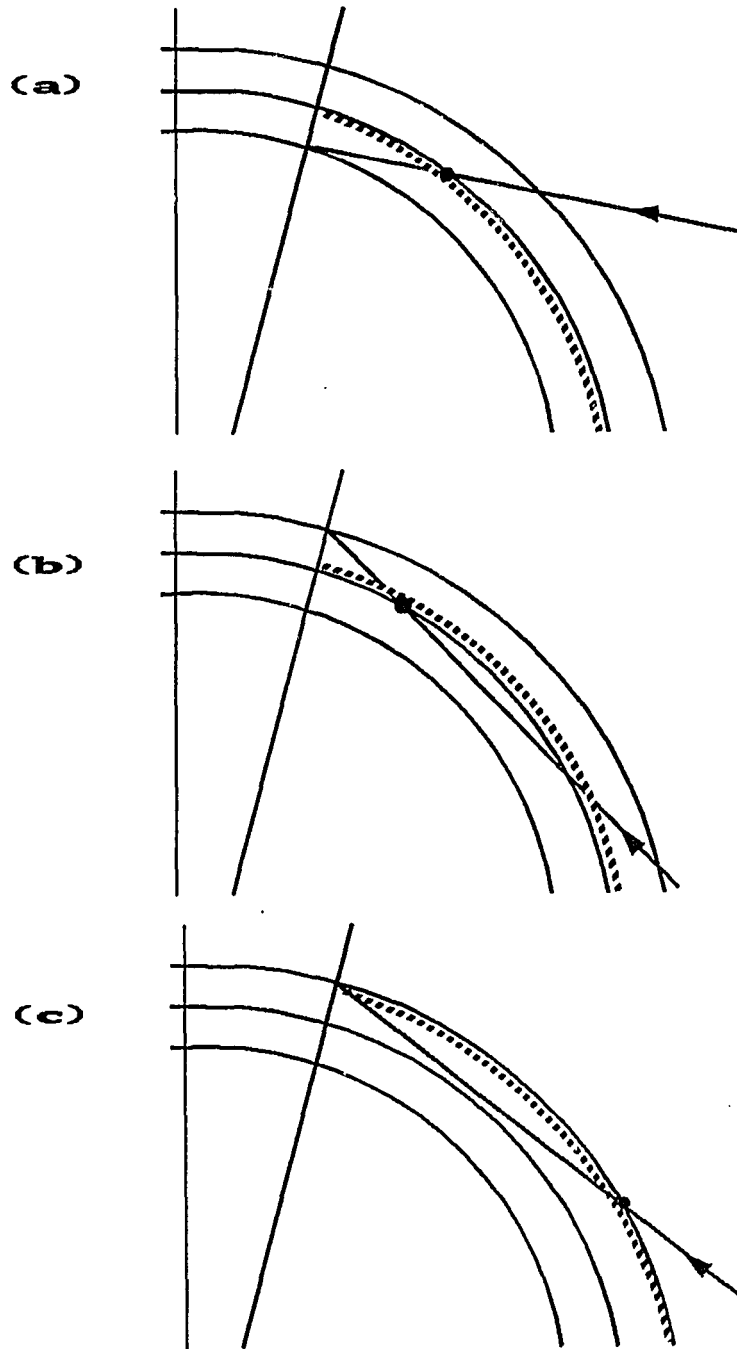


Figure 3.6 Shows the boundary for the three line sight cases on the cone

illustrates the situation where the path becomes tangent within the layer before striking the boundary. This is prevented from happening on the zenith by adding additional layers, but cannot be avoided on the cone without severely hindering the polar angles used or taxing the limits of computation time by adding even more layers. As was used in the previous section, the + subscript designates the point on the boundary.

3.6.a The Source Term Integral The equation used to solve for the cone multiple scatter is of the same form as (3.8) only using $\psi = \psi_0$ and including the η dependence. The source integral of (3.8) is found by a different technique than that of (3.9). It is assumed that the source term integral may be written as

$$\int_0^{\tau_L(z, \theta, \phi, \psi = \psi_0, \eta)} J_{ms}(z', \theta, \phi, \psi', \eta) e^{-(\tau_L(z, \theta, \phi, \psi = \psi_0, \eta) - \tau'(z', \theta, \phi, \psi', \eta))} d\tau' \cong \bar{P}(\psi = \psi_0) \left(\int_0^{2\pi} \int_0^{\pi} \bar{I}(< z >, \theta', \phi', \psi = \psi_0, \eta) d\theta' d\phi' \right) \times \left(\int_0^{\tau_L(z, \theta, \phi, \psi = \psi_0, \eta)} e^{-(\tau_L(z, \theta, \phi, \psi = \psi_0, \eta) - \tau'(z', \theta, \phi, \psi', \eta))} d\tau' \right) \quad (3.10)$$

where τ_L is the optical depth along the path within the boundary, $\bar{P}(\psi = \psi_0)$ is an average phase function over angle for the scattering into the direction θ, ϕ along the path within the layer, and $\bar{I}(< z >, \theta', \phi', \psi = \psi_0, \eta)$ is an average intensity for the layer which is written

$$\bar{I}(< z >, \theta', \phi', \psi = \psi_0, \eta) = \frac{I(z, \theta', \phi', \psi = \psi_0, \eta) + I(z_+, \theta', \phi', \psi = \psi_0, \eta)}{2} \quad (3.11)$$

In (3.10) a value for the integral of the source function along the path within the layer is desired. The two terms in parentheses on the right hand side of this

equation are known, and as before, the solid angle integral is approximated by a summation and the optical depth integral is computed analytically. Thus to find the source term integral, a value for $\bar{P}(\psi = \psi_0)$ must be found. Now, a similar equation to (3.10) may be written for the zenith as well. But, on the zenith the left hand side is known as well as the terms in parentheses. Thus $\bar{P}(\psi = 0)$ can be found using simple algebra. The current work assumes that $\bar{P}(\psi = 0) = \bar{P}(\psi = \psi_0)$. Then $\bar{P}(\psi = 0)$ is used in (3.10) to replace $\bar{P}(\psi = \psi_0)$ and the source term integral is obtained since the other two terms in (3.10) are known.

This source term integral approximation depends primarily on the validity of (3.10) as well as the validity of $\bar{P}(\psi = 0) = \bar{P}(\psi = \psi_0)$. If there are large non-linear changes in the intensity along either the zenith or the cone paths within the boundary, these assumptions are not good. Also important is how similar the paths are to one another. As long as the paths, both geometric and optical, are not too large inside the boundary, the $\bar{P}(\psi = 0) = \bar{P}(\psi = \psi_0)$ assumption should be valid. A more detailed description of these points is given in Chapter 4.

3.6.b The Incident Multiple Scatter The incident term must still be computed. As on the zenith, the ratio of multiple to single scatter is used, as well as the known single scatter on the boundary. Unlike the zenith, no interpolation can be used since there is no data outside the cone. Instead, the multiple to single scatter ratio at $\psi = \psi_0$ and z_+ is assumed to be identical to the ratio at the point where the path exits the boundary. The validity of this assumption depends on how long the path is and how homogeneous the field is. As mentioned in the last section, the multiple to single scatter ratio is smoother than the actual intensity, making this a much better assumption than letting the intensities be

identical at the two points. This technique also allows the known single scatter to be used to give extra information and give a better estimate of the incident multiple scatter intensity. This technique is similar to that used in the Gauss-Sidel flat atmosphere methods, where the incident intensities are obtained by assuming intensity fields at a given level to be identical. The difference is that in the current method the ratio of multiple to single scatter is assumed to be horizontally homogeneous outside the cone.

The attenuated incident term, the source integral for the layer, and the single scatter at the grid point are added to yield an estimate of the total intensity on the cone boundary for the given θ_i and ϕ_j . This process is utilized at each η_k for a given θ_i and ϕ_j . At this point, the single, multiple, and total intensities are known for the given θ_i 's and ϕ_j 's at each grid point along the zenith and on the cone. A brief description of the Gauss-Sidel iteration process given in the next section will clarify how the other angles and levels are computed.

3.7 The Gauss – Sidel Iteration

The first iteration of the Gauss-Sidel consists of computing the single scatter at all levels on the zenith and cone for every θ_i , ϕ_j , and η_k . The second iteration begins with a downward pass through the atmosphere, beginning at Z_0 and ending at the surface. In the downward pass, only polar zenith angles less than ninety degrees are considered. At the top of the atmosphere, the downward intensities are zero.

At the second level, the incident term is evaluated at level one where all intensities are zero for all $\theta < 90$ degrees, as stated above. The process starts by letting i and $j=1$ (recall that i and j are the incremental integers for θ and ϕ).

Using the process described in Section 3.5, the source integral for the first layer is computed on the zenith using the single scatter values which have already been computed. This value is then used to compute \bar{P} on the cone for each value of k (where k is the incremental integer for η) as described in Section 3.6. This \bar{P} along with the single scatter values on the cone allows the calculation of the source integral on the cone. The process then returns back to the zenith where, the source integral for $j=2$ and $i=1$ is found and this value is used on the cone for all k 's to compute the source integral as described above. This zenith to cone process is repeated first for all j 's at a given i , then all i 's at the given level such that $\theta_i < 90$.

The process then continues downward until all levels have been completed. The only difference in these subsequent levels from the second level, is that now an incident multiple scatter term must be included. The incident intensity used in the zenith computations is found using the methods described in Section 3.5 while the incident intensity for the cone is discussed in Section 3.6. Because the intensities at each angle and level are continually updated as they are found, the process is designated as Gauss-Sidel. This updating procedure increases the rate of convergence of the solution.

Once the downward intensities at the surface are computed, a downward flux is calculated. This downward flux is used to calculate a Lambertian surface reflection and, the upward pass begins. Using the surface reflection as the boundary condition, the above process is repeated, working up the atmosphere considering polar angles greater than ninety degrees. By the time the top of the atmosphere is reached, second approximations for the intensity field at each grid point have been calculated. This ends the second iteration. The entire process

of a downward and an upward pass constitutes one iteration.

These iterations are repeated until convergence of the solution is reached. Convergence occurs when the changes in the computed downward flux at the surface, and the upward flux out the top vary by less than 0.5% from the previous iteration. The rate at which the solution converges depends primarily on two factors, solar zenith angle and total optical depth. The larger the solar zenith and the larger the optical depth, the slower the rate of convergence. Typically seven iterations is sufficient for convergence in most earth atmosphere situations.

Recall that in Section 3.3 it was mentioned that the incident intensity was found by a combination of interpolation and numerical techniques. The interpolation technique was discussed in Section 3.5. The numerical technique is now discussed. Referring back to Fig. 3.3, what is ultimately desired is the intensity at the point on the zenith for level D. Since the downward intensities at the top of the atmosphere are assumed to be zero the intensity at level D is the integral of the source term for the path from A'' to D. The numerical techniques utilized in the current work compute this integral along the entire path for the single scatter intensities only. To compute the multiple scatter contribution, the current method starts at the level B and computes this integral for the path from A' to level B. This plus the single scatter yields a total intensity on the z-axis at level B. This is also done for all the points on the conical boundary as well. At level C, on the z-axis, the path integral is computed for the path between B' and C for the line of sight shown. The interpolated incident multiple scatter intensity at B' is attenuated to the z-axis and added to the source integral and single scatter to give the total intensity on the z-axis. But it can be seen that the intensity at B' is essentially the source integral along the path for the first layer.

This integral has been approximated by the interpolation scheme described in Section 3.5. Thus the intensity at level C on the z-axis is effectively the integral of the source term for the entire path, depending on how well the interpolation of the intensity at B' represents the actual path integral.

At level D, the intensity is the sum of the source integral of the path in the layer C to D, the attenuated multiple scatter intensity from C' and the single scatter. Using the same argument as above, the intensity at C' really represents the integral of the source term for the first two layers. Thus the source integral for the path from level A to D has been approximated by the numerical method. Problems arise in this technique when the distance between A' and A'' becomes large. This is because inhomogeneities in the spherical atmosphere make the paths too dissimilar for this process to give accurate results. This problem is somewhat negated by the fact that the intensities from A'' to level B yield only a small percentage of the total intensity at level D on the z-axis because of attenuation. Thus, even though the path from A' to level B may not accurately represent that for A'' to level B, the errors introduced should be small.

CHAPTER IV

RESULTS AND CHECKS

In this chapter, the model is checked for accuracy and compared to results from other spherical models. A description of the considerations that go into selecting the parameters of the model is given in Section 4.1. Also discussed is the effect of the cone solution on the final result. Section 4.2 presents comparisons to flat atmosphere results. The spherical model is run for a case where R_0 is increased by a factor of 100 and the solutions are compared to flat atmosphere results as one of the checks on the model. The model is also run for a normal radius and small solar zenith angle, and the results compared with the flat atmosphere to determine differences. Conservation of energy considerations are discussed in Section 4.3, and a "cone to zenith" comparison is given in Section 4.4. The last section of this chapter compares results for several cases of the current cone method to other previous methods. Two of the methods used for comparison are Monte Carlo techniques while the third is the quasi-spherical technique developed by Asous(1982). In all computations in the current work, the incident solar flux, F_0 , is taken to be unity per unit area normal to the beam.

4.1 Choice of Parameters

As mentioned in Chapter III, several of the variables used in the model have discrete values. The choice of divisions for these variables will have bearing on the final solution. The variables that take on discrete values are z , θ , ϕ , and η . As was shown by Herman(1963), dividing ϕ into thirty degree intervals is sufficient

to accurately describe the intensity field, and this interval will be used in the current work as well. Solutions on the $\psi = \psi_0$ cone are determined at 30 degree intervals in η to keep the grid points compatible with the angular intervals in intensity for the various intensity interpolations required.

The original method developed for the flat atmosphere used eighteen θ angles with ten degree separation. The current model was developed to allow any number of θ angles distributed with uneven increments. The importance of the distribution of θ was investigated by comparing runs of eighteen and thirty-six angles. The eighteen angle runs used the same angles as in the original flat atmosphere Gauss-Sidel. The thirty-six angle runs used these angles, plus others to better define the peaks in the intensity distributions. For a solar zenith angle of 85 degrees, a pure Rayleigh atmosphere of optical depth 0.40, and a surface albedo of 0.8, comparisons of intensities at identical angles for the eighteen and thirty-six angle runs showed differences of less than 1% in all cases. A twenty angle run was also performed. The extra two angles were placed at 92 and 88 degrees. The intensities at these angles when compared to those of the thirty-six angle run, differed by less than 2%. These results indicate that as long as the line of sight angles are well distributed, there is no large impact upon the model results. Whenever possible, the smallest number of angles are used to decrease computation time.

The last variable to take on discrete values is z . The manner in which z is discretized can have a significant impact on the model results. To test the effect of the number of levels and the method of division, the model was run for twenty, thirty, forty and sixty levels. The atmosphere was assumed to be pure Rayleigh with an optical depth of 1.00. The incident solar angle was 85

degrees, surface albedo was 0.8 and eighteen θ angles were used. As described in Appendix A, half of the levels were chosen so that the lower portion of the atmosphere was divided to meet layer optical depth requirements. The other half of the layers were used in the upper portion of the atmosphere to meet geometric requirements. The sixty level runs were also performed with 2/3 and 5/6 of the levels used in the lower part of the atmosphere to reduce the optical depths of each layer. The remaining levels were used to divide the upper portion of the atmosphere using geometric considerations. It should be understood that layers added in the lower portion of the atmosphere serve to reduce the optical depths of the layers, and that the layer optical depths of the upper layers are orders of magnitude smaller than those of the lower atmospheric layers. The geometrical thickness of the upper atmospheric layers may too need to be reduced in order to maintain the spherical nature of the problem.

The results from these runs indicated that as long as the largest layer optical depth is less than 0.025, increasing the number of levels used to divide the lower portion of the atmosphere according to optical depth considerations has less than a 1% influence on the final solution. If the largest layer optical depth is as large as 0.035, the errors induced approach 3%. Also from the results of these runs, it was determined that ten levels are adequate in the upper third of a 50 km atmosphere to adequately account for spherical geometry effects. If less than this number is used, the layers are still thick geometrically to account for the spherical nature of the problem, even though the layer optical depths in this region are small enough so as not to induce errors. Thus, to keep the errors less than 1% in the case of the total optical depth of 1.00, a minimum of fifty levels should be used. Ten of the levels are used for the upper part of the atmosphere

to account for the spherical nature of the problem while the other 40 are used in the lower part of the atmosphere to divide for optical depth.

The next step in the checking process was to examine the effect of the cone angle ψ_0 on the final solution. In choosing ψ_0 several factors must be considered. A large value for ψ_0 would lead to poorer interpolated values. Also, since paths on the zenith and cone are parallel, it is possible for radiation that travels upward on the zenith to travel downward on the cone and vice versa. These paths would be too dissimilar to allow an accurate interpolation. By making ψ_0 small these problems are avoided and the interpolation is accurate. But if ψ_0 is too small, then errors on the boundary for which the intensities are approximate (see Chapter III) will have a larger effect on the solution. Another problem is that more of the paths will exit the side boundary as shown in Fig 3.5 (c). These paths rely on the less accurate two-point interpolation of the multiple scatter intensities. One last point is that a small value for ψ_0 will encompass less of the atmosphere and the Gauss-Sidel approximation for the source integral will be poorer. Taking all of these factors into account, a value of $\psi_0=1.0$ degrees was selected. Runs were performed for $\psi_0=0.5, 0.75, 1.25,$ and 1.5 degrees. Comparisons of the final results showed deviations of less than 1% from the solution obtained using $\psi_0=1.0$ degrees.

Also examined was the effect of the boundary on the final solution. To test this, the boundary intensities were positively biased by three and ten percent each time they were calculated during a given iteration. In the case of the 10% bias, the final boundary values differed from the unbiased solution by as much as 50%. These large errors resulted in the desired z-axis solutions differing by as much as 15%. In the 3% bias, the final cone solutions differed from between

5 and 10%. Differences on the zenith were all less than 2.5%, and most were less than 1%. This indicates that the model can tolerate errors of up to 10% on the boundary without greatly influencing the final solution. In a typical run, there will not be a consistent bias in the boundary as was introduced in this case, thus it will be shown in Section 4.4 that errors will be less than 1% in the final solution due to errors in estimating the boundary.

4.2 Flat Atmosphere Comparison

The first check of the actual results of the model was to compare it with flat atmosphere simulations. To examine the model for programming errors, the spherical model was run letting $R_0=638,000$ km. By doing this, the geometry essentially becomes plane-parallel. The model was run with a solar zenith angle of 85.0 degrees, a pure Rayleigh atmosphere with optical depth of 1.00, albedo of 0.8, and $\psi_0=1.0$ degrees. When the results from this run were compared with results using a flat atmosphere Gauss-Sidel model, the solutions differed by less than 1% at all angles. This indicates that no large programming errors exist

The second flat atmosphere comparison consisted of running the model for a small solar zenith angle and optical depth. While the small solar angle and small optical depth somewhat diminish the spherical effects, the intensities will tend to vary more or less linearly with geometric path lengths. This enables an easier interpretation of the differences between the flat and spherical models. The parameters used were a solar zenith angle of 5 degrees, a pure Rayleigh atmosphere with optical depth of 0.05, and surface albedo of 0.0. The transmitted intensities at the surface for $\phi=0$ and 180 degrees, and for $\phi=60$ and 120 degrees are shown in Figs. 4.1 and 4.2. These figures show good agreement in the

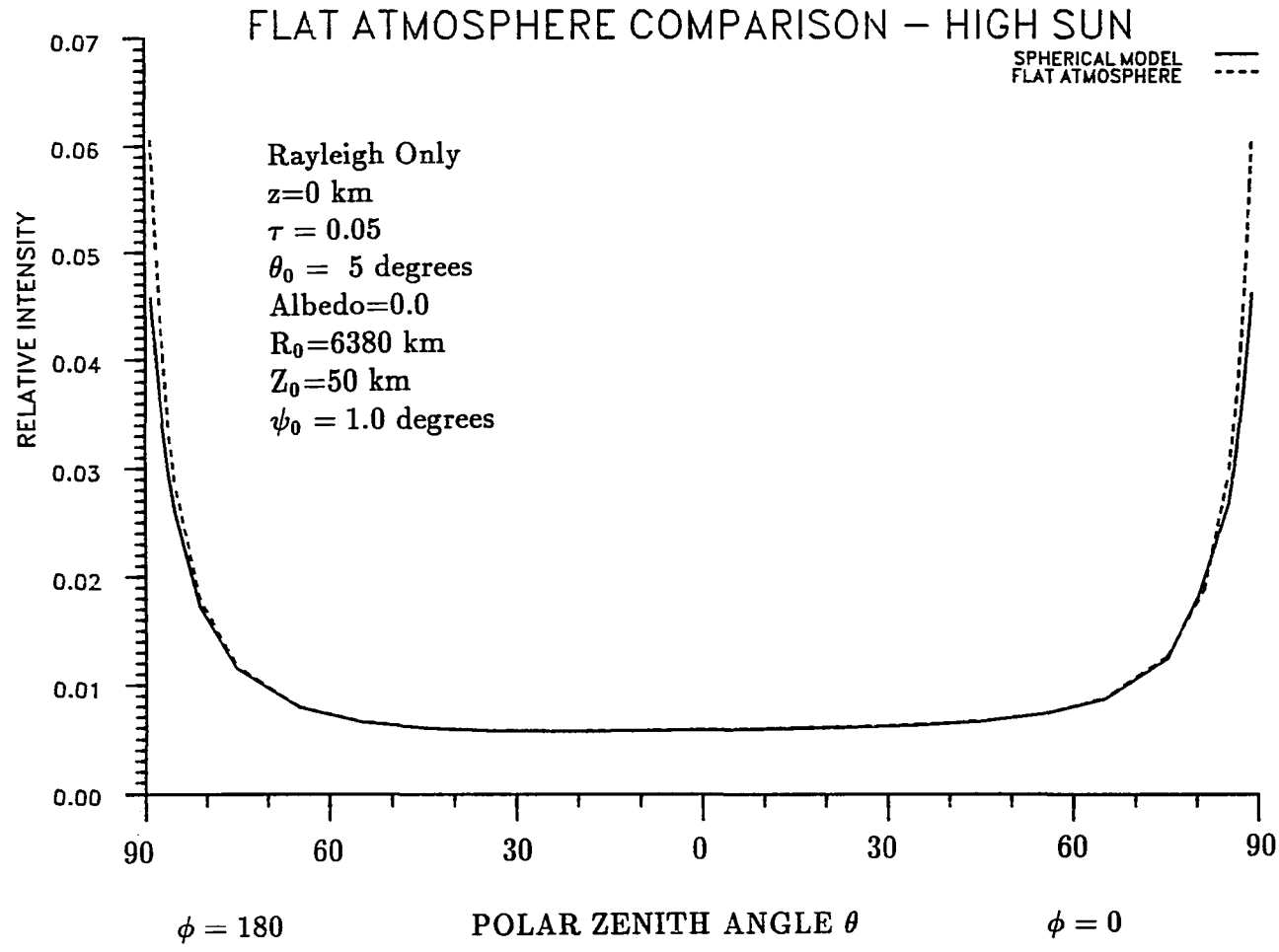


Figure 4.1 Transmitted intensities at the surface for the case of a high sun and small optical depth. Comparison with flat atmosphere results for $\phi=0$ and 180 degrees.

intensities for θ angles up to 80 degrees. For near horizon paths the methods diverge by more than 3%. These results agree with those obtained by Blattner *et. al*(1974), and occur because of the much shorter path lengths in the spherical atmosphere. Because the paths are shorter, one expects the spherical intensities to be smaller than those for the flat solution, and this is indeed the case. This confirms the Monte Carlo results of Collins *et. al*(1972) and Blattner(1977).

Shown in Figs. 4.3 and 4.4 are the reflected intensities at the top of the atmosphere for the above ϕ angles. As is evident from these figures, there is a large discrepancy in the intensities for polar angles less than 110 degrees. This is due primarily to the fact that there are tangent line of sights in a spherical atmosphere. In the case of the flat atmosphere, the longest path lengths occur near ninety degrees. In the spherical atmosphere, the longest path length will be for that line of sight that just grazes the planet's surface. Because of these differences in geometry, at angles between 90 and 95.1 degrees the geometric paths are shorter in the spherical case. Then the intensities at these angles should be smaller in the spherical case. At angles greater than 95.1 degrees the reverse is true and the intensities will be larger in the spherical case. These points are illustrated in the results of the reflected intensity plots(Figs. 4.3 and 4.4).

4.3 Energy Conservation

As was mentioned in Chapter II, in an atmosphere with conservative scattering, that is no absorption, the divergence of the flux is zero. This point may be used in much the same way as the large radius run of the previous section to find programming errors. In the flat atmosphere, flux conservation

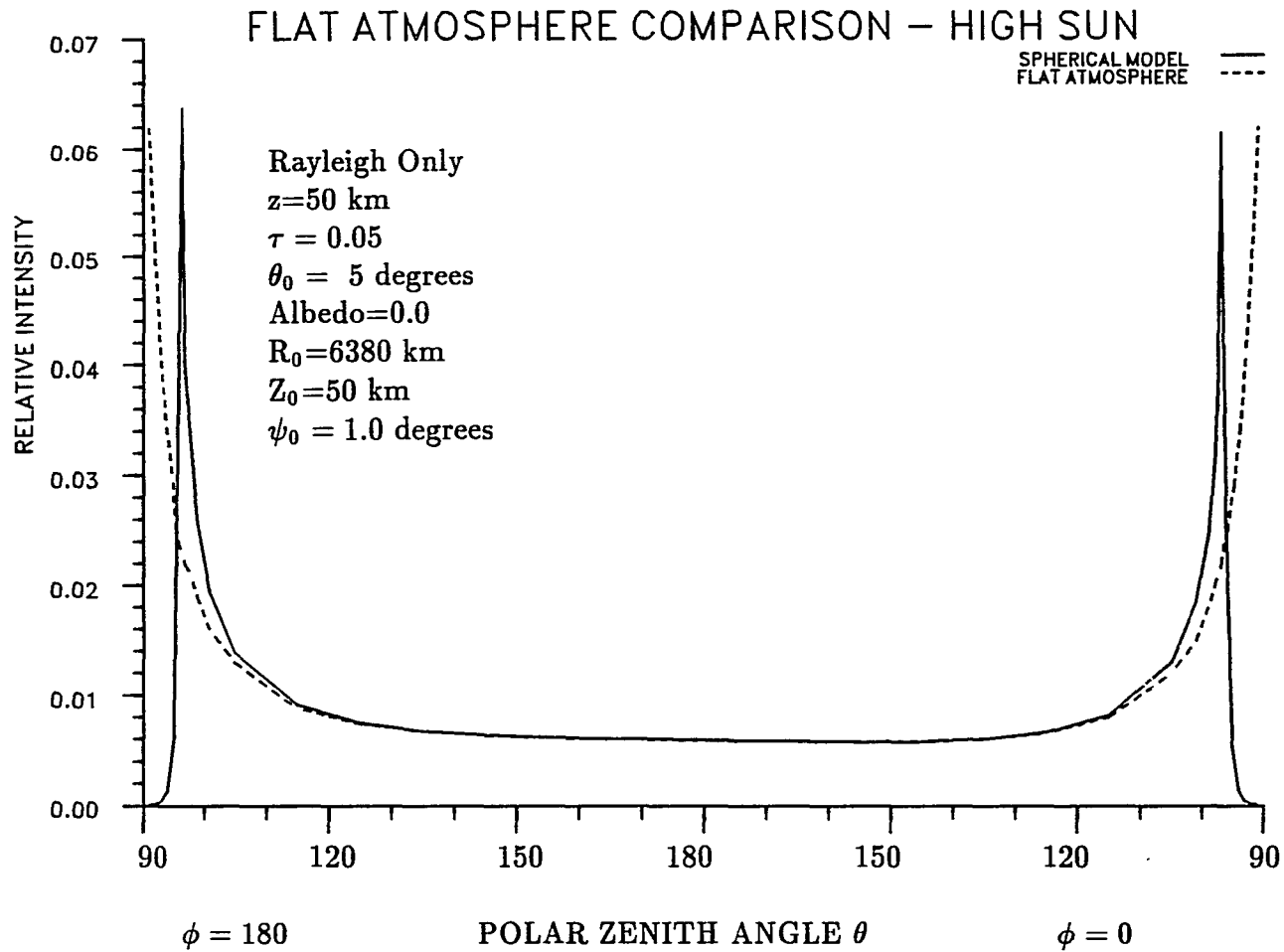


Figure 4.3 Reflected intensities at the top of the atmosphere for the case of a high sun and small optical depth. Comparison with flat atmosphere results for $\phi=0$ and 180 degrees.

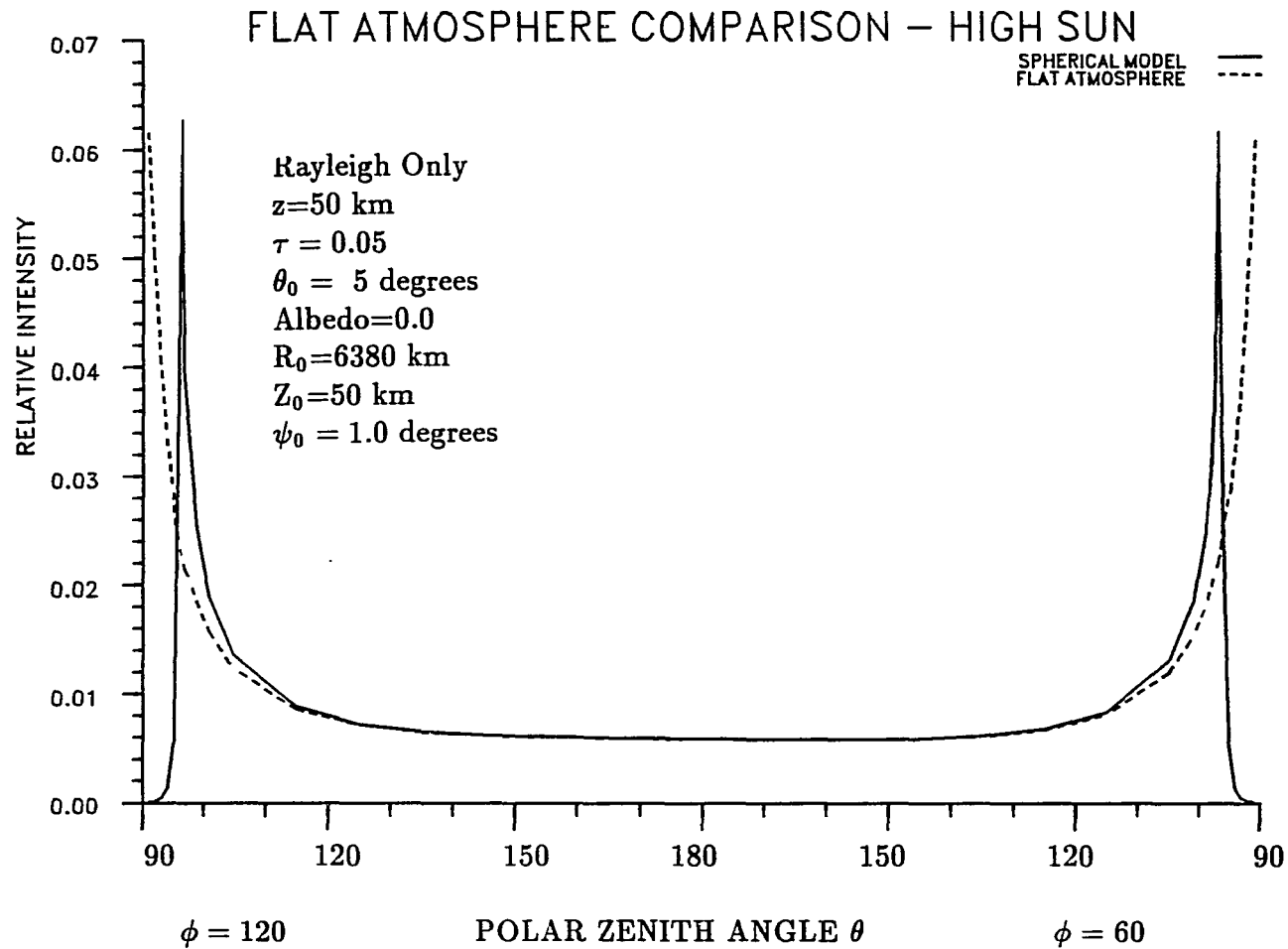


Figure 4.4 Reflected intensities at the top of the atmosphere for the case of a high sun and small optical depth. Comparison with flat atmosphere results for $\phi=60$ and 120 degrees.

is a very simple quantity to check. One simply computes the net flux at the top and bottom of the atmosphere and ensure that they cancel. One need not worry about the horizontal fluxes because horizontal homogeneity ensures that the divergence of these fluxes will always vanish. In the spherical case the lack of horizontal homogeneity complicates the problem and the horizontal fluxes must be computed and accounted for in the flux divergence computations.

Model output from a Rayleigh only atmosphere of optical depth 0.40, solar zenith angle of 85 degrees, and twenty levels was used to check energy conservation. Since ten of the levels must be used to account for the spherical nature of the problem, leaving the other ten levels to divide the nearly 0.40 optical depth, this provides a severe check of the model because the layer optical depths are near the limit of acceptability. To check for energy conservation, a program developed at the University of Arizona was used. This program considers each layer to be a plane cylinder with the cone boundary acting as the side of the cylinder. Using the z-axis solution to be representative of the intensities at that level on the top or bottom of the given cylinder, and averaging the cone intensities from the two levels to obtain layer intensities on the sides, net fluxes are computed for each layer. The results from these calculations indicate that flux is conserved to better than 3%. In view of the approximations in calculating the flux divergence and the high values for the layer optical depth, this strongly suggests that no programming errors are present.

4.4 Cone to Zenith Comparison

The cone to zenith comparison is designed to examine the accuracy of the cone boundary solution that is used in solving the zenith intensities. As with most

models that use approximated boundary values, a technique may be developed that can solve the model such that the boundary of one problem is the solution in another. By making appropriate changes to the solar angle and the set of θ 's, the solution along the cone for one case can have the same geometric configuration as the zenith for a different problem. Then if the boundary were perfect these results would be identical.

As an example, consider a case where the solar angle on the z-axis is 85 degrees, $\theta=95$ degrees, and $\psi_0=1.0$ degrees. Further consider that the solution at $\eta=60$ degrees is to be checked. Then the solar angle, θ'_0 , on ψ_0 is given by

$$\cos\theta'_0 = \cos\theta_0\cos\psi_0 + \sin\theta_0\sin\psi_0\cos\eta \quad (4.1)$$

and in this case $\theta'_0=84.50$ degrees. The above formula may also be applied to the line of sight as well. Then

$$\cos\theta' = \cos\theta\cos\psi_0 + \sin\theta\sin\psi_0\cos(\eta - \phi) \quad (4.2)$$

where it should be noticed that the azimuth of the viewing angle has been included. Then for the twelve ϕ angles(all angles from 0 to 360 degrees must be used because of the lack of symmetry) there would be twelve θ' angles for the comparison run. Because this would lead to a prohibitive time problem, the comparisons were restricted to cases where $\eta = \phi$ and in the above problem, $\theta'=94.0$ degrees. The intensity values that would be compared would be denoted by $I(z, \theta = 95, \phi = 60, \theta_0 = 85, \psi = \psi_0, \eta = 60)$ and $I(z, \theta = 94, \phi = 60, \theta_0 = 84.5, \psi = 0)$.

The parameters used in the actual comparison runs were $\theta_0=85$ degrees, a pure Rayleigh atmosphere of optical depth 0.40, surface albedo of 0.8, $\psi_0=1.0$

degrees, $R_0=6380$ km, and Z_0 of 50 km. The boundary solutions for this solar zenith angle were obtained at each of the seven η 's from 0 to 180 degrees at thirty degree intervals. The model was then run using these η radial lines as a z-axis. The adjusted solar angles used were 84, 84.13, 84.50, 85.00, 85.50, 85.87, and 86 degrees, corresponding to η 's of 0, 30, 60, 90, 120, 150, and 180 degrees respectively. Only the solutions for $\phi=\eta$ were considered, then the set of θ angles used for the original run were decreased by one degree as given by (4.2). The results of this comparison for $\eta = \phi = 0$ and 180 degrees are shown in Figs. 4.5 and 4.6, while those for $\eta = \phi = 60$ and 150 degrees are shown Figs. 4.7 and 4.8. In these plots, the phrase "zenith solution" refers to the z-axis solution for the adjusted solar angle cases, while "cone solution" refers to the boundary solution of the original $\theta_0=85$ case. The agreement in all cases is quite good, with the largest percentage difference being 12% for the reflected intensities between 90 and 100 degrees. Considering that this case was for a low sun, and that the largest layer optical depths were on the order of the 0.035 limit, the results indicate that the solutions on the boundary are good approximations. Referring to the discussion of Section 4.1, it can be concluded that the errors in the boundary do not introduce errors in the final solution greater than 1%.

4.5 Comparison with other Methods

The most important test of a new model is how well it agrees with other models. In this section results from three other models are presented. Two of these used Monte Carlo techniques, and the third is the quasi-spherical approach of Asous(1982).

In the comparison with Asous(1982) the model parameters were: $\theta_0=85$

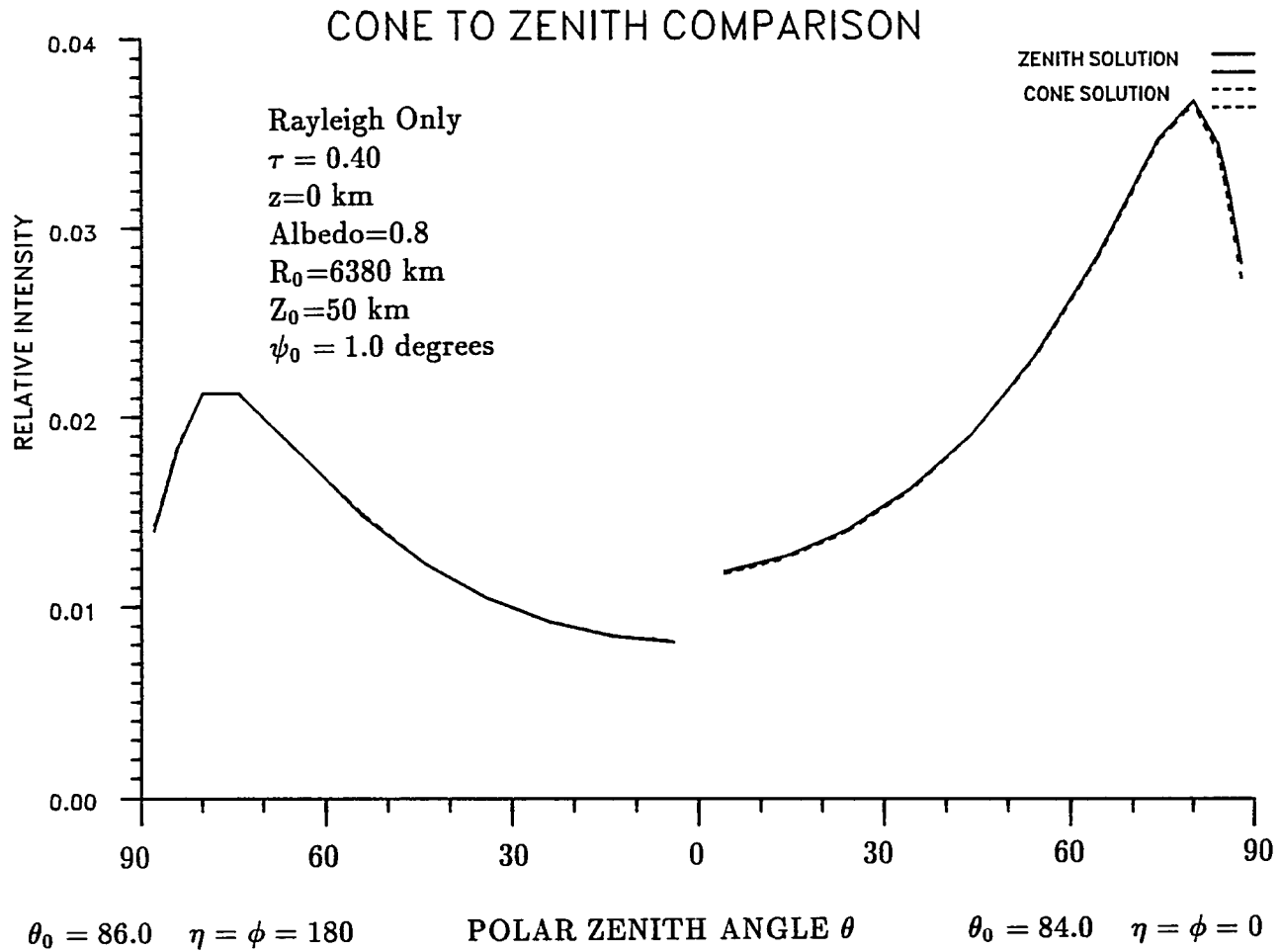


Figure 4.5 Transmitted intensities at the surface for $\eta = \phi = 0$ and 180 degrees. Shows the cone to zenith comparison.

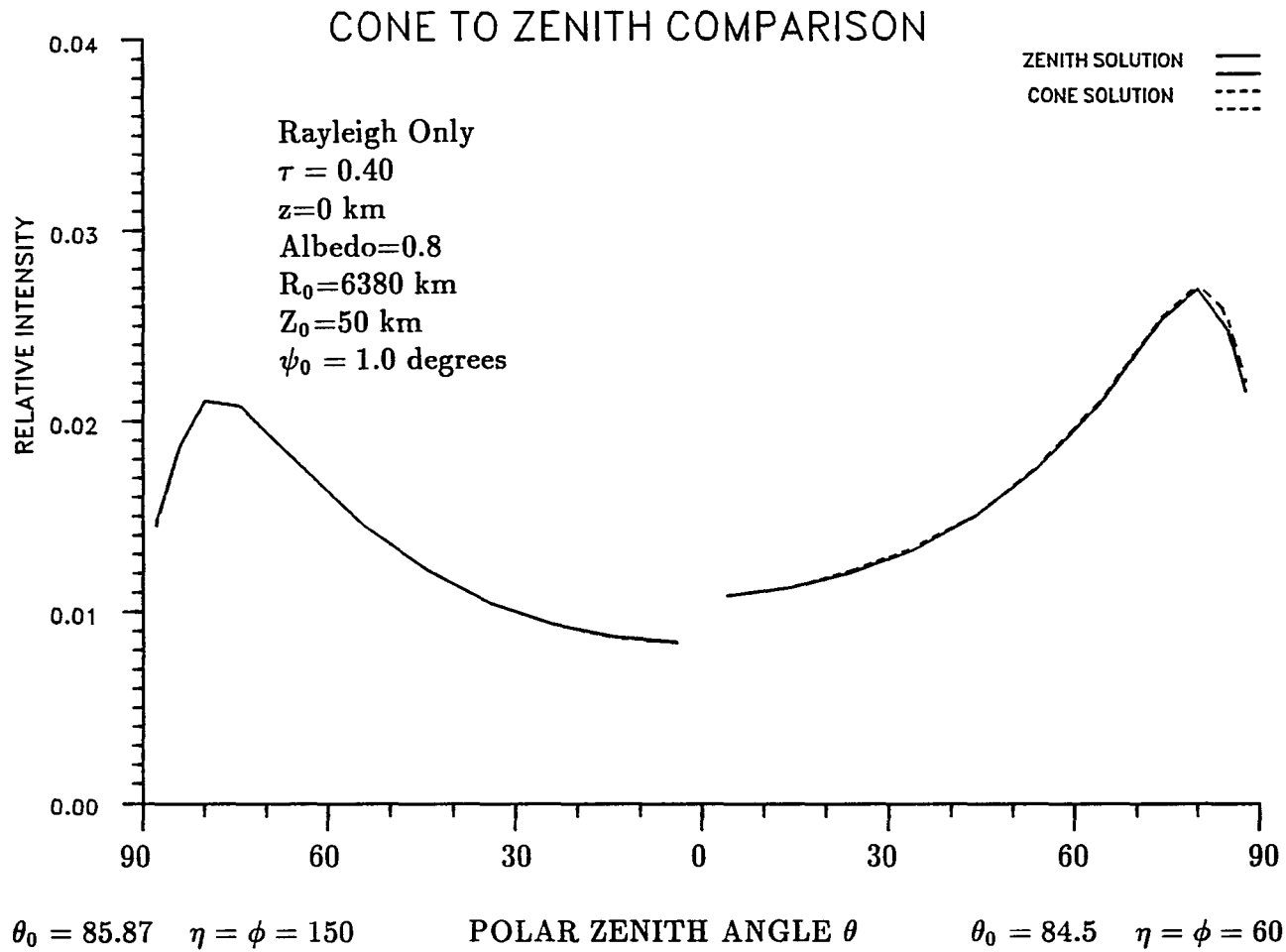


Figure 4.6 Transmitted intensities at the surface for $\eta = \phi = 60$ and 150 degrees. Shows the cone to zenith comparison.

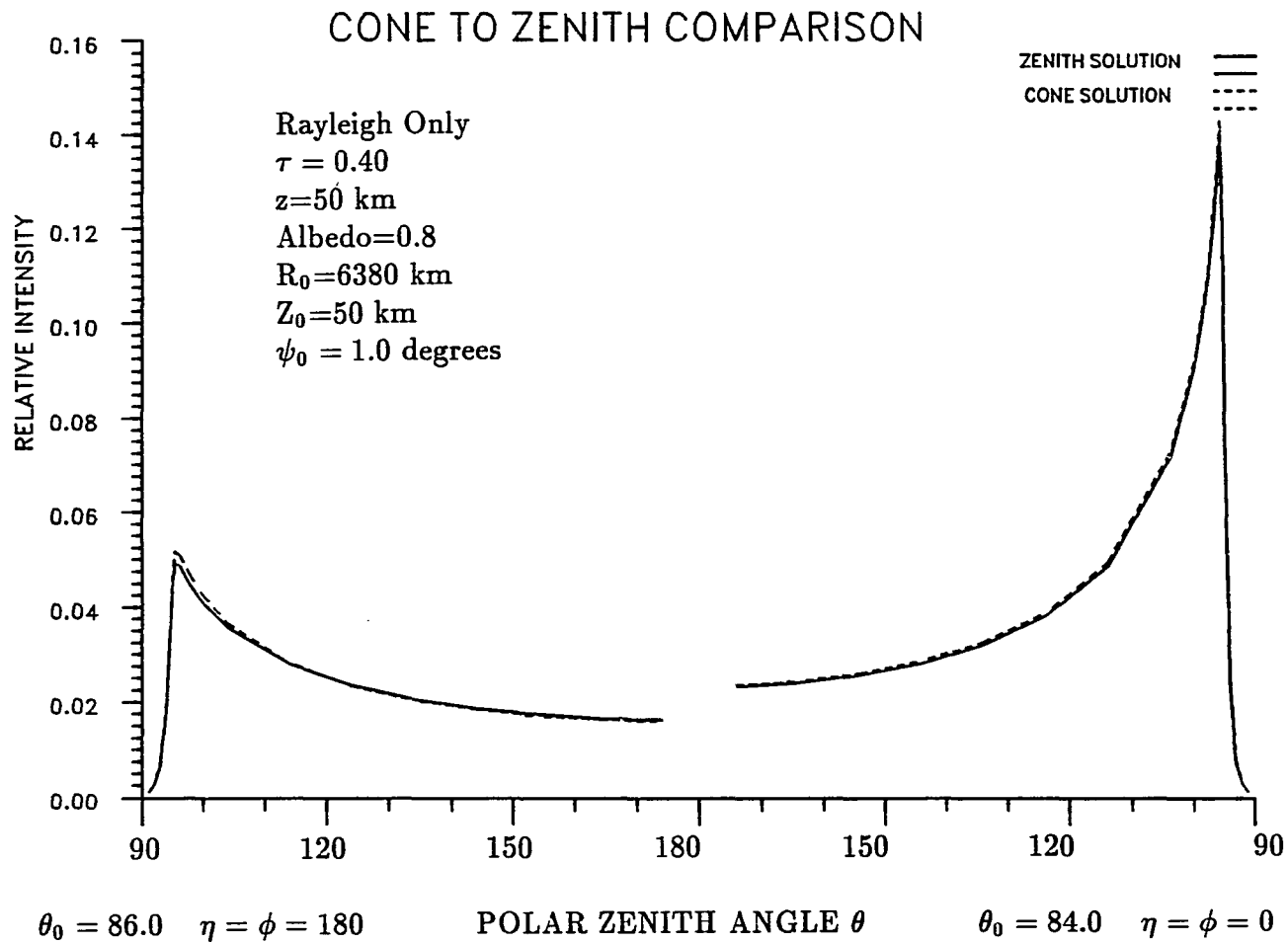


Figure 4.7 Reflected intensities at the top of the atmosphere for $\eta = \phi = 0$ and 180 degrees. Shows the cone to zenith comparison.

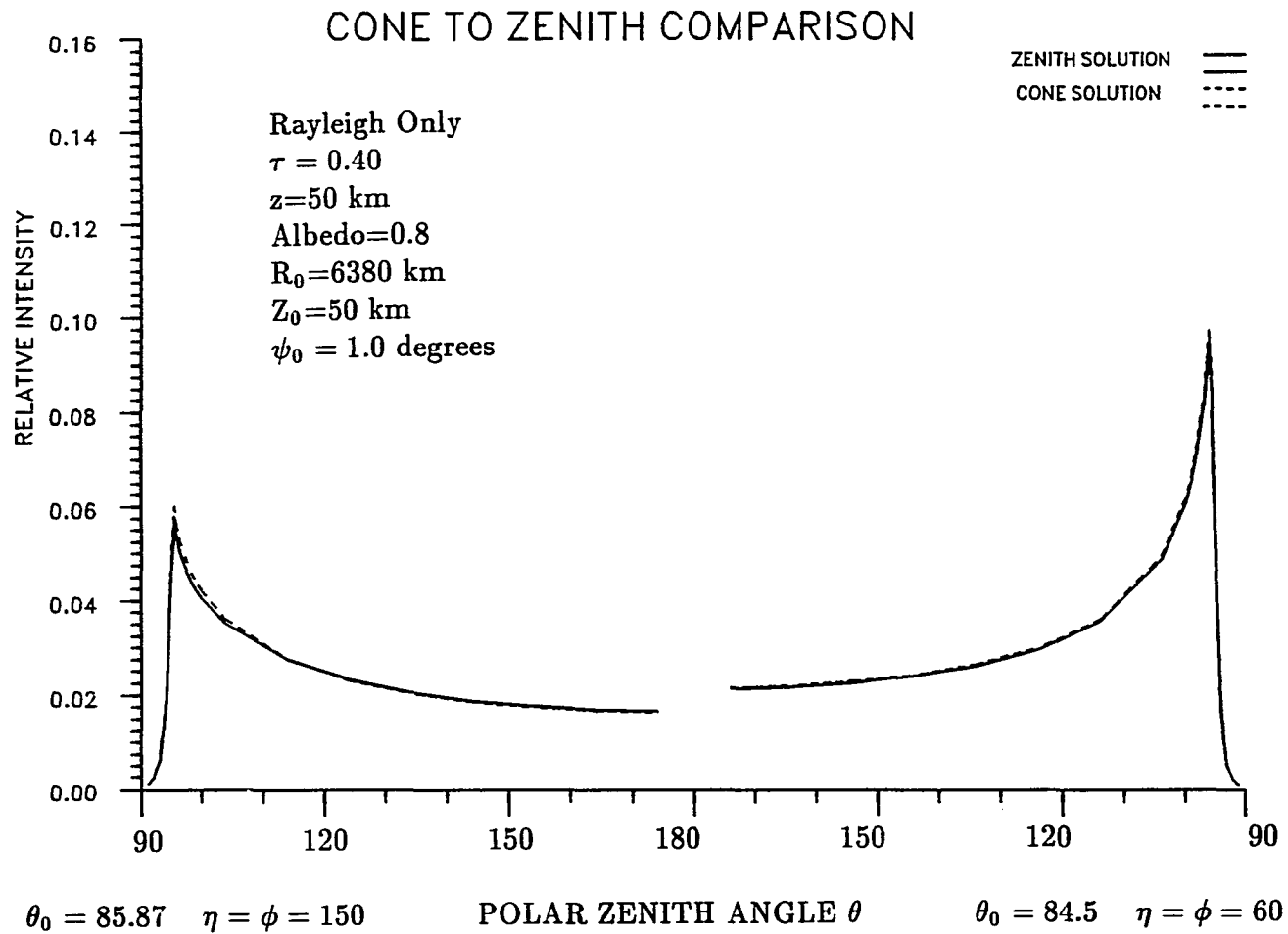


Figure 4.8 Reflected intensities at the top of the atmosphere for $\eta = \phi = 60$ and 150 degrees. Shows the cone to zenith comparison.

degrees, a pure Rayleigh atmosphere with $\tau_r=0.10$, albedo of 0.0, $R_0=6370$ km, and $Z_0=50$ km. The results for $\phi=0$ and 180 degrees are shown in Figs. 4.9 and 4.10 while Figs. 4.11 and 4.12 show $\phi=60$ and 120 degrees. Figs. 4.9 and 4.11 indicate excellent agreement in the results of the transmitted intensities at the surface. For $\theta < 80$ degrees, the differences between the two models are less than 1.0%, and 1 to 2% for $\theta > 80$ degrees. The reflected intensities at the top of the atmosphere (Figs. 4.10 and 4.12) agree well also. There do exist differences on the order of 10% for $\theta < 93.5$. These errors are not critical. One, because the amount of energy at these angles is not large, and two, because at these angles the assumptions of the quasi-spherical approach are expected to break down. These angles are also highly influenced by the selection of the vertical height distribution of molecules. Since the exact model used by Asous was not available, differences are sure to exist.

Both of the next two models used for comparison utilize Monte Carlo techniques. The first of these is the model presented in Marchuk(1980). The parameters used were identical to Asous with $\theta_0=53.13$ degrees and Z_0 of 100 km. An albedo of 0.25 as well as 0.0 was used. According to Marchuk(1980), his results are certain to the 2-3% limit. Further differences of up to 4% can be expected from the inclusion of polarization in the Marchuk model but not the current method (Marchuk(1980) and Mikhailov and Nazaraliev(1971)). The results are presented in Figs. 4.13 to 4.16, with the reflected intensities shown in Figs. 4.15 and 4.16. The transmitted intensities, presented in Figs. 4.13 and 4.14, agreed to well within the uncertainties presented earlier. The reflected values differ greatly for angles less than 110 degrees. Normally, a discrepancy of this nature would be cause for concern, but there are several points that

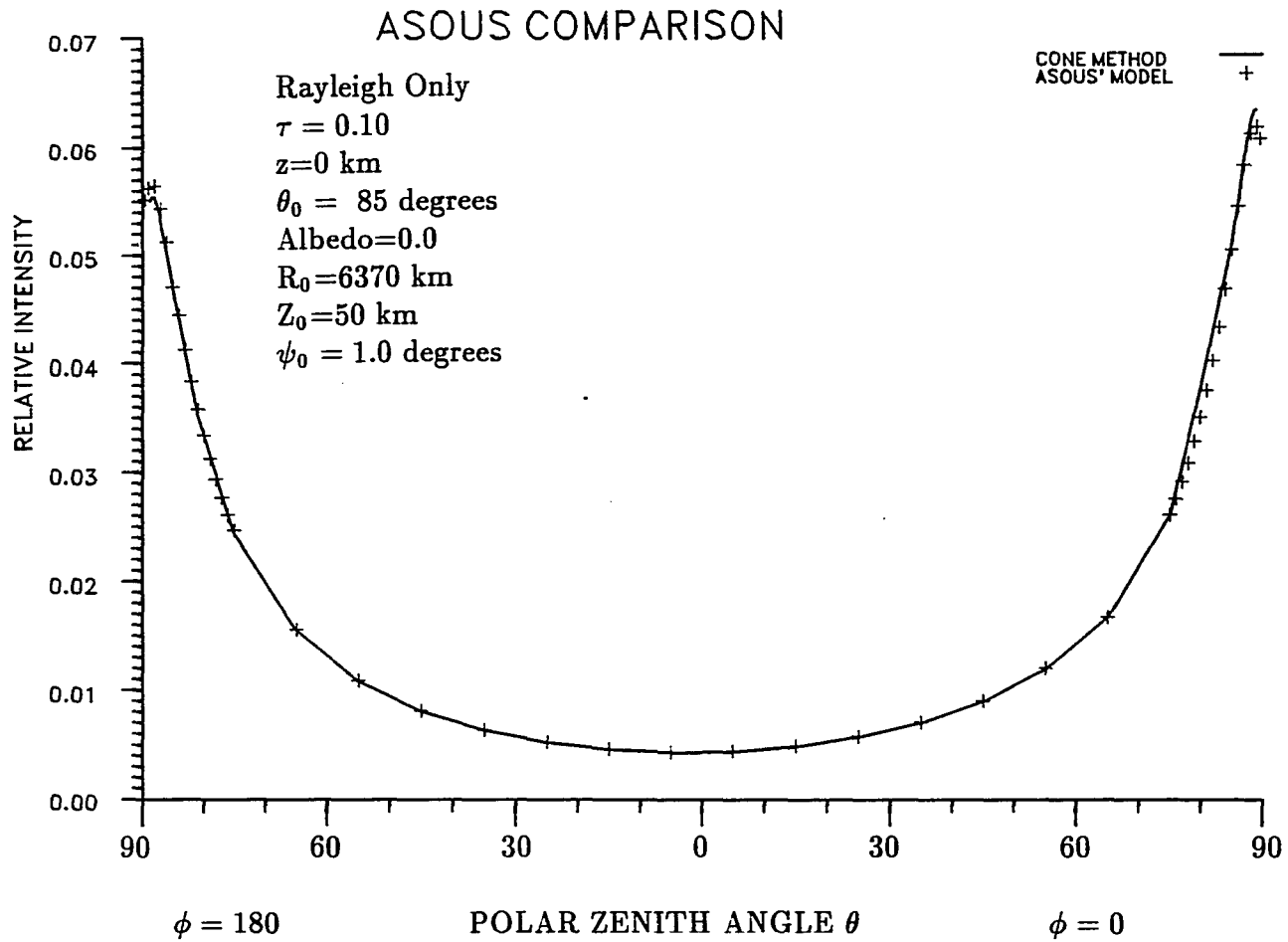


Figure 4.9 Transmitted intensities at the surface for $\phi=0$ and 180 degrees. Results are from Asous(1982) and the current method.

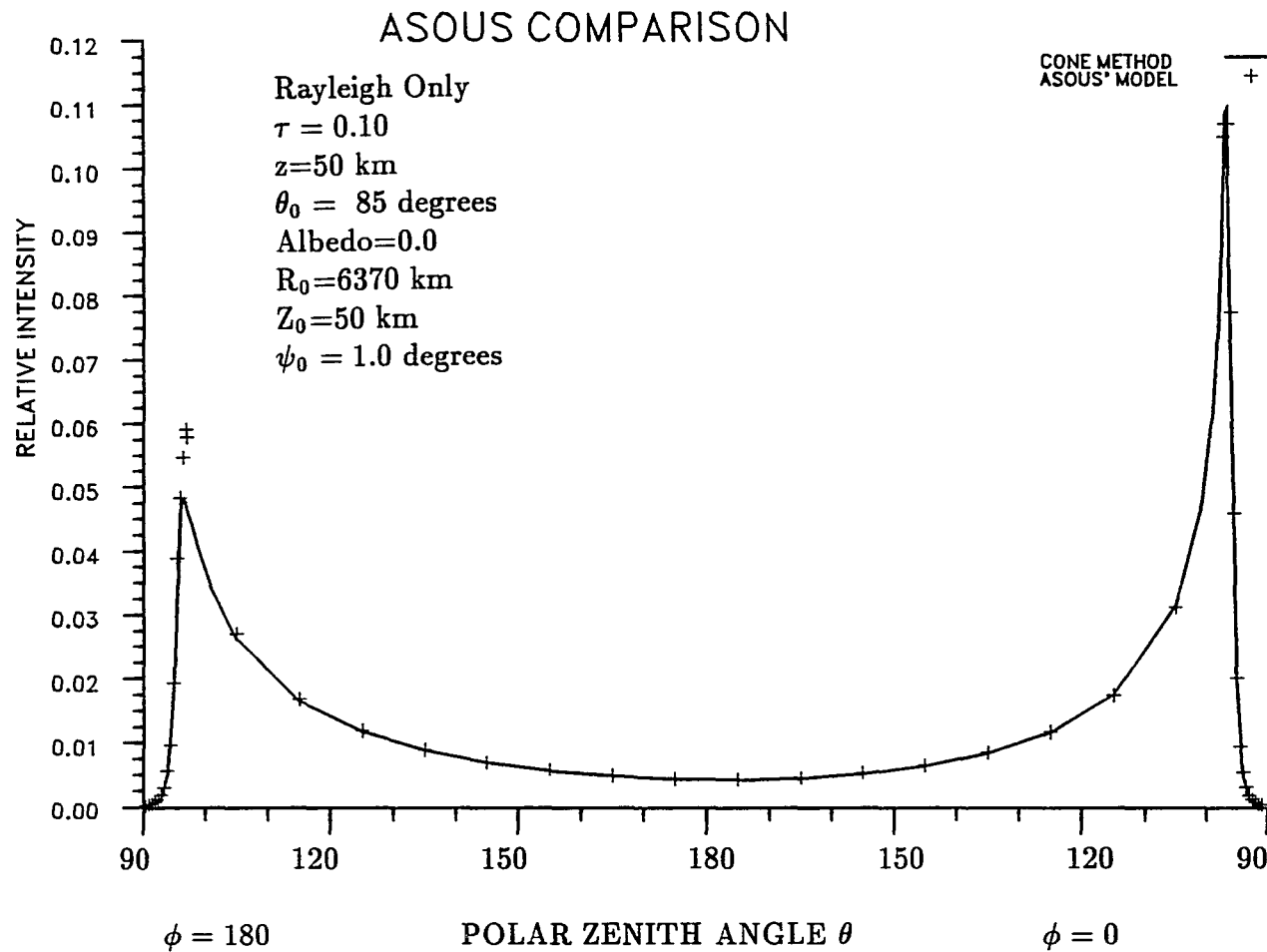


Figure 4.10 Reflected intensities at the top of the atmosphere for $\phi=0$ and 180 degrees. Results are from Asous(1982) and the current method.

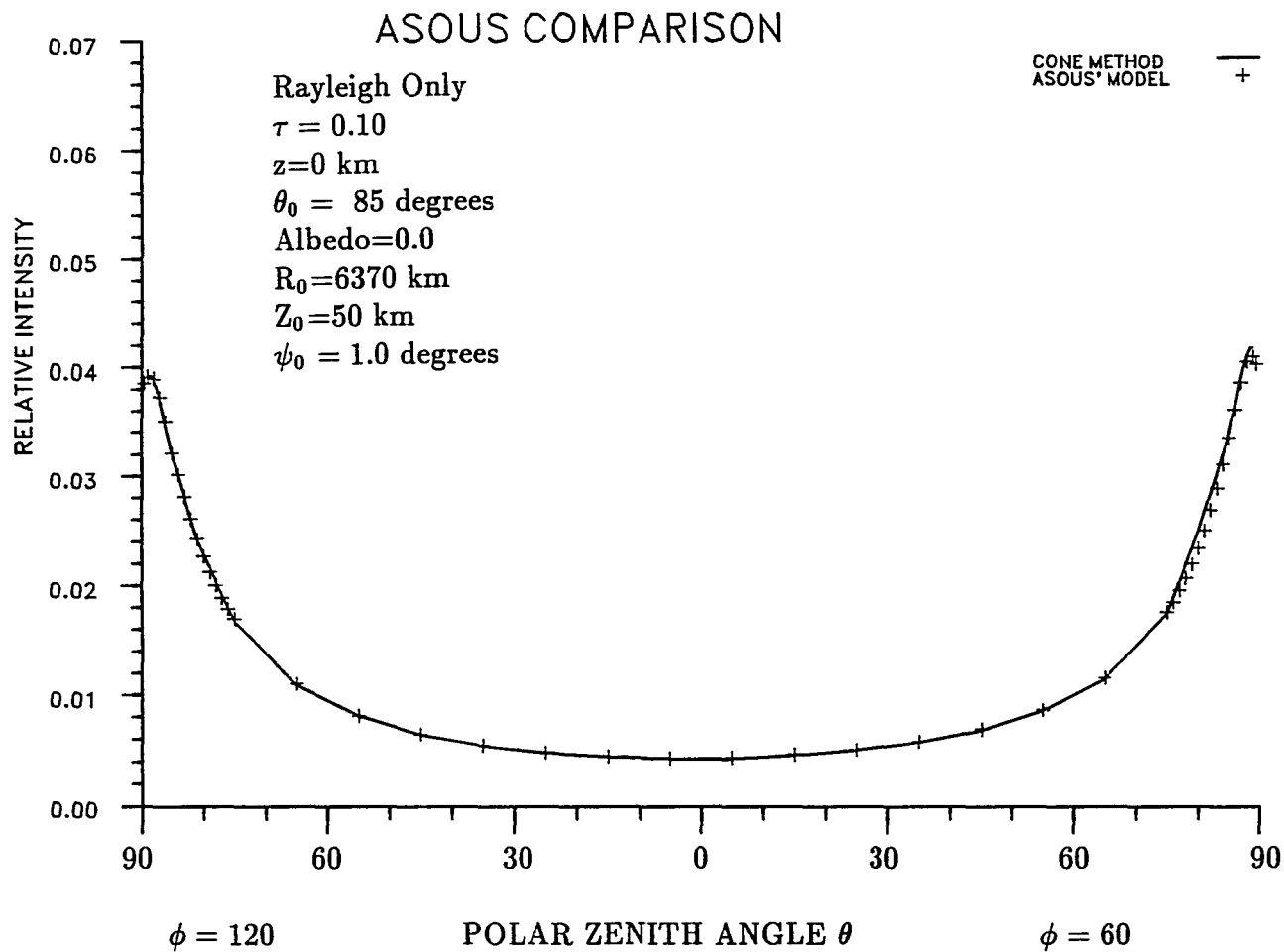


Figure 4.11 Transmitted intensities at the surface for $\phi=60$ and 120 degrees. Results are from Asous(1982) and the current method.

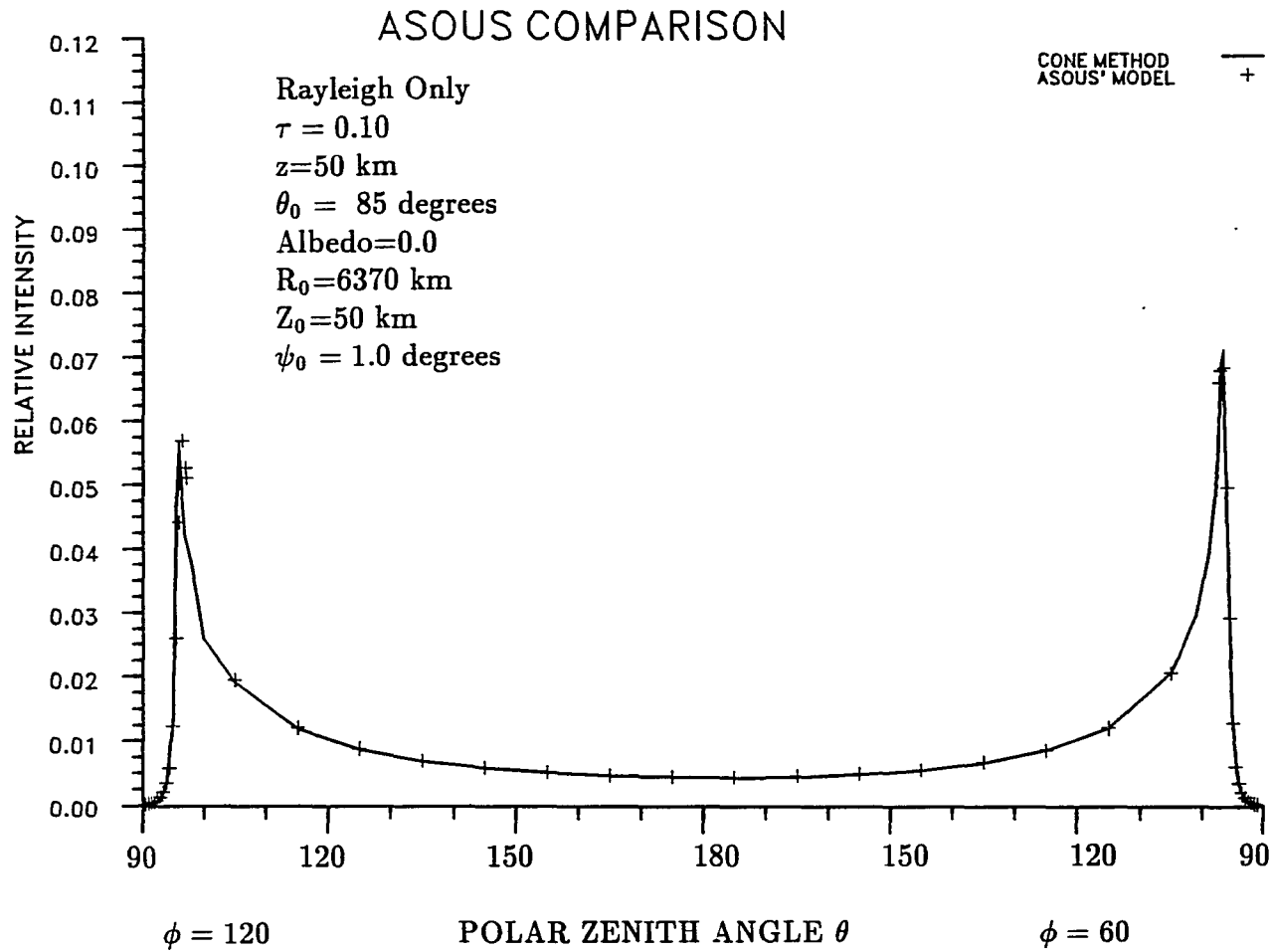


Figure 4.12 Reflected intensities at the top of the atmosphere for $\phi=60$ and 120 degrees. Results are from Asous(1982) and the current method.

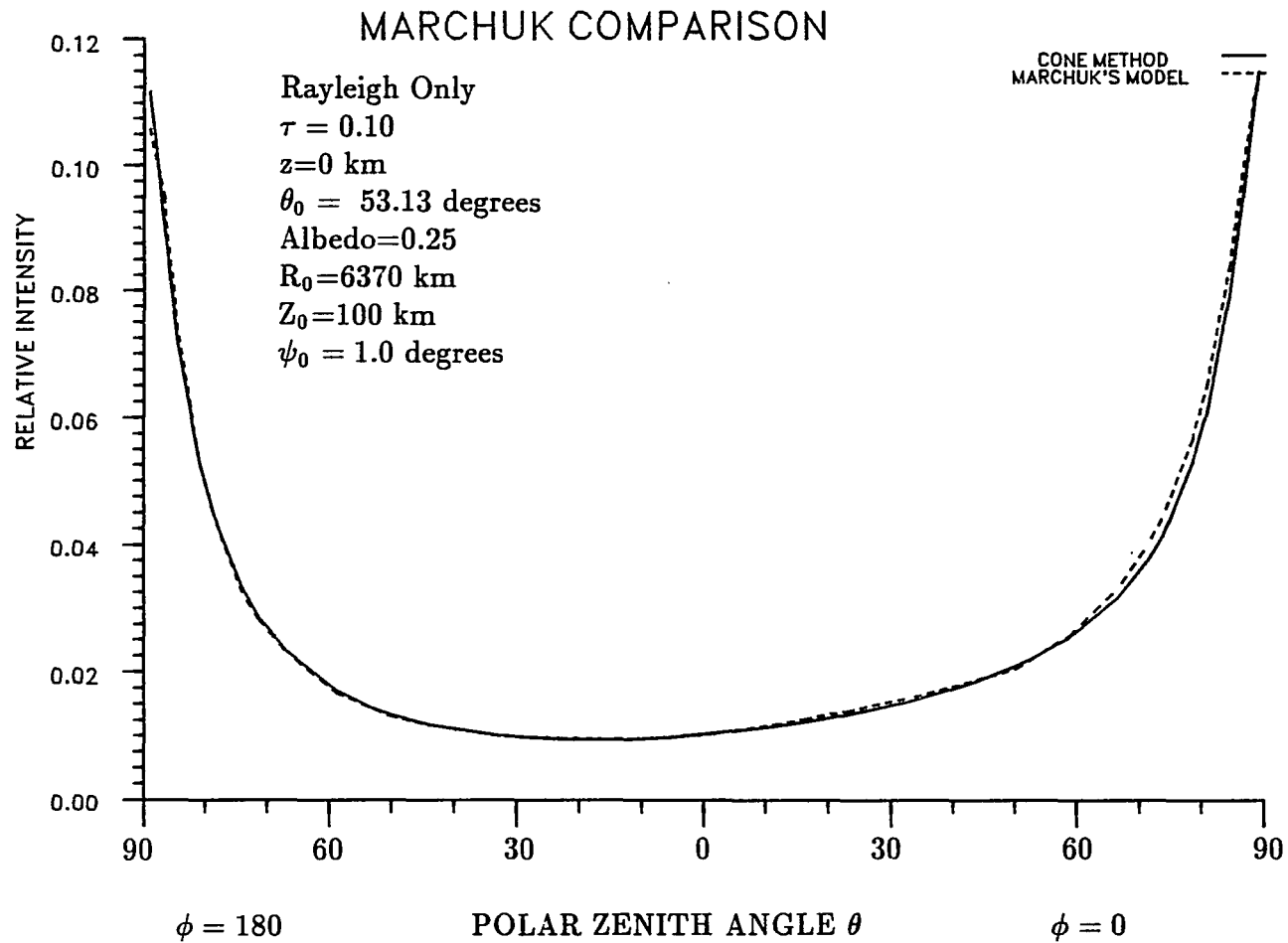


Figure 4.14 Transmitted intensities at the surface for $\phi=0$ and 180 degrees and albedo of 0.25. Results are from Marchuk *et al.*(1980) and the current method.

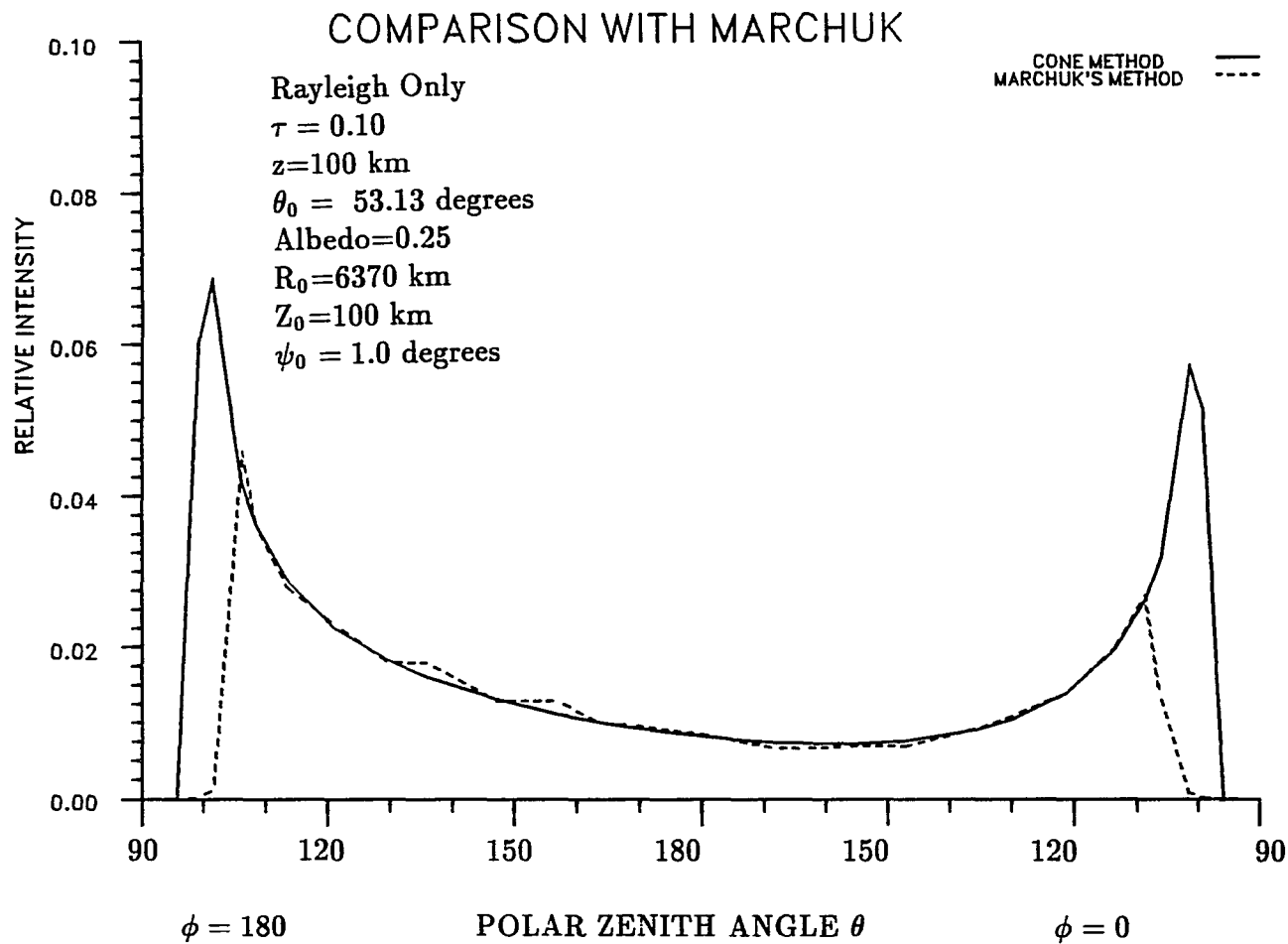


Figure 4.15 Reflected intensities at the top of the atmosphere for $\phi=0$ and 180 degrees and albedo of 0.0. Results are from Marchuk *et al.*(1980) and the current method.

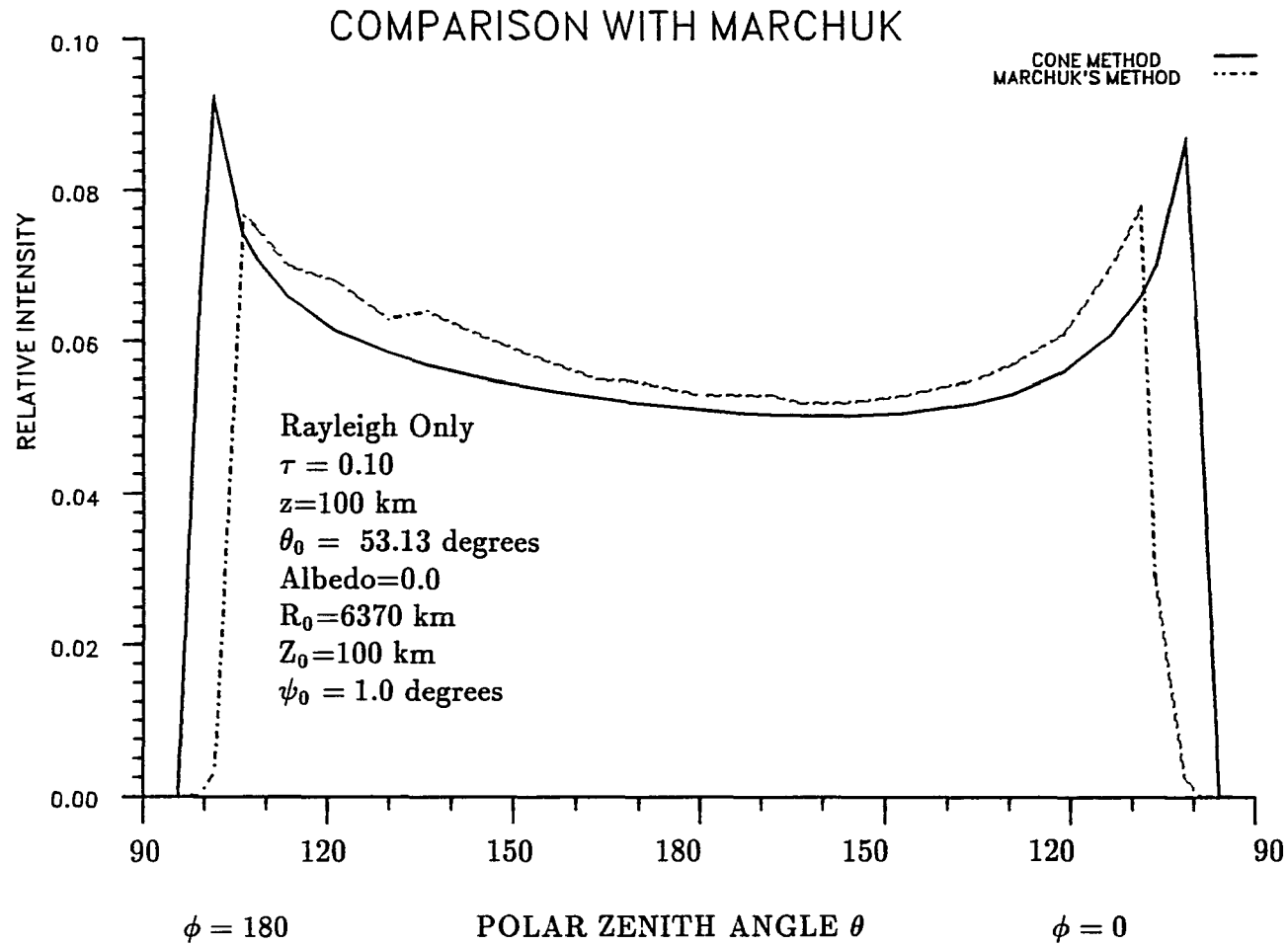


Figure 4.16 Reflected intensities at the top of the atmosphere for $\phi=0$ and 180 degrees and albedo of 0.25. Results are from Marchuk *et al.*(1980) and the current method.

reduce the credibility of Marchuk's results. From path length arguments, it is clear that there is a problem with the Marchuk results. Referring to Fig. 4.16 where the albedo is 0.25, there should be a sharp increase in intensity at $\theta=100.1$ degrees, the point at which the paths first strike the ground. The current method shows this jump quite well, while the Marchuk results do not peak for another 8 degrees. Further research indicated that the results for the transmitted case were first presented by Antyufeyev and Nazaraliev(1973). This paper did not present results for the reflected cases, thus it is possible that the reflected intensity results were computed at a later time with slightly different parameters, or that problems were recognized and the reflected results withheld from the original paper.

The final comparison is made with Adams(1978). Adams used his Monte Carlo technique on a vertically homogeneous Rayleigh atmosphere of optical depths 0.25 and 1.00. The solar angle was 84.26 degrees, albedo of 0.0, $R_0=6371$ km, and $Z_0=100.0$ km. The results given by Adams were single scatter intensities and percentage of single to total scatter. From these, a total scatter was inferred, and these are the values plotted in Figs. 4.17 and 4.18. These figures indicate excellent agreement between the two methods at all angles, except 95 degrees for $\tau=0.25$ and $\phi=0$. In this case the solutions differ by 6%. Because of the statistical nature of the Monte Carlo method, and the better than 2% agreement at all other points, this is not considered to invalidate the current method.

Considering the results of this and the previous sections, the current work accurately describes radiative transfer in a spherical atmosphere to better than 3% in total intensity. This estimate is on the high side for safety, and it is felt that in most situations the model is accurate to better than 1%. The advantage this model has over other techniques is the combination of speed and accuracy. It is

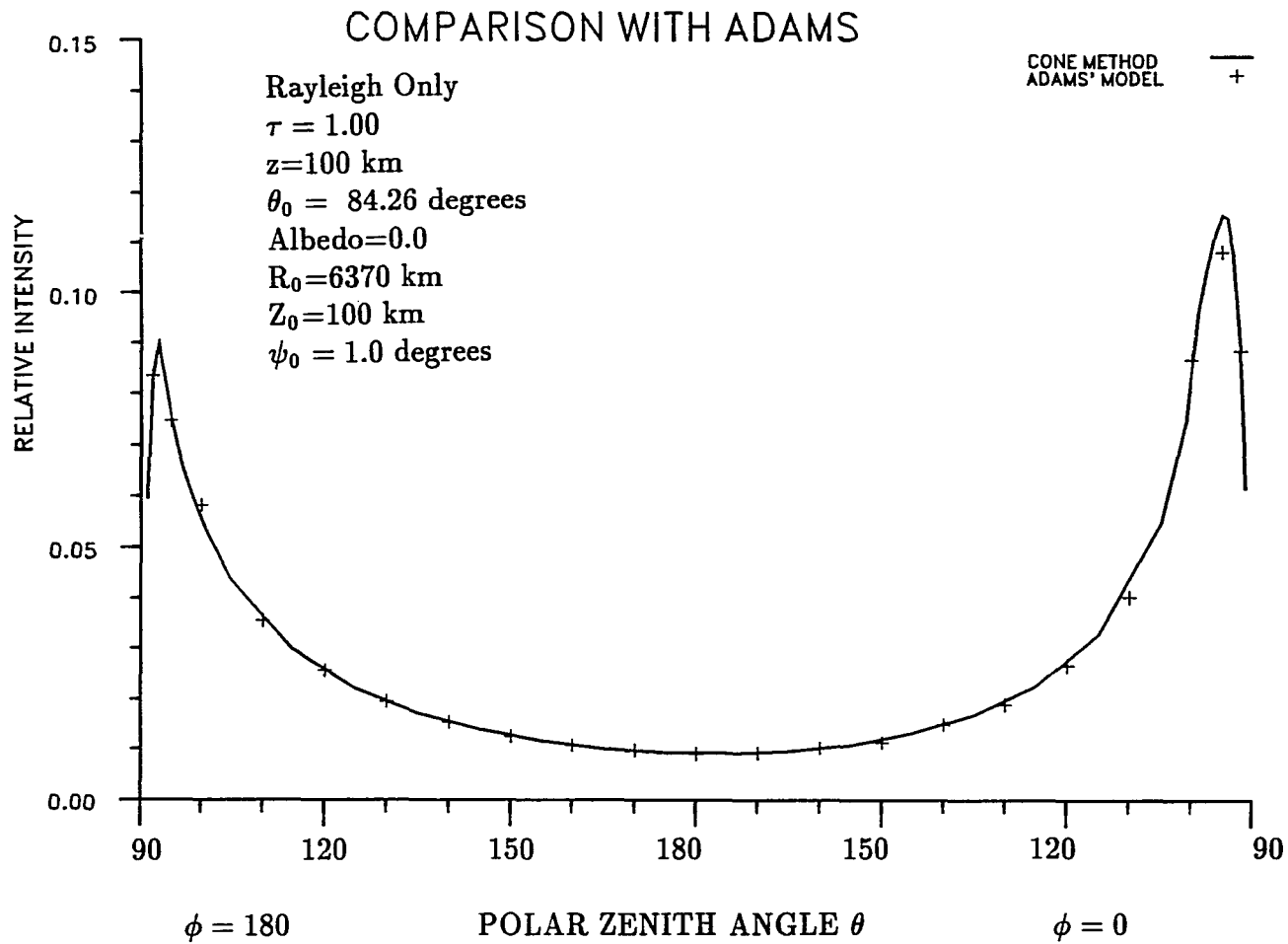


Figure 4.17 Reflected intensities at the top of the atmosphere for $\phi=0$ and 180 degrees for a homogeneous Rayleigh atmosphere of optical depth 0.25. Results are from Adams and Kattawar(1978) and the current method.

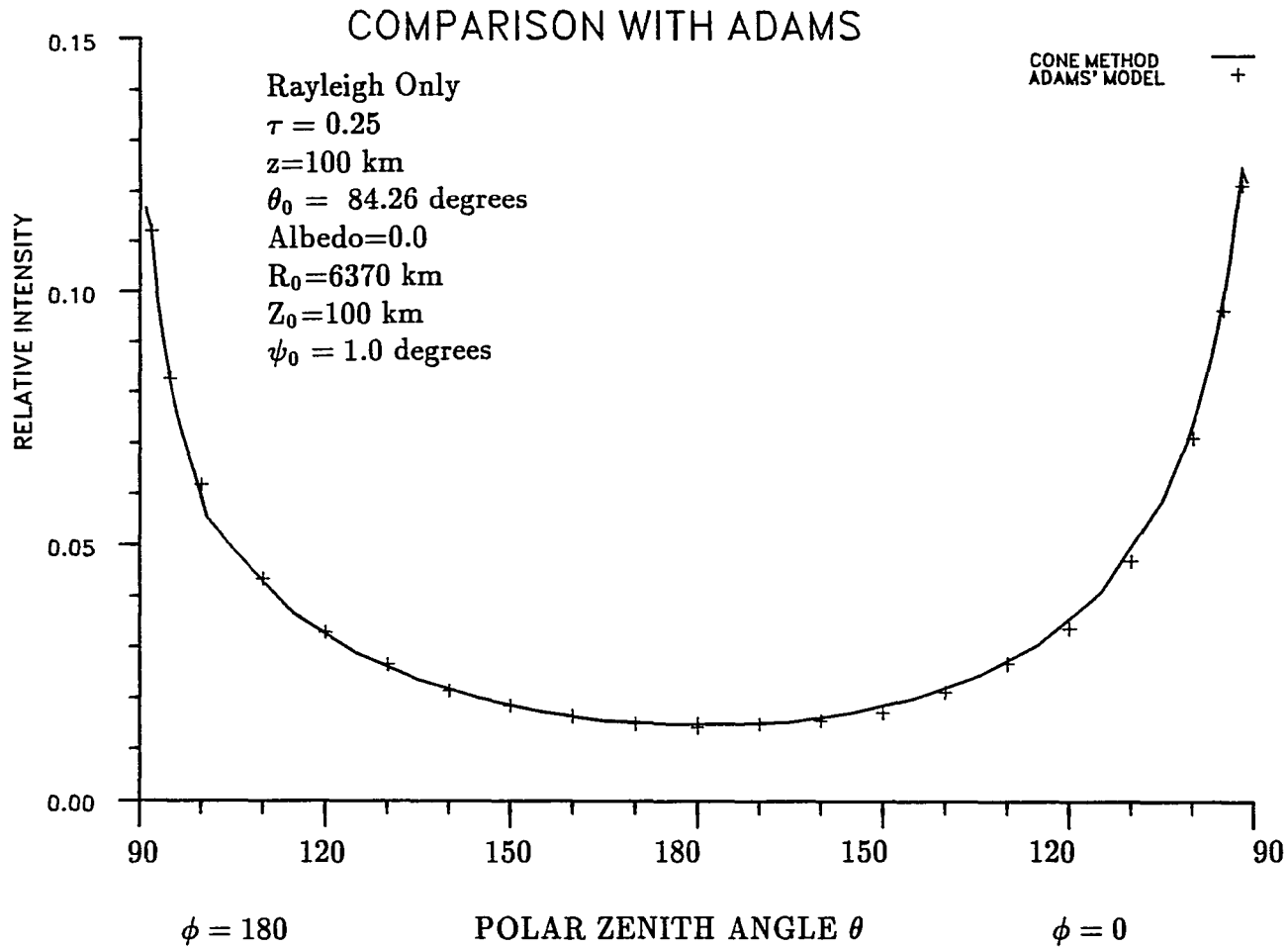


Figure 4.18 Reflected intensities at the top of the atmosphere for $\phi=0$ and 180 degrees for a homogeneous Rayleigh atmosphere of optical depth 1.00. Results are from Adams and Kattawar(1978) and the current method.

as accurate as the Monte Carlo simulations but more computationally efficient, and does not suffer from the statistical fluctuations of these techniques. It is also felt that the current technique is more accurate and versatile than other techniques mentioned in Chapter I that rely on moments of intensity and other approximations to enhance computational efficiency. It is this versatility in angular and height coordinates that makes the current model applicable for most earth atmosphere cases. Furthermore the model may be employed for sub-horizon sun situations(twilight) with essentially no increase in computer time, although accuracy may suffer slightly. This is a topic for future research.

CHAPTER V

APPLICATION TO LIMB SCAN

In this chapter, the current model is used to simulate atmospheric limb scans from space. In a limb scan, a satellite scans the atmosphere vertically from top to bottom and measures the diffusely scattered radiation without looking at the ground. This is somewhat different from solar occultation measurements in which the satellite views the directly transmitted sunlight through the atmosphere. By applying Beer's law (first term of (2.4)) to these measurements and doing a direct inversion, the vertical distribution of atmospheric constituents is inferred (Chu and McCormick (1979)). The problem with occultation measurements is the satellite is limited to one sunrise/sunset event per orbit. At other times, the instrument is idle. To better utilize the instrument, limb scan measurements of the diffusely scattered sunlight could be made. The modelling of these measurements requires calculations of atmospheric scattering including spherical geometry. In this chapter, the current model is used to simulate such limb scans in order to examine whether information about atmospheric constituents may be retrieved from them. As an in depth treatment of actual retrieval techniques is beyond the scope of this dissertation, the discussion is limited to examining the model results and commenting on the feasibility of attempting atmospheric content determinations based upon the information contained in the scans.

Model runs were performed using five basic atmospheric models. These are presented in Figs. 5.1 and 5.2. In all cases the height of the atmosphere is taken to be 50 km. Model I is a Rayleigh atmosphere of 0.06 optical depth

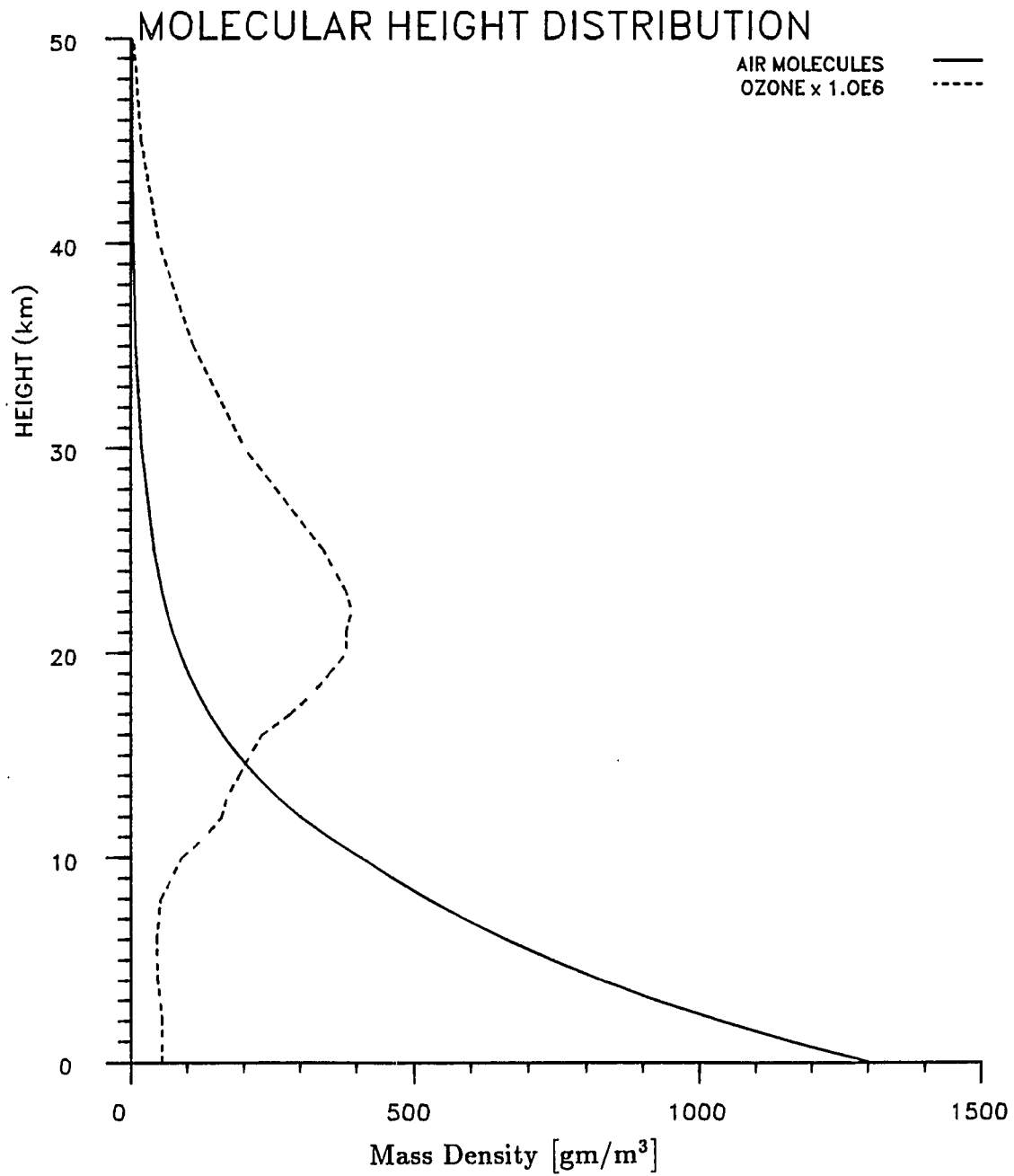


Figure 5.1 Height distribution of air molecules for Model I, and distribution of ozone molecules($\times 10^6$) for Model II in terms of mass density.

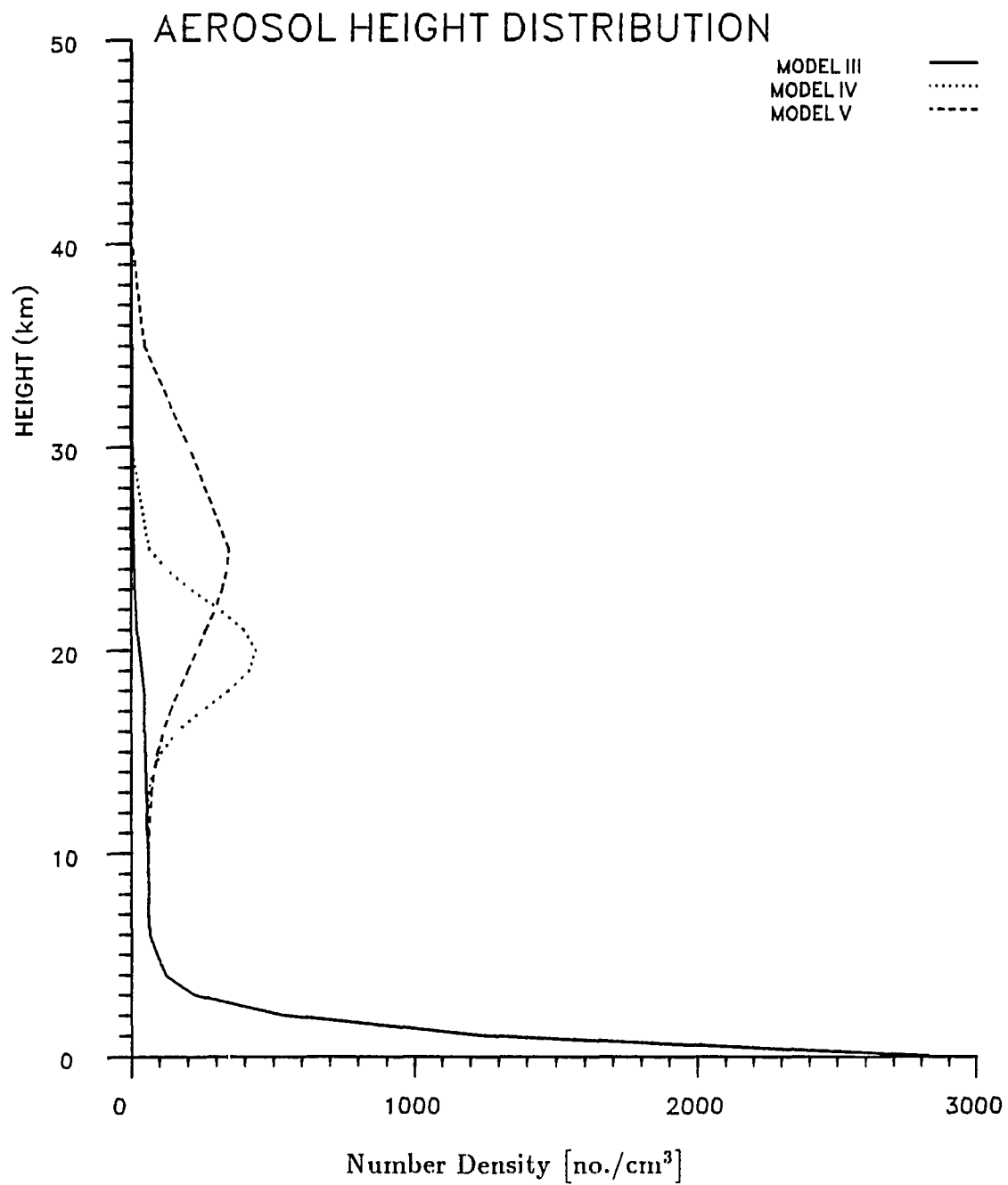


Figure 5.2 Height distribution of aerosols for Models III, IV, and V.

corresponding to a wavelength of 0.6 microns. This Rayleigh model is used in all runs. Model II, shown in Fig. 5.1, includes, in addition to the Rayleigh model, an ozone distribution peaked at about 22 km, corresponding to an ozone absorption optical depth of 0.04 due to Chappuis band absorption. In the runs examined, the ozone optical depth was varied and given values of 0.00, 0.02, 0.04, and 0.08. These other optical depths essentially move the distribution of Fig. 5.1 to the left or right. Model III introduces tropospheric aerosols with an aerosol optical depth of 0.24. This model was run for ozone optical depths of 0.00, 0.02, and 0.04. The last two models introduce stratospheric aerosol layers of optical depth 0.103. These aerosol layers are superimposed on the aerosol height distribution of Model III. Model IV is peaked at 20 km and the layer is contained between 15 and 25 km (Fig. 5.2). As seen in Fig. 5.2, Model V is peaked slightly higher at 25 km and is also broader, being contained between 15 and 30 km. Models IV and V were run for ozone optical depths of 0.00 and 0.04.

The geometry of the problem is shown in Fig. 5.3. The height of the satellite above the surface is 700 km, then $R_S = 7080$ km where $R_0 = 6380$ km. The satellite scans the atmosphere from the top to the surface. The lines of sight from a scan are discriminated by their tangent heights, h_T . The tangent height is the level above the surface at which the satellite line of sight becomes tangent in the atmosphere. In the current work 12 values of h_T were selected: 48.76, 43.22, 38.54, 35.23, 32.42, 29.32, 25.90, 22.16, 19.49, 15.19, 10.52, and 5.46 km corresponding to a given set of incident solar angles θ'_0 . If more lines of sight had been used, the computation time of a single scan would have increased, but since the atmosphere is divided into homogeneous shells, no new information would be obtained because some of the paths would become tangent in the same layer.

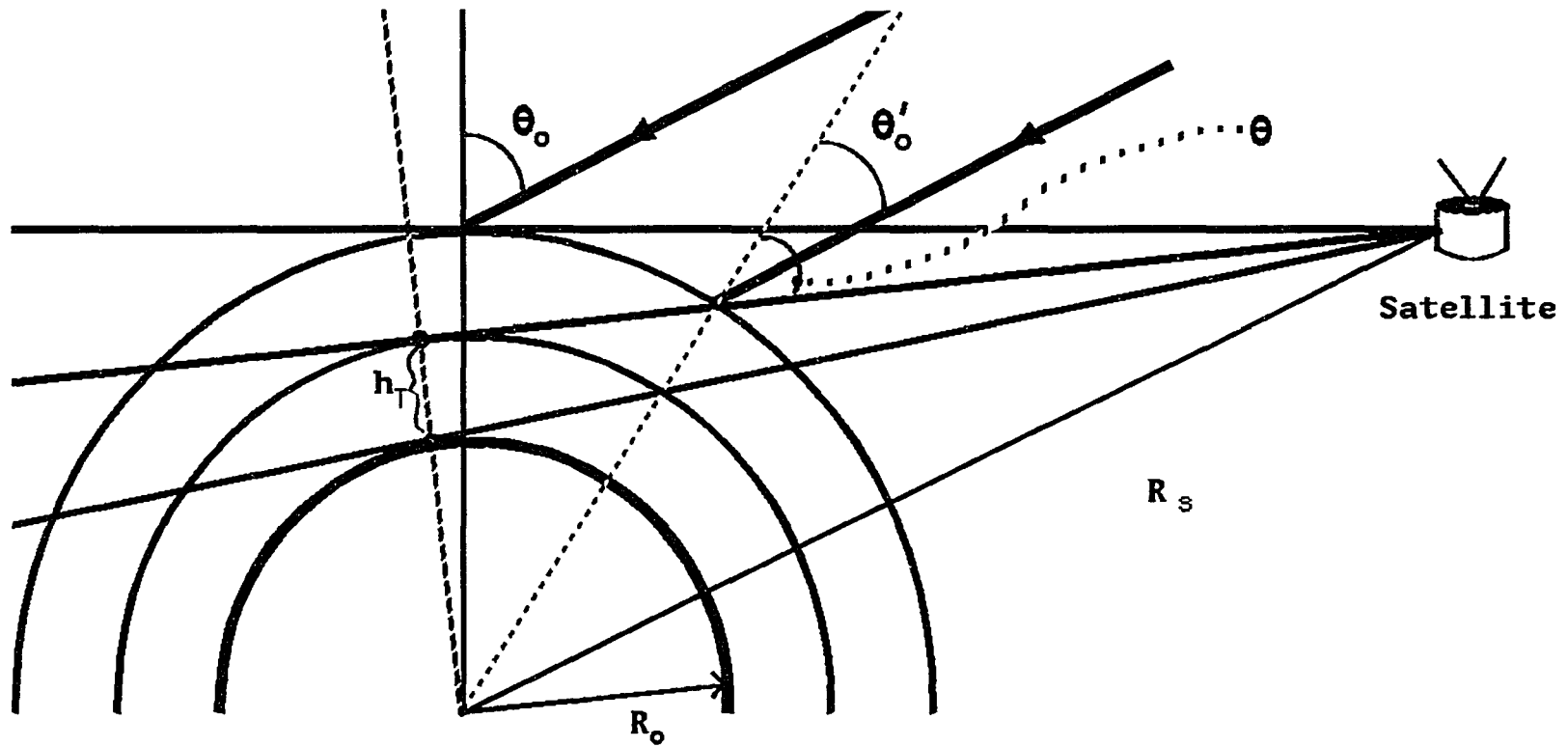


Figure 5.3 Satellite geometry and definition of terms used in the atmospheric limb simulations.

Since twelve lines of sight adequately cover the atmosphere, this number is an adequate tradeoff between time and height discrimination.

Selecting h_T , R_S , and θ_0 defines the point where the line of sight intersects the top of the atmosphere. Using trigonometry, θ'_0 and θ' (Fig. 5.3) are determined. These are the two parameters needed for the spherical model. For some runs $\phi = 180$ degrees, this corresponds to cases where the satellite is between the Earth and the Sun. When θ'_0 is calculated for the 12 lines of sight it is seen that $(\theta_0 - \theta'_0)$ varies from 1.1 to 5.9 degrees. Since this is a significant change, the model must be run for each θ'_0 and solved for the single θ' corresponding to the single beam which strikes the satellite for the given θ'_0 . To complete one satellite scan, the model must be run twelve times. Though inefficient, this process is not overly time consuming. At $\phi=90$ degrees this inefficiency is avoided. For example, using this azimuth and a sun angle of 25 degrees, $(\theta'_0 - \theta_0)$ varies from 0.02 to 0.64 degrees. At sun angle 85 degrees this is 0.001 to 0.03 degrees. This variation is small enough that a single average value for θ'_0 may be used. For $\theta_0 = 25$ degrees this amounts to an error of only 0.2% in the incoming solar flux. Thus an average solar elevation angle is used whenever possible in order to take advantage of the resulting large savings in computer time.

Differences between flat and spherical atmospheres were examined by running Models III, IV, and V for ozone optical depth 0.04 and $\theta_0 = 25$ degrees. The results are shown in Figs. 5.4 - 5.6 for $\phi = 90$ and 180 degrees. As can be seen from the figures, the flat atmosphere does not accurately portray the limb scan. This is not surprising since the plane-parallel assumption does not permit tangent line of sights. Most of the differences can be explained using the line of

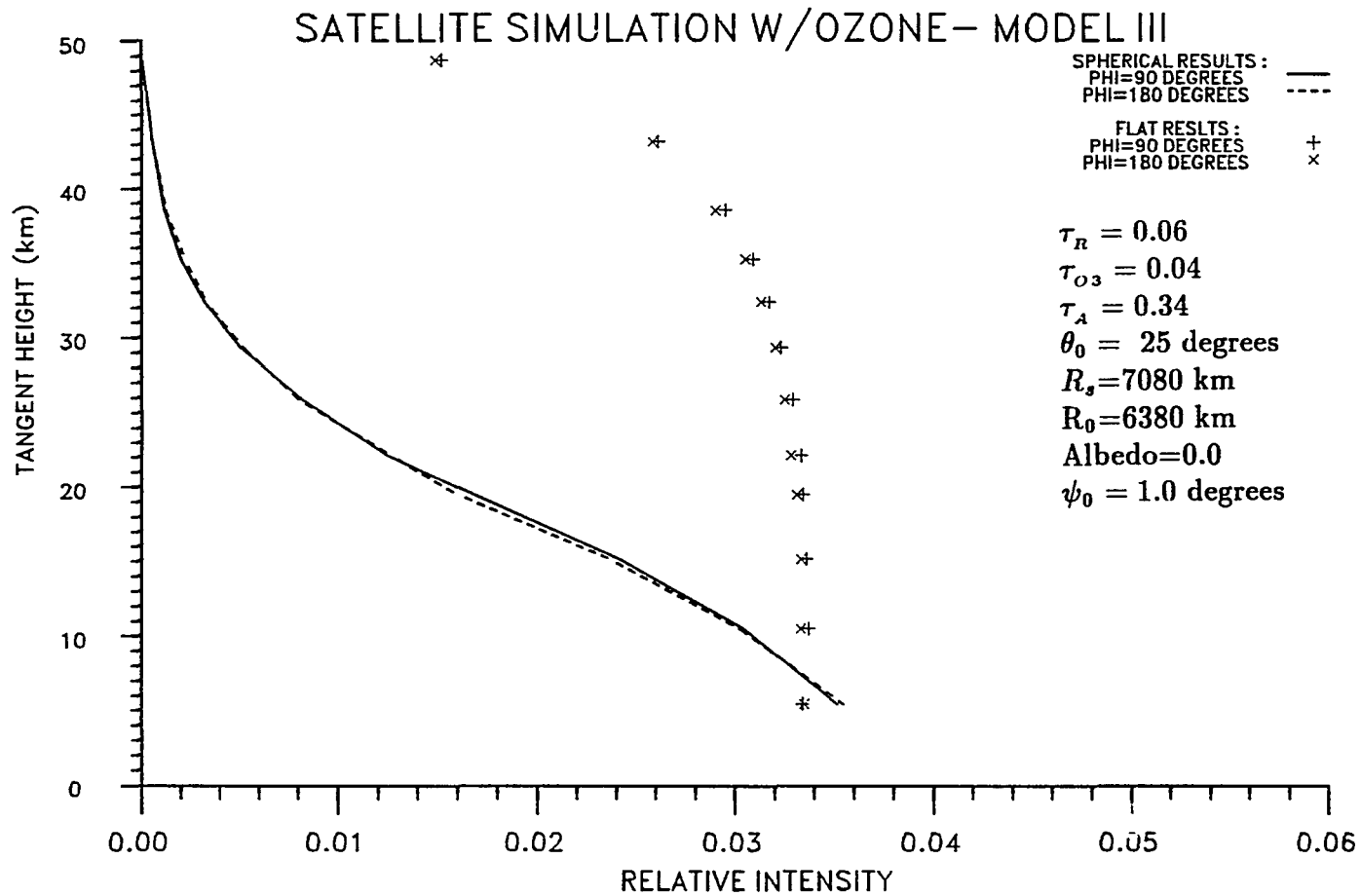


Figure 5.4 Flat atmosphere comparison for Model III with 0.04 ozone optical depths for $\phi = 90$ and 180 degrees.

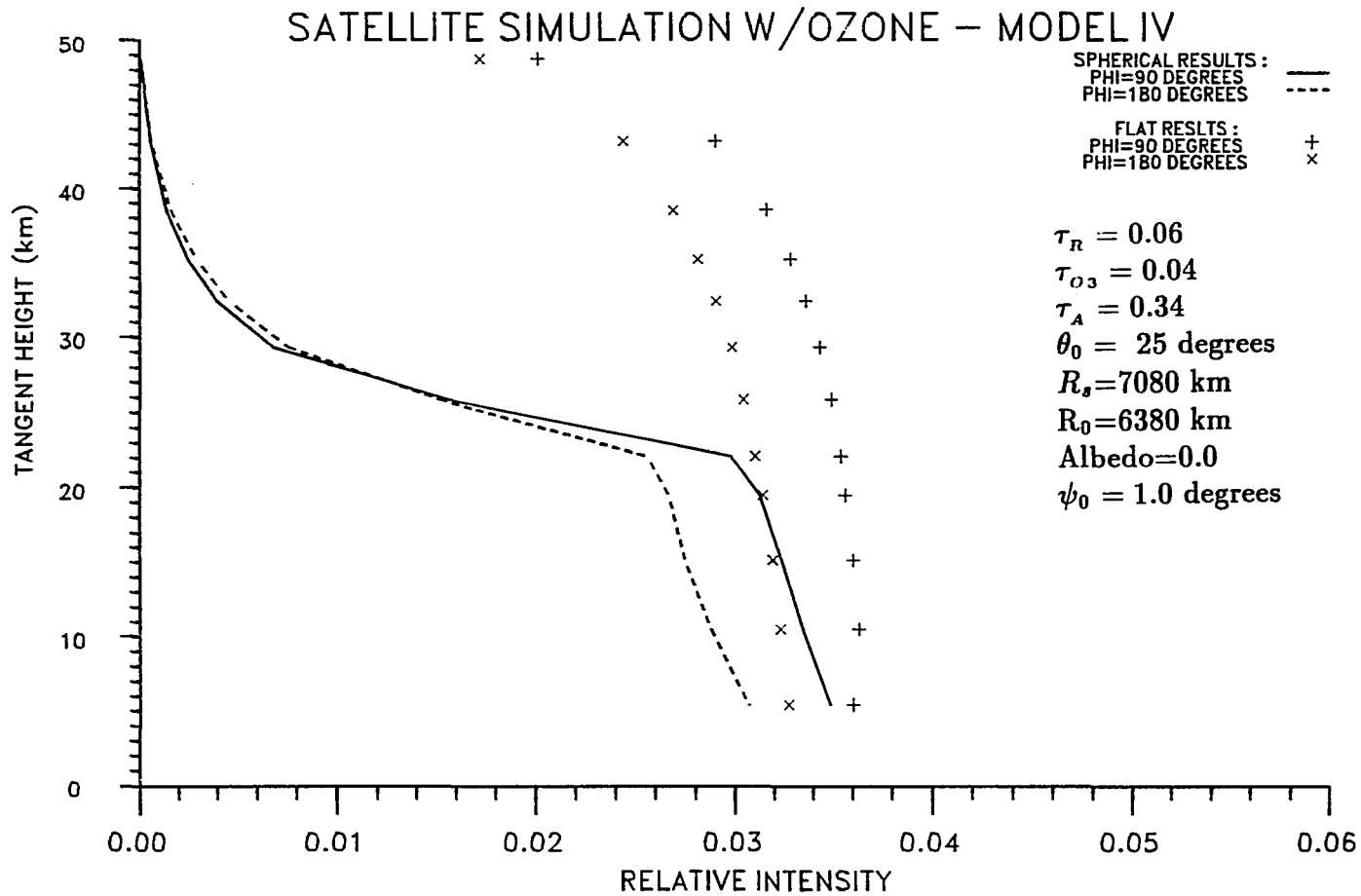


Figure 5.5 Flat atmosphere comparison for Model IV with 0.04 ozone optical depths for $\phi = 90$ and 180 degrees.

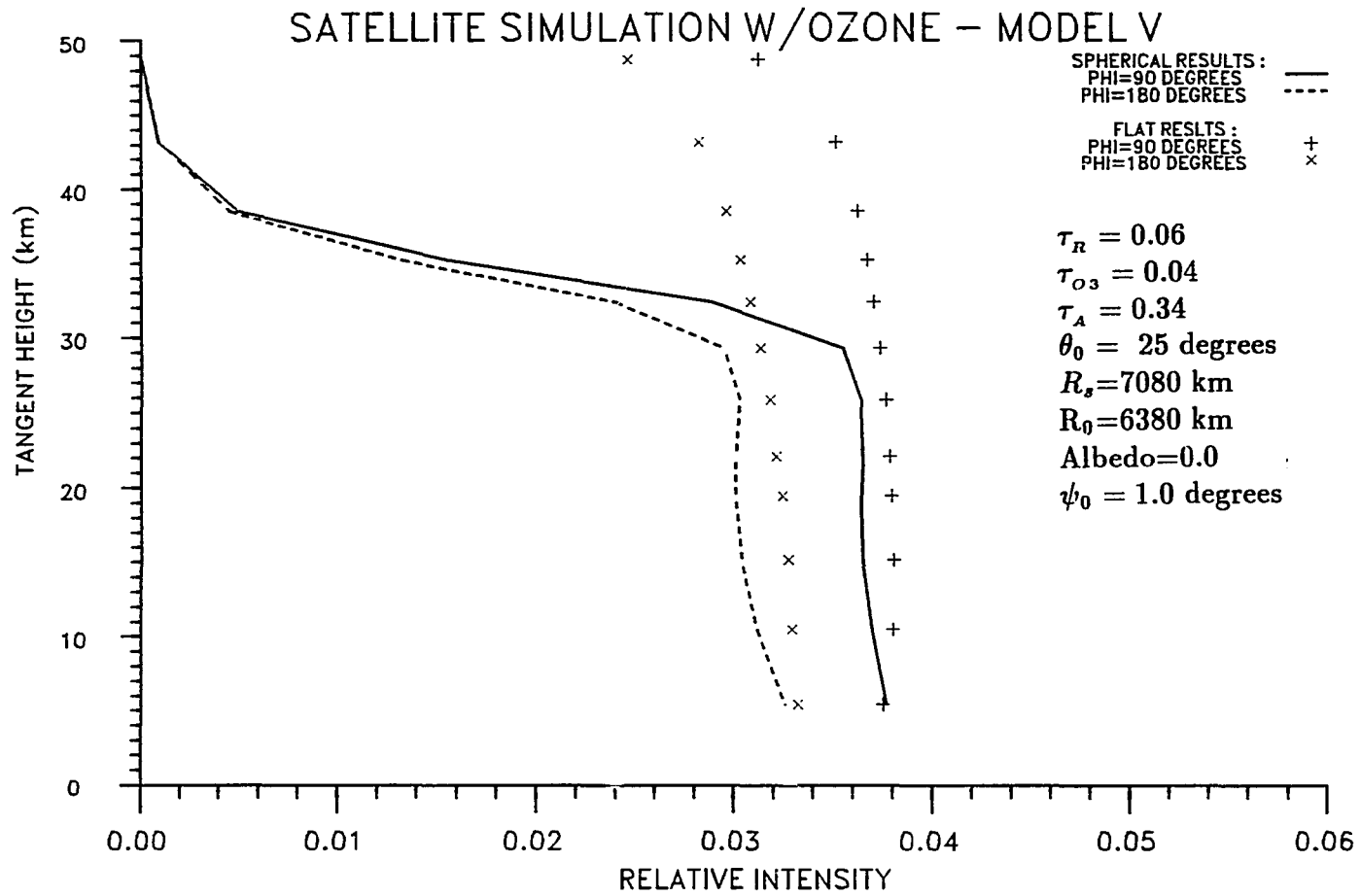


Figure 5.6 Flat atmosphere comparison for Model V with 0.04 ozone optical depths for $\phi = 90$ and 180 degrees.

sight arguments of Chapter IV, Section 3, and are not repeated here. There are some points worth mentioning. In both Figs. 5.5 and 5.6, the intensities for $\phi = 180$ are less than for $\phi = 90$. This is due to the larger solar path lengths for these lines of sight (Adams and Kattawar 1978). Also evident in the spherical results are sharp rises in the intensity corresponding to the heights of the aerosol layers. These sharp rises are absent from the flat atmosphere results because each line of sight in the flat atmosphere model must pass through every layer. In the spherical geometry, some of the lines of sight do not pass through the aerosol layers, and thus do not show the enhanced intensities from the extra scattering.

In Fig. 5.7 a comparison between Models III, IV, and V is given for the case where the ozone optical depth was 0.00. For Model III, the intensities rise smoothly through the atmosphere, while Models IV and V show local maxima near the peaks of the respective dust layers. Model III shows the largest intensities near the surface because of lower attenuation due to the smaller optical depth. Model V shows the lowest values because much of the incident energy is scattered out at higher levels. Another cause is that the geometric length of the paths through the dust layer of Model V are slightly smaller than those of Model IV. This is because lines of sight that are tangent near the surface strike layers in the upper part of the atmosphere at less of an angle than in lower regions of the atmosphere. Thus the geometric path is smaller through the upper level dust layers, the optical depth along the path through these layers is less, and the scattered intensity will be smaller.

Figure 5.8 shows the same comparison as Fig. 5.7 only with an ozone optical depth of 0.04. With the addition of ozone, several changes occur. All of the curves have shifted left, due to added attenuation, and essentially maintained

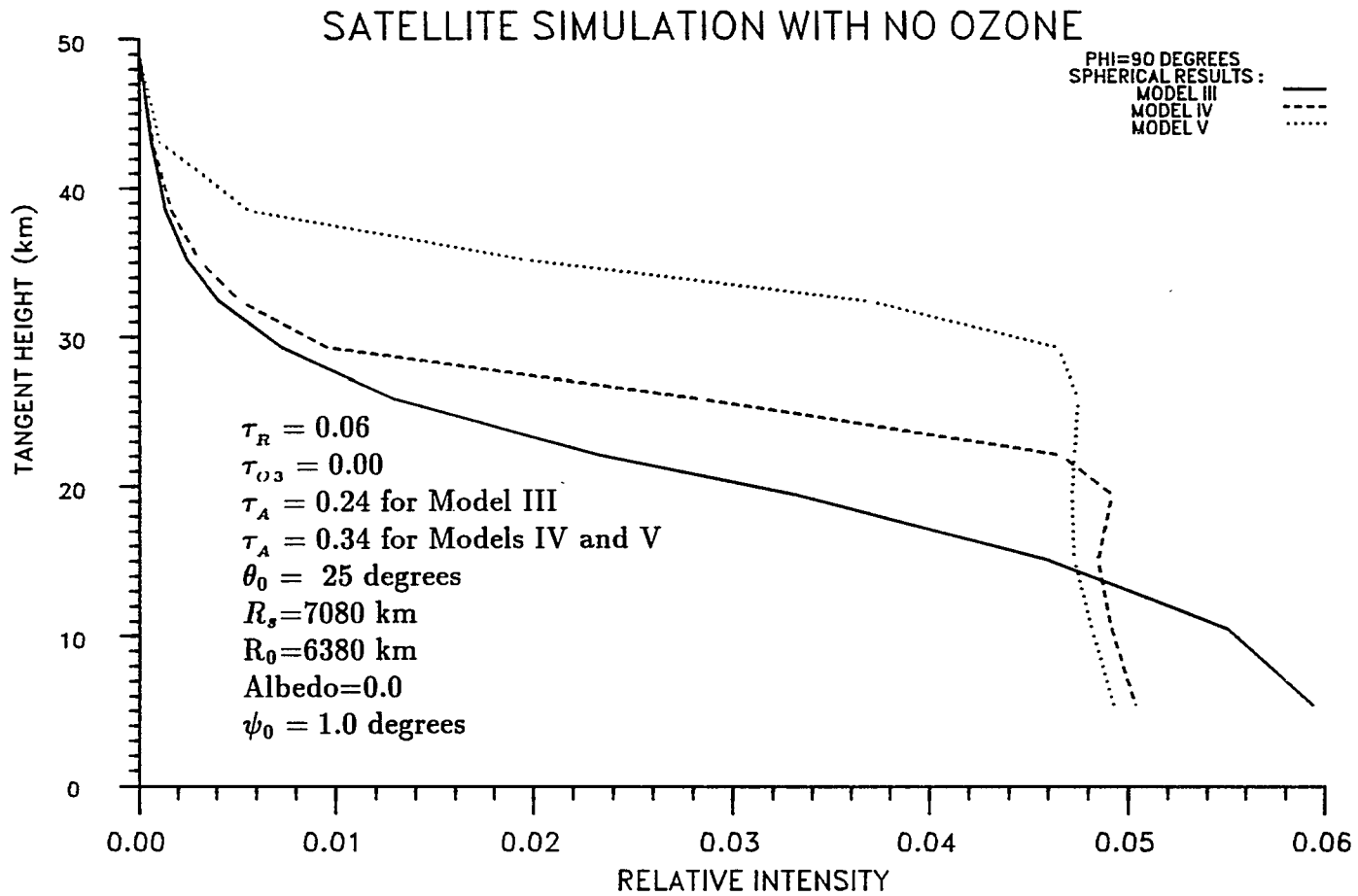


Figure 5.7 Comparison between Models III, IV, and V with 0.0 ozone optical depths for $\phi = 90$ degrees to show effect of volcanic layers.

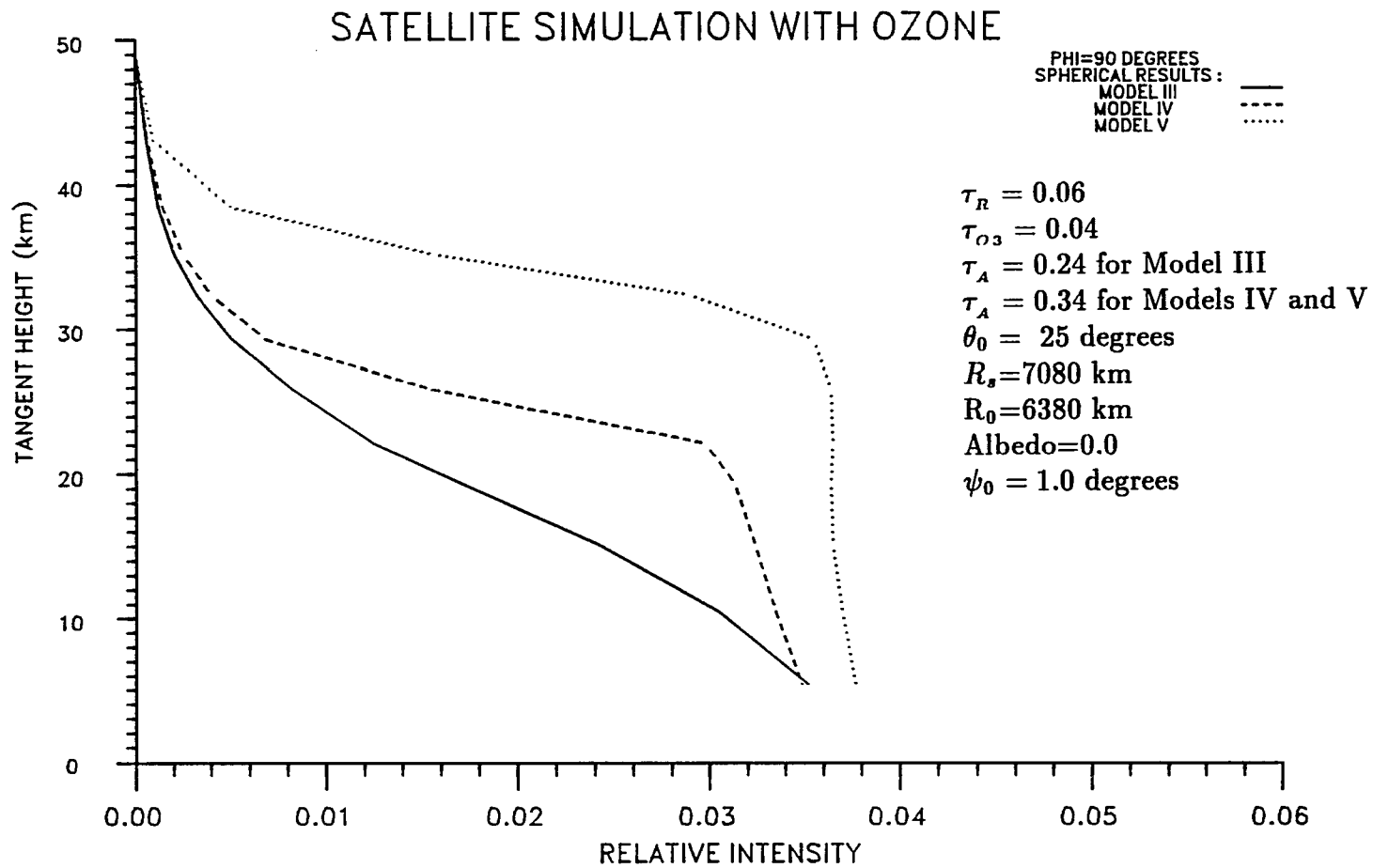


Figure 5.8 Comparison between Models III, IV, and V with 0.04 ozone optical depths for $\phi = 90$ degrees to show effect of volcanic layers.

their shapes. The sharp rises in intensity due to the stratospheric dust layers of Models IV and V are still present. These rises still correspond to the heights of the dust layers, but the local maxima are absent. Also noticeable is the fact that Model V intensities are now the largest as a result of scattering above the ozone absorption. For a given line of sight there is a contribution from aerosol scattering that does not undergo absorption. Not only is some of the scattered energy not being absorbed, but the incident solar energy is also not affected by absorption before it reaches the dust layer. This explains why Model IV is to the right of Model III, since with Model IV, some aerosol scattering still occurs before the entire ozone layer is passed. From the results presented above it is clear that the flat atmosphere cannot be used to simulate earth-atmosphere limb scans. It is also apparent that these limb scans can detect stratospheric dust layers.

A constituent receiving greater interest in recent years is ozone. Three cases were examined to study ozone retrieval from atmospheric limb scans. The first used $\theta_0 = 25$ degrees, no aerosol attenuation and ozone optical depths of 0.00, 0.02, 0.04, 0.08. The results are given in Fig 5.9 and indicate changes of over 70% in total intensity at a height of 15 km over the range of ozone amounts used. In the upper portions of the atmosphere, where paths do not encounter ozone, no significant differences occur as the ozone amount increases. The above case was also run for $\theta_0=85$ degrees(Fig. 5.10). In these runs, the intensity changes are larger, but the signal level has decreased. The last case(Fig. 5.11) used $\theta_0=25$ degrees, ozone optical depths of 0.0, 0.02 and 0.04, and included Model III aerosols. Here the percent changes in intensity are less, but signal levels are much higher.

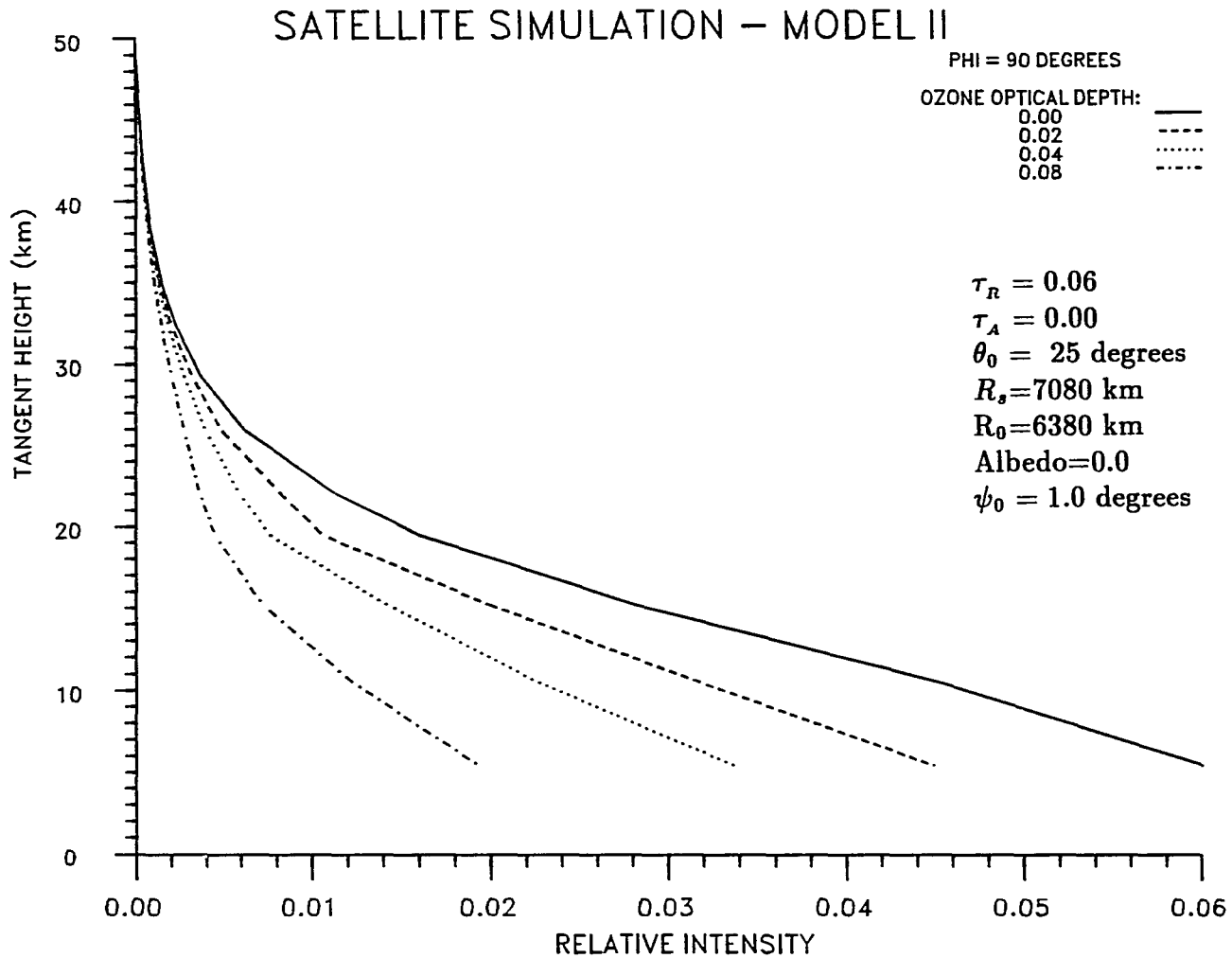


Figure 5.9 Satellite limb scan simulation for Model II with ozone optical depths of 0.00, 0.02, 0.04, and 0.08 and $\phi = 90$ degrees.

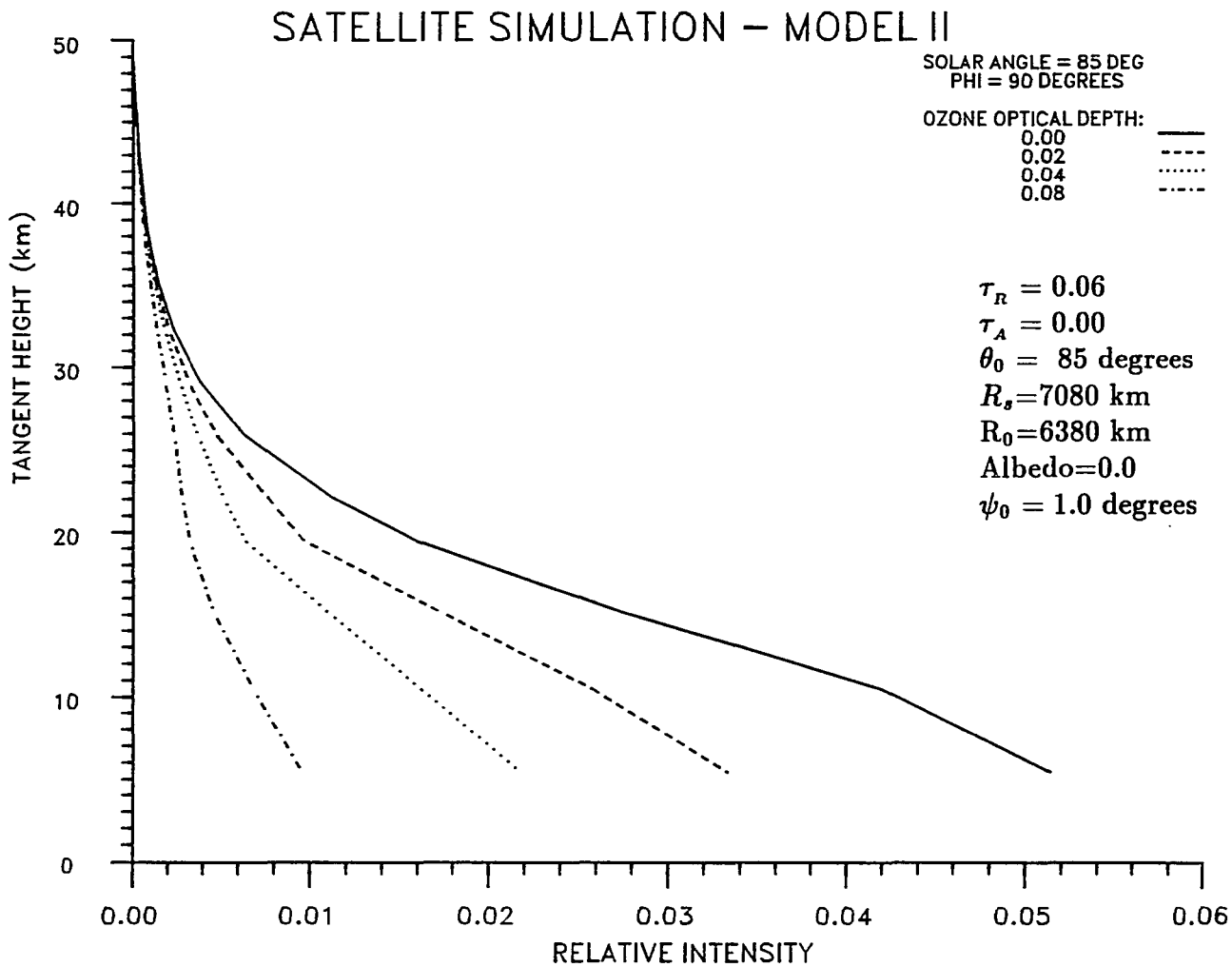


Figure 5.10 Satellite limb scan simulation for Model II with ozone optical depths of 0.00, 0.02, 0.04, and 0.08 and $\phi = 90$ degrees and solar zenith angle of 85 degrees.

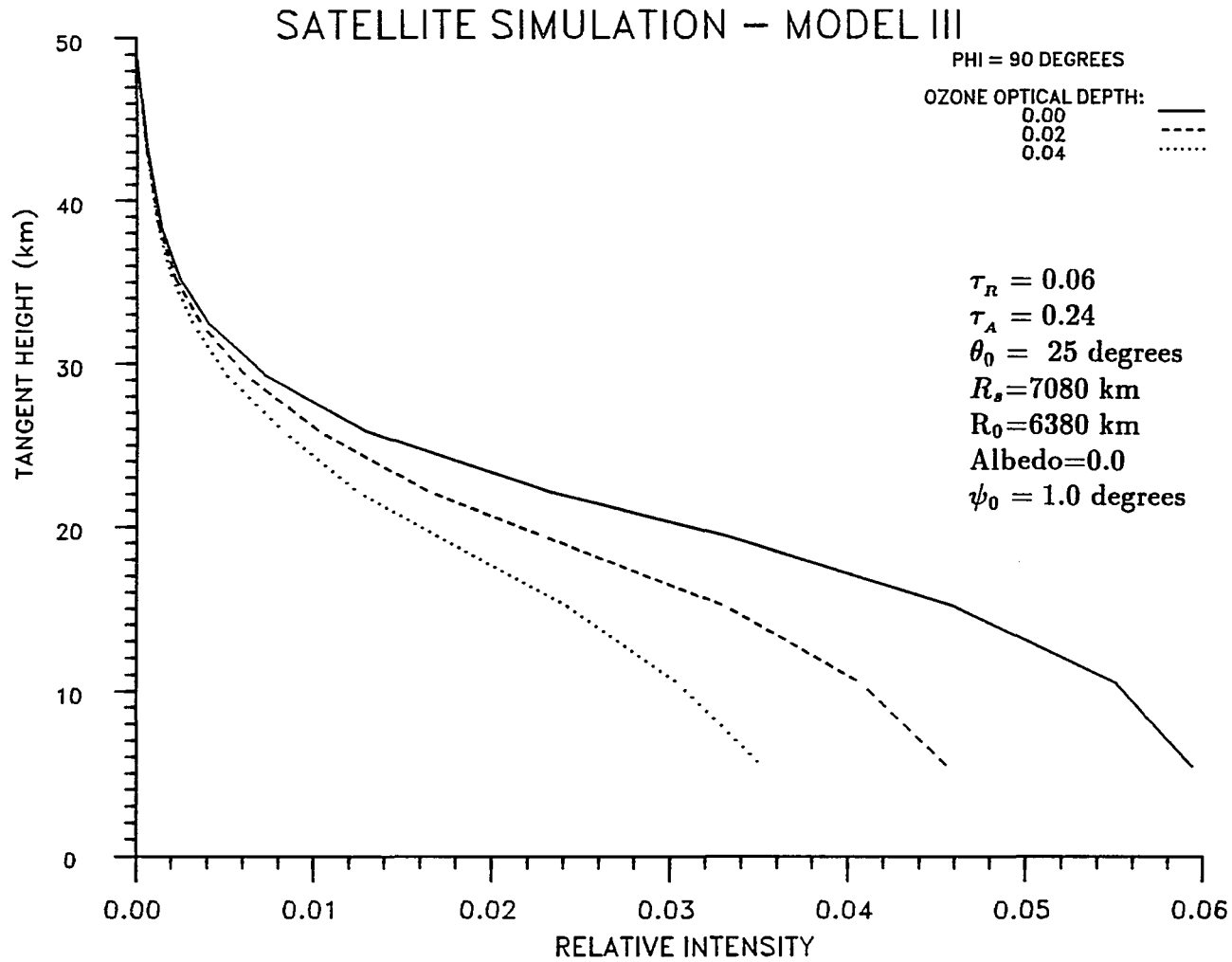


Figure 5.11 Satellite limb scan simulation for Model III with ozone optical depths of 0.00, 0.02, 0.04, and $\phi = 90$ degrees.

From these results, the limb scan should be effective at retrieving total columnar ozone. Because of the higher signal levels, it appears that a high sun case at wavelengths where dust can enhance the signal further would be preferable. One proposed technique is to use the ratio of intensities at two heights. One of these heights would be above the ozone while the other below. By ratioing, changes due to aerosols are negated and the size of the ratio would indicate changes in ozone. Further research is required to determine the specifics of this type of retrieval, but discussion of this is beyond the scope of the current work.

CHAPTER VI

CONCLUSIONS AND FURTHER WORK

In this dissertation a new model for computing radiative transfer in a spherically symmetric atmosphere is presented. The model uses a Gauss-Sidel iteration scheme developed by Herman (1963) for application to the plane-parallel atmosphere. In order to account for inhomogeneities in the horizontal intensity field due to sphericity, the current work introduces a conical boundary. The solutions on the boundary are found and used in an interpolation scheme to obtain the intensity at each level on the radial line at the center of the cone. The results can be found for any set of polar angles and height levels and for 30 degree increments in azimuth. The model includes absorption and aerosols but neglects polarization and refraction.

Several checks of the model were performed. Results for a high sun and small optical depth were compared to flat atmosphere results. All differences were consistent with geometric arguments. The results from a model run where the radius of the planet was increased by a factor of 100 were found to agree with flat atmosphere results to better than 1%. The model was also run for low sun and layer optical depths on the order of 0.035. Flux was conserved for this case to better than 3%. Boundary solutions were also found to be accurate to better than 3% for all nontangent paths, and better than 12% for tangent paths. With a biased boundary solution of 10%, the central solution was found to vary by less than 1%. The final test of the model was to compare with other models. Results agreed favorably with those of Asous (1982), Marchuk *et al.* (1980) and Adams and Kattawar (1978).

From the results of these tests the current model is concluded to be accurate to 3%. It is felt that in most earth-atmosphere situations the results are accurate to 1%. This accuracy is on the order of, or better than, previous techniques including spherical geometry. The current method is as accurate as a Monte Carlo simulation but computationally more efficient. Because of its versatility and accuracy, the cone method performs better than the techniques that strive for computational efficiency described in Chapter I.

The model was used to examine the atmospheric limb problem. From these results it is concluded that there is great promise in these measurements for the determination of atmospheric constituents. This is especially true for the cases of stratospheric dust layers and ozone. Further work is currently being done in this area.

Further work is also being done to include the effects of polarization, refraction, and the forward peak due to aerosols. The exclusion of these factors does not dramatically affect the usefulness of the model (Marchuk *et al.* 1980 and Blattner (1974)), but for intensive studies of the twilight sky and sub-horizon suns, they should be considered. To also enhance the results of twilight sky and sub-horizon sun modeling, the optical depths of lines of sight should be computed to the solar terminator rather than to the nearest level. To avoid problems due to this, the current model is run for a larger number of layers, but because of the added computer time, this is not desirable.

Lastly, a technique is being developed to increase the number of polar angles around ninety degrees. This method utilizes an approach similar to that developed by Herman *et al.* (1971) to compute the forward peak from aerosols. Intensities at these extra angles are calculated after the model has

been run, thereby increasing the number of angles without significantly affecting the computation time. Currently this method produces results to better than 4%. Further work is being done to get this value to less than 2%.

APPENDIX A

CALCULATION OF ATMOSPHERIC PARAMETERS

This appendix describes the calculations needed to determine the atmospheric parameters used in the radiative transfer calculations. These parameters are the heights of the levels, the optical depth within each homogeneous layer, and the Rayleigh and aerosol phase functions. For a more detailed description on these topics the reader is directed to Herman (1963), Herman and Browning (1965), Asous (1982) and Bohren and Huffman (1983).

Before the radiative transfer calculations are performed, the atmosphere is divided into homogeneous layers. In a plane-parallel atmosphere, optical depth is the only parameter considered when selecting the thicknesses of these layers. Each level is selected such that a layer is optically thin enough to prevent the intensity from varying non-linearly along a path in the layer. The value of optical depth corresponding to this restriction is approximately 0.03. As long as the layer optical depth does not exceed this value, the Gauss-Sidel method is accurate. Using optical depth as the criteria for dividing the atmosphere results in thinner geometric layers near the surface than near the top of the atmosphere as a consequence of the fact that the major atmospheric constituents have larger concentrations near the surface.

In the plane-parallel methods, the top layer of the atmosphere is often as large as 30 km. Using a Gauss-Sidel process, it would be impossible to accurately model the spherical geometry of the problem using a layer as thick as this. The current method subdivides this top layer using approximately half of the total

number of levels in the problem. This essentially divides the atmosphere into two parts, the lower half to account for optical depth and the upper to account for the spherical nature of the problem. The top half of the atmosphere is divided evenly and then checked to ensure that no path covers more than 4 degrees of arc before exiting the layer. This is to ensure that the approximations used to compute the boundary values in the radiative transfer model remain valid. By evenly dividing the atmosphere between 30 and 50 km into 9 layers, this criteria is met. The method of division attempts to satisfy both the geometric and optical depth requirements. It also attempts to ensure a smooth transition from where the atmosphere is divided by optical depth to that divided by geometry.

To actually divide the atmosphere into layers of known optical depth, the vertical distribution of atmospheric constituents must be known. In this dissertation, the 1962 U.S. Standard Atmosphere midlatitude winter model is used. This distribution may easily be modified. The relative size distribution of aerosols is constant with height and follows a Junge power law with exponent 3 and maximum and minimum radii of 5.0 and 0.1 microns. The aerosols are non-absorbing with real index of refraction of 1.5. To compute the optical depth due to a given constituent in a layer, the total optical depth due to that constituent is multiplied by the percentage of the constituent in the layer.

To obtain the required layer phase functions for the radiative transfer model, the Rayleigh and aerosol phase functions must be calculated. The Rayleigh phase function is computed at one degree increments of scattering angle from 0 to 180 degrees according to

$$P_R(\Theta) = \frac{3}{16\pi}(1 + \cos^2\Theta) \quad (A.1)$$

where Θ , the scattering angle, is the angle between the incident and scattered

light. Each of the values of P_R obtained from (A.1) is then normalized such that

$$\sum_{\Theta=0}^{180} P_R(\Theta)\Delta\omega = 1 \quad (A.2)$$

where $\Delta\omega$ is the increment of solid angle about the scattering angle Θ . To ensure that energy is conserved over the larger increments of the radiative transfer calculations, normalization constants are used such that for each scattering direction, θ_i ,

$$C_R(\theta_i) = \frac{1.0}{\sum_j \sum_k P_R(\theta_i, \phi = 0, \theta_j, \phi_k)\Delta\mu_j\Delta\phi_k} \quad (A.3)$$

where

$$\Delta\mu_j = \cos\left(\frac{\theta_{j-1} + \theta_j}{2}\right) - \cos\left(\frac{\theta_{j+1} + \theta_j}{2}\right) \quad (A.4)$$

and

$$\Delta\phi_k = \frac{\phi_{k+1} - \phi_{k-1}}{2} \quad (A.5)$$

And the summation is carried out over all incident directions θ_i and ϕ_k .

The calculation of the aerosol phase function is more complicated. For simplicity, the atmospheric aerosols are assumed to behave as Mie scatterers. It is realized that all particles in the atmosphere are not spherical, and thus not Mie scatterers, But as stated, this simplifies the problem. For a description of Mie scattering see Stratton (1946). As was the case for the Rayleigh phase function, the aerosol phase function is computed at one degree intervals from 0 to 180 degrees. The calculations are performed using an algorithm developed by Bohren and Huffman (1983). The phase function is also summed over the size distribution and normalized so the sum over solid angle is unity. Since the aerosol phase function may vary appreciably over the angular intervals used in the radiative transfer model, an average phase function over the interval is

computed. To compute this average over the given interval in θ and ϕ , the θ interval is broken into 10 sub-intervals and ϕ into 30. Then

$$\bar{P}_A(\theta_i, \phi_j, \theta_{i'}, \phi_{j'}) = \frac{\sum_l \sum_m P_A(\theta_i, \phi_j, \theta_l, \phi_m) \Delta\mu_l \Delta\phi_m}{\sum_l \sum_j \Delta\mu_l \Delta\phi_m} \quad (A.6)$$

where the summation over l is for the θ sub-interval about i' , the summation over m is for the ϕ sub-interval about j' , and $P_A(\theta_i, \phi_j, \theta_l, \phi_m)$ is interpolated from the set of 181 values at each single degree in Θ . To ensure energy conservation, normalization constants are used,

$$C_A(\theta_i) = \frac{\varpi_0}{\sum_j \sum_k \bar{P}_A(\theta_i, \phi = 0, \theta_j, \phi_k) \Delta\mu_j \Delta\phi_k} \quad (A.7)$$

The actual radiative transfer calculations use layer phase functions. To obtain these, the phase functions are averaged for the given layer according to

$$P(z_1, \theta_i, \phi_j, \theta_{i'}, \phi_{j'}) = \frac{(\tau_R(z_1)C_R(\theta_i)P_R(\theta_i, \phi_j, \theta_{i'}, \phi_{j'}) + \varpi_{0A}\tau_A(z_1)C_A(\theta_i)\bar{P}_A(\theta_i, \phi_j, \theta_{i'}, \phi_{j'}))}{\tau_R(z_1) + \tau_A(z_1) + \tau_{abs}(z_1)} \quad (A.8)$$

where ϖ_{0A} is the aerosol single scatter albedo from the Mie calculations, the "R" subscript refers to Rayleigh, the "A" subscript to aerosols, and "abs" to absorption. Then $\tau_R, \tau_A, \tau_{abs}$ are the Rayleigh, aerosol, and absorption optical depths for the layer l . This is the phase function that is used in the radiative transfer calculations.

REFERENCES

- Adams, C. N., G. N. Plass, and G. W. Kattawar, 1974, The Influence of Ozone and Aerosols on the Brightness and Color of the Twilight Sky. *J. Atmos. Sci.*, Vol. 31, pp. 1662-1674.
- Adams, C. N., and G. W. Kattawar, 1978, Radiative Transfer in Spherical Shell Atmospheres: I. Rayleigh Scattering. *Icarus*, Vol. 35, pp. 139-151.
- Antyufeyev, V. S., and M. A. Nazaraliev, 1973, A New Modification of the Monte Carlo Method for Solution of Problems in the Theory of Light Scattering in a Spherical Atmosphere. *Izv. Acad. Sci. USSR, Atmos. Oceanic Phys.*, Vol. 9, pp. 463-467.
- Asous, W. A., 1982, Light Scattering in Spherical Atmospheres. *Ph.D. Dissertation*, Dept. of Electrical Engineering, University of Arizona, Tucson, Az.
- Bailey, P. B., 1964, A Rigorous Derivation of Some Invariant Imbedding Equations of Transport Theory. *J. Math. Anal. Appl.*, Vol. 8, pp. 144-169.
- Bellman, R. E., H. H. Kagiwada, and R. E. Kalaba, 1966, Invariant Imbedding and Radiative Transfer in Spherical Shells. *J. Comp. Phys*, Vol. 1, pp. 245-256.
- Bellman, R. E., H. H. Kagiwada, and R. E. Kalaba, 1968, Diffuse Transmission of Light from a Central Source Through an Inhomogeneous Spherical Shell with Isotropic Scattering. *J. Math. Phys.*, Vol. 9, pp. 909-912.
- Bellman, R. E., H. H. Kagiwada, and R. E. Kalaba, 1969, Diffuse Reflection of Solar Rays by a Spherical Shell Atmosphere. *Icarus*, Vol. 11, pp. 417-423.
- Blattner, W. G. M., 1977, Light Scattering in Spherical Shell Atmospheres. *Radiation in the Atmosphere*. Science Press, Princeton, NJ.
- Blattner, W. G., G. H. Horak, D. G. Collins, and M. B. Wells, 1974, Monte Carlo Studies of the Sky Radiation at Twilight. *Appl. Opt.*, Vol. 13, pp. 534-547.
- Blattner, W. G. and M. B. Wells, 1973, *Monte Carlo Studies of Sky Radiation*. AFCRL Report No. TR-73-0613, Air Force Cambridge Research Laboratories, Bedford, Mass.

- Casinelli, J. P., 1971, Extended Model Atmospheres for the Central Stars of Planetary Nebulae. *Astrophys. J.*, Vol. 165, p. 265.
- Chandrasekhar, S., 1960, *Radiative Transfer*. Dover Publications, New York.
- Chapman, R. D., 1966, Radiative Transfer in Extended Stellar Atmospheres. *Astrophys. J.*, Vol. 143, pp. 61-74.
- Chu, W. P. and M. P. McCormick, 1979, Inversion of Stratospheric Aerosol and Gaseous Constituents from Spacecraft Solar Extinction Data in the 0.38 to 1.0 μm Wavelength Region. *Appl. Opt.*, Vol. 18, pp. 1404-1413.
- Collins, D. G., M. B. Wells, 1970, *FLASH, a Monte Carlo Procedure for Use in Calculating Light Scattering in Spherical Shell Atmospheres*. AFCRL Report No. 70-0206. Air Force Cambridge Research Laboratories, Bedford Mass.
- Collins, D. G., W. G. Blattner, M. B. Wells, and G. H. Horak, 1972, Backward Monte Carlo Calculation of Polarization Characteristics of Radiation Emerging from Spherical-Shell Atmospheres. *Appl. Opt.*, Vol. 11, pp. 2684-2696.
- Coulson, K. L., 1980, Characteristics of Skylight at the Zenith During Twilight as Indicators of Atmospheric Turbidity, 1: Degree of Polarization. *Appl. Opt.*, Vol. 19, pp. 3469-3480.
- Coulson, K. L., 1981, Characteristics of Skylight at the Zenith During Twilight as Indicators of Atmospheric Turbidity, 2: Intensity and Color Ratio. *Appl. Opt.*, Vol. 20, pp. 1516-1524.
- Coulson, K. L., J. V. Dave, and Z. Sekera, 1960, *Tables Related to Radiation Emerging from a Planetary Atmosphere with Rayleigh Scattering*. University of California Press, Berkeley, CA.
- Dave, J. V., C. L. Mateer, 1968, The Effect of Stratospheric Dust on the Color of the Twilight Sky. *J. Geophys. Res.*, Vol. 73, pp. 6897-6913.
- Divari, N. B., 1967, Calculation of the Polarization of the Light of the Twilight Sky. *Izv. Acad. Sci. USSR, Atmos. Oceanic Phys.*, Vol. 3, pp. 287-291.
- Divari, N. B., and L. I. Plotnikova, 1966, Computed Brightness of the Twilight Sky. *Sov. Astron.*, Vol. 9, pp. 840-852.

- Elterman, L., 1968. *UV, Visible, and IR Attenuation for Altitudes to 50 km.* AFCRL Report No. 68-0153. Air Force Cambridge Research Laboratories, Bedford, Mass.
- Gray, C. R., H. L. Malchow, D. C. Merrit, R. E. Var, and C. K. Whitney, 1973, *Aerosol Physical Properties from Satellite Horizon Inversion.* NASA Contractor Report 112311, NTIS No. N73-27330.
- Herman, B. M., 1963, A Numerical Solution to the Equation of Radiative Transfer for Particles in the Mie Region. *Ph.D. Dissertation*, Dept. of Atmospheric Sciences, University of Arizona, Tucson, AZ.
- Herman, B. M. and S. R. Browning, 1965, A Numerical Solution to the Equation of Radiative Transfer. *J. Atmos. Sci.*, Vol. 22, pp. 559-566.
- Herman, B. M. and S. R. Browning, 1975, The Effect of Aerosols on the Earth-Atmosphere Albedo. *J. Atmos. Sci.*, Vol. 32, pp. 1430-1445.
- Herman, B. M., W. Asous, and S. R. Browning, 1980, A Semi-analytic Technique to Integrate the Radiative Transfer Equation over Optical Depth. *J. Atmos. Sci.*, Vol. 37, pp. 1828-1838.
- Herman, B. M., S. R. Browning, and R. J. Curran, 1971, The Effect of Atmospheric Aerosols on Scattered Sunlight. *J. Atmos. Sci.*, Vol. 28, pp. 419-428.
- Hulbert E. O., 1953, Explanation of the Brightness and Color of the Sky, Particularly the Twilight Sky. *J. Opt. Soc. Am.*, Vol. 43, pp. 113-118.
- Hummer, D. G. and G. B. Rybicki, 1971, Radiative Transfer in Spherical Symmetric Systems. The Conservative Gray Case. *Mon. Not. R. Astron. Soc.*, Vol. 152, pp. 1-19.
- Ishimaru, A., 1978, *Wave Propagation and Scattering in Random Media, Vol 1.* Academic Pres, Inc. New York.
- Kattawar, G. W. and C. N. Adams, 1978, Radiative Transfer in Spherical Shell Atmospheres: II Asymmetric Phase Functions. *Icarus*, Vol. 35, pp. 436-449.

- Kattawar, G. W., G. N. Plass, and C. N. Adams, 1971, Flux and Polarization Calculations of the Radiation Reflected from the Clouds of Venus. *Astrophys. J.*, Vol. 170, pp. 371-386.
- Lenoble, J., 1977, Comparison of Computation Technique in Scattering Problems. *Radiation in the Atmosphere*. Science Press, Princeton, NJ.
- Lenoble, J., 1985, *Radiative Transfer in Scattering and Absorbing Atmospheres: Standard Computational Procedures*. A. Deepak Publishing, VA.
- Lenoble, J. and Z. Sekera, 1961, Equation of Transfer in a Planetary Spherical Atmosphere. *Proc. National Academy of Science, USA*, Vol. 47, pp. 372-378.
- Leong, T. K. and K. K. Sen, 1972, A Probabilistic Model for Time-Dependent Transfer Problems In Spherical Shell Media. *Mon. Not. R. Astron. Soc.*, Vol. 160, pp. 21-36.
- Leong, T. K. and K. K. Sen, 1975, Probabilistic Model for Transfer Problem of a Externally Illuminated Shell Atmosphere with Perfectly Absorbing Core. *Ann. d'Astrophys.*, Vol. 31, pp. 467-474.
- Marchuk, G. I. and G. A. Mikhailov, 1967a, The Solution of Atmospheric Optics by a Monte Carlo Method. *Izv. Acad. Sci. USSR, Atmos. Oceanic Phys.*, Vol. 3, pp. 147-155.
- Marchuk, G. I. and G. A. Mikhailov, 1967b, Results of the Solution of Certain Problems in Atmospheric Optics by the Monte Carlo Method. *Izv. Acad. Sci. USSR, Atmos. Oceanic Phys.*, Vol. 3, pp. 227-231.
- Marchuk, G. I., G. A. Mikhailov, M. A. Nazaraliev, R. A. Darbinjan, B. A. Kargin, and B. S. Elepov, 1980, *The Monte Carlo Methods in Atmospheric Optics*. Springer-Verlag, Berlin.
- Martin, P. G., C. Roger, and G. B. Rybicki, 1984, Half Range Moment Methods for Radiative Transfer in Spherical Geometry: II. Implementation of the Method. *Astrophys. J.*, Vol. 284, pp. 317-326.
- Mikhailov, G. A. and M. A. Nazraliev, 1971, Calculation of the Polarization of Light in a Spherical Atmosphere by Monte Carlo Method. *Izv. Acad. Sci. USSR Atmos. Oceanic Phys.*, Vol. 7, pp. 254-260.

- Minin, I. N. and V. V. Sobolev, 1963, The Theory of Radiation Scattering in Planetary Atmospheres. *Sov. Astron.*, Vol. 7, pp. 379-383.
- Newell, R. E. and C. R. Gray, 1972, *Meteorological and Ecological Monitoring of the Stratosphere and Mesosphere*. NASA Contractor Report 2094, NTIS No. N72-30343.
- Peraiah, A. and B. A. Varghese, 1985, Radiative Transfer Equation in Spherical Symmetry. *Astrophys. J.*, Vol. 290, pp. 411-423.
- Rogers, C., 1984, Half Range Moment Methods for Radiative Transfer in Spherical Geometry: V. Line Formation in a Static Atmosphere. *Astrophys. J.*, Vol. 286, pp. 659-665.
- Rogers, C. and P. G. Martin, 1984, Half Range Moment Methods for Radiative Transfer in Spherical Geometry: III. Numerical Solution and Applications. *Astrophys. J.*, Vol. 284, pp. 327-336.
- Rozenberg, G. V., 1965, Investigations at Twilight of Planetary Atmospheres from Spacecraft. *Izv. Acad. Sci. USSR, Atmos. Oceanic Phys.*, Vol 1, pp. 223-227.
- Rozenberg, G. V., 1966, *Twilight: A Study in Atmospheric Optics*. Plenum Press, New York.
- Shah, G. M., 1969, Enhanced Twilight Glow Caused by the Volcanic Eruption on Bali Island in March and September 1963. *Tellus*, Vol. 21, pp. 636-640.
- Simonneau, E., 1976, Radiative Transfer in Atmospheres with Spherical Symmetry. *J. Quant. Spectrosc. Radiat. Trans.*, Vol. 16, pp. 741-753.
- Smokty, O. I., 1969, Multiple Light Scattering in the Spherical Planetary Atmosphere. *Pure Appl. Geophys.*, Vol. 72, pp. 214-226.
- Sobolev, V. V., 1963, *A Treatise on Radiative Transfer*. Van-Nostrand, Co. Princeton, NJ.
- Sobolev, V. V., 1975, *Light Scattering in Planetary Atmospheres*. Pergammon Press, Ltd. New York.

- Stratton, J. A., 1941, *Electromagnetic Theory*. McGraw-Hill Book Co. New York.
- Unno, W. and M. Kondo, 1976, The Eddington Approximation Generalized for Radiative Transfer in Spherically Symmetric Systems. I. Basic Method. *Publ. Astron. Soc. Japan*, Vol. 28, pp. 347-354.
- Van de Hulst, H. C., 1980, *Multiple Light Scattering Tables, Formulas and Applications Vol 1 and 2*. Academic Press. New York.
- Volz, F., 1970, On Dust in the Tropical and Midlatitude Stratosphere from Recent Twilight Measurements. *J. Geophys. Res.*, Vol 75, p. 1641.
- Whitney, C., 1972, Implications of a Quadratic Stream Definition in Radiative Transfer Theory. *J. Atmos. Sci.*, Vol. 29, pp. 1520-1530.
- Whitney, C., 1974, Efficient Stream Distributions in Radiative Transfer Theory. *J. Quant. Spectrosc. Radiat. Tran.*, Vol. 14, pp. 591-611.
- Whitney, C. K., R. E. Var, and C. R. Gray, 1973, *Research into Radiative Transfer Modeling and Applications*. AFCRL Report No. TR-73-0420. Air Force Cambridge Research Laboratories, Bedford, Mass.
- Wilson, S. J. and K. K. Sen, 1980a, Light Scattering by an Optically Thin Inhomogeneous Spherically-symmetric Planetary Atmosphere. *Astrophys. Sp. Sci.*, Vol 69, pp. 107-113.
- Wilson, S. J. and K. K. Sen, 1980b, Light Scattering by an Optically Thin Inhomogeneous Spherically-symmetric Planetary Atmosphere: Brightness at the Zenith Near Terminator. *Astrophys. Sp. Sci.*, Vol 71, pp. 405-410.